HEAVY-ION-INDUCED TERNARY FISSION AS A PROBE OF THE DYNAMICAL DECAY OF EXCITED NUCLEI

Todd A. Bredeweg

Accepted by the Graduate Faculty, Indiana University, in partial fulfillment of the
requirements for the degree of Doctor of Philosophy.

Oral Examination
May 2, 2001

Romualdo T. de Souza, Ph.D.

Victor E. Viola Jr., Ph.D.

W. Michael Snow, Ph.D.

Glenn A. Martyna, Ph.D.

Dedication

To my wife Deb, whose support, encouragement and patience has made this document possible.

Acknowledgments

I would like to thank my research advisor, Prof. R.T. de Souza, for his guidance and patience over the years. I would also like to thank the other members of my thesis commitee, Prof. G.A. Martyna, Prof. W.M. Snow and especially Prof. V.E. Viola.

Abstract

Investigation of ternary fission in the reaction ^{12}C + ^{232}Th at projectile energies of $E_{lab} = 193$ and 264 MeV has revealed two components, only one of which can be understood within a standard statistical emission framework. Comparison of the relative emission probabilities for intermediate mass fragments (IMFs), fragments with atomic number $3 \leq Z \leq 20$, as a function of the initial excitation of the composite system has provided evidence that two different mechanisms exist for IMF emission. IMFs emitted early, prior to significant deformation of the system, exhibit behavior consistent with statistical emission. IMFs emitted later, near-scission, manifest significantly different behavior. The characteristics of early stage and near-scission emission are explored. Comparisons are also made to recent work in spontaneous and thermal neutron induced ternary fission.

Romualdo T. de Souza, Ph.D.

Victor E. Viola Jr., Ph.D.

W. Michael Snow, Ph.D.

Glenn A. Martyna, Ph.D.

Contents

List of Figures

List of Tables

Chapter 1

Introduction

Nuclei are observed to decay *via* statistical emission of particles in a process analogous to evaporation in macroscopic liquids [1, 2]. Nuclear collisions, used to prepare excited nuclear matter, may, however, lead to deformed nuclear shapes that are subject to dynamical (time-dependent) instabilities [3]. Dynamical effects in nuclear reactions have been recognized in the pre-equilibrium emission of nucleons and fragments [4] and in the multifragmentation of the mid-rapidity zone in near-symmetric heavy-ion collisions [5]. All of these processes proceed on a rather fast time-scale ($\lesssim 10^{-21}$ s). The manifestation of dynamics on fragment emission on a longer time-scale, e.g. the fission time-scale ($\sim 10^{-17}$–10^{-20} s), has only recently been reported [6]. The purpose of this thesis is to further explore dynamical (non-statistical) fragment decay which occurs on the fission time-scale.

To study systems where the dynamical evolution of the shape of the nuclear system is important, yet keep the statistically thermalized energy modest, we have focused on ternary fission in the reaction ^{12}C + ^{232}Th at $E_{lab} = 16$ and 22 MeV/A. In this energy domain, incomplete fusion of the projectile and target nucleus occurs, followed by the fission of the heavy, excited composite system into two similar-sized fission fragments [7]. As the heavy composite nucleus undergoes the large scale deformation necessary for fission, it can decay *via* emission of neutrons, light charged particles (LCP: $1 \leq Z \leq 2$) and/or intermediate mass fragments (IMF:

$3 \leq Z \leq 20$). Such decay has been described with reasonable success within the framework of statistical emission theories [8, 9]. Recently, it has also been found that IMFs are emitted from the region between the two fission fragments near the moment of scission (near scission emission), with characteristic energy and angular distributions [10, 11]. The mechanism responsible for the production of these near-scission particles is presently unclear. Proposed mechanisms for similarly emitted alpha particles range from barrier modifications due to the proximity of the two fission fragments [12] to dynamical, double-neck rupture scenarios [13, 14]. While the former scenario is still statistical - driven by phase space considerations - the latter scenario is largely, if not completely, dynamical.

Several terms that will be used throughout this work are schematically depicted in Fig. 1.1. For the case of particle-induced fission, the energy of the parent nucleus may initially be well above the fission barrier. The saddle point is defined as the top of the fission barrier, and the scission point is the point at which the extended heavy system separates into two (or more) distinct fragments. The separated fragments are then accelerated by their mutual Coulomb repulsion. Within model descriptions the scission point is defined as the point at which the neck radius goes to zero or, within the description of random neck rupture (discussed below), the point at which the rupture actually occurs.

The purpose of the present work is to study the dynamics of fission, utilizing the experimentally measured properties of IMFs observed in coincidence with two corre-lated fission fragments. In particular, the yields of ternary fragments emitted near the moment of scission (near scission emission) are compared to those for emission prior to significant deformation of the parent composite nucleus. Additionally, trends in the near scission emission yields are investigated by comparing results from the current work with those from spontaneous and low energy induced ternary fission.
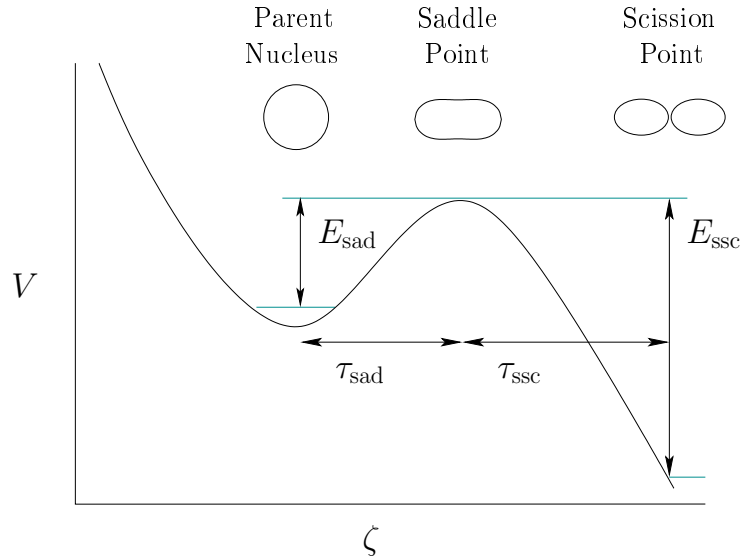
Figure 1.1: Simple schematic of a one dimensional fission barrier as a function of an arbitrary deformation parameter ζ along the fission coordinate. The three labeled stages in the fission process are defined in the text. The height of the barrier relative to the ground state of the parent nucleus is labeled E_{sad}, and the saddle to scission energy is labeled E_{ssc}. Three commonly referenced times in discussions of fission are the pre-saddle time, τ_{sad}, the saddle-to-scission time, τ_{ssc} and the pre-scission time, $\tau_{\mathrm{pre}} = \tau_{\mathrm{sad}} + \tau_{\mathrm{ssc}}$.

1.1   Statistical *vs.* Dynamical Decay of Excited Nuclei

Since its discovery, radioactivity has been viewed as a statistical process. The spontaneous decay of unstable nuclei is well described within the language of statistical mechanics. However, with the advent of induced nuclear decays, using accelerated particles or high energy photons for example, the situation has become less clear. Under these circumstances it is necessary to consider the dynamics of the initial interaction (entrance channel dynamics), and possibly the subsequent decay as well (exit channel or decay dynamics). Of particular interest in this regard is nuclear fission, as the large scale collective motion inherent even in spontaneous fission implies

the need for a dynamical description of the decay process.

Purely statistical models start with a fully equilibrated parent nucleus with a certain amount of internal excitation energy, which is then allowed to decay. The probability of decaying to a particular final state is dominated by the available excitation energy and its partitioning among the various single-particle and collective degrees of freedom. Such models provide no information concerning the time evolution of the system, i.e. how the equilibrated system was formed, including possible particle emission prior to achieving full equilibrium. Once the equilibrated source is formed its subsequent decay is considered to be primarily a function of the total available excitation energy, independent of the details of its formation. This decoupling of the entrance and exit channels is considered indicative of a mechanism that is consistent with statistical decay. Dynamical models attempt to describe the time evolution of the initial interaction and the subsequent decay. For example, during the pre-equilibrium stage of the interaction one or more locally thermalized regions may be formed with sufficient energy to lead to evaporation of a neutron or possibly a proton.

The picture becomes more complicated for the case of nuclear fission. Although it is true that increasing excitation facilitates surmounting the fission barrier, i.e. the fission cross-section is an increasing function of the excitation energy, this is only a small piece of the total picture. Nuclear fission is known to be a strongly over-damped process, with energy flowing from the collective to the intrinsic modes (nuclear dissipation) right up to the point of scission. Additionally, as energy accumulates in the intrinsic degrees of freedom, i.e. as the system heats up, there is an increasing probability that some of the energy will be released through particle emission. Thus the system may never reach full thermal equilibrium prior to scission. With these features in mind it seems unlikely that a model requiring a fully equilibrated source would be able to adequately describe all of the important features of the process.

1.2 Probes of Nuclear Fission Dynamics

Aside from its intrinsic interest as a specific decay mode, nuclear fission is an ideal means to study the dynamics of large-scale collective motion of nuclear matter over a wide range of excitation. There are three commonly employed probes of the dynamical nature of nuclear fission:

  · The kinetic energies of the fission fragments

  · The multiplicity of neutrons emitted prior to scission

  · The probability and characteristics of ternary fission.

While the first two will be discussed briefly to provide perspective, the third probe of fission dynamics, ternary fission, is the primary focus of this work.

1.2.1 Total Kinetic Energy of the Fission Fragments

Immediately after scission, the two primary fission fragments are accelerated under the influence of their mutual Coulomb repulsion. A large fraction of the final kinetic energies of the two fragments is a result of this initial Coulomb repulsion. Only about 5–10 MeV can be attributed to kinetic energy along the scission coordinate (the motion of the two nascent fragments just prior to scission). Immediately after scission, the Coulomb potential, V_c, between the two fission fragments is related to their atomic numbers, Z_1 and Z_2, and the distance between their charge centers, R, by Coulomb's law

$$V_c \propto \frac{Z_1 Z_2}{R}. \tag{1.1}$$

An empirical correlation, similar in form to Eq. 1.1, between the total kinetic energy of the two fission fragments and the liquid-drop-model Coulomb parameter $Z^2/A^{1/3}$ of the parent nucleus has been developed and refined over the years [15, 16, 17, 18]. Figure 1.2 is a plot of the most probable kinetic energy release, $\langle E_K \rangle$, in the center-of-mass of the fission nucleus *vs.* the Coulomb parameter for a large number of fissioning systems over a range of excitation energies. The energies are averaged
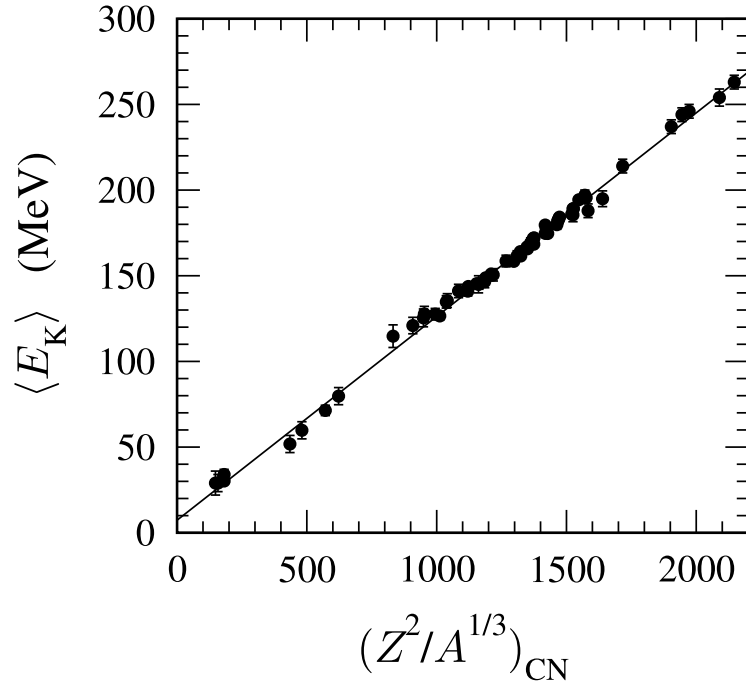
Figure 1.2: Dependence of the mean fission fragment kinetic energy release, $\langle E_K \rangle$ as a function of the liquid-drop-model Coulomb parameter, $\left(Z^2/A^{1/3} \right)_{CN}$, of the fissioning nucleus. The solid line represents the most recent fit to the experimental data. [15].

over all mass asymmetries of the fission fragments. The solid line is the result of a least squares fit to the data, which leads to the relation:

$$\langle E_K \rangle = 0.1189 \, \frac{Z^2}{A^{1/3}} + 7.3 \text{ MeV}$$

where Z and A refer to the fissioning nucleus. This seemingly simple expression, commonly referred to as the Viola systematics, can be used to deduce the separation of the two heavy fragments at scission by performing a transformation of the dependent variable giving:

$$\langle E_K \rangle = 0.755 \, \frac{Z_A Z_B}{A_A^{1/3} + A_B^{1/3}} + 7.3 \text{ MeV}.$$

where the quantities $A_{\mathrm{A}}^{1/3}$ and $A_{\mathrm{B}}^{1/3}$ can be related to the spherical radii of the two fragments by the relation $R_i \propto A_i^{1/3}$. Comparison of the extracted values of R_i with measured nuclear radii can then provide information on the shape at scission. The observed variance of the fragment kinetic energies, as indicated by the error bars in Fig. 1.2, reflects the variation in both the mass asymmetry, $Z_{\mathrm{A}} Z_{\mathrm{B}}$, and the nuclear elongation, $R_{\mathrm{A}} + R_{\mathrm{B}} \propto A_{\mathrm{A}}^{1/3} + A_{\mathrm{B}}^{1/3}$, at the scission point. Thus, it is possible to extract at least qualitative information about the scission configuration, i.e. how stretched the system is at scission, and from this gain some insight concerning the nature of the nuclear dissipation [13], directly from the fission fragment energy spectra.

1.2.2 Pre-Scission Neutron Emission

Prior to scission, an excited heavy nucleus can decay by statistical emission of neutrons. Pre-scission neutrons can be distinguished from neutrons emitted post-scission by examination of their angular distribution relative to the direction of motion of the accelerated fission fragments. The multiplicity of pre-scission neutrons, M_n^{pre}, depends on the lifetime of the system prior to scission, τ_{pre}. The mean evaporation time for one neutron, defined as $\tau_n = \hbar/\Gamma_n$ where Γ_n is the neutron decay width, is an exponentially decreasing function of the instantaneous excitation energy of the emitting system as shown in Fig. 1.3. The neutrons are assumed to be emitted sequentially from the excited nucleus, with an increasing mean time between emissions as the available excitation energy decreases. In theory, the pre-scission lifetime can then be determined by summing the emission times of the pre-scission neutrons in the event

$$\tau_{pre} = \sum_{i=1}^{M_n^{pre}} \tau_{n,i} = \sum_{i=1}^{M_n^{pre}} \frac{\hbar}{\Gamma_{n,i}}.$$

In practice this requires fitting the measured neutron energy spectra, usually using statistical evaporation model calculations. In the early development of this "neutron clock" technique the model calculations used a static approach in which the partial decay widths, $\Gamma_{n,i}(E^*)$, were calculated assuming an evaporation cascade be-
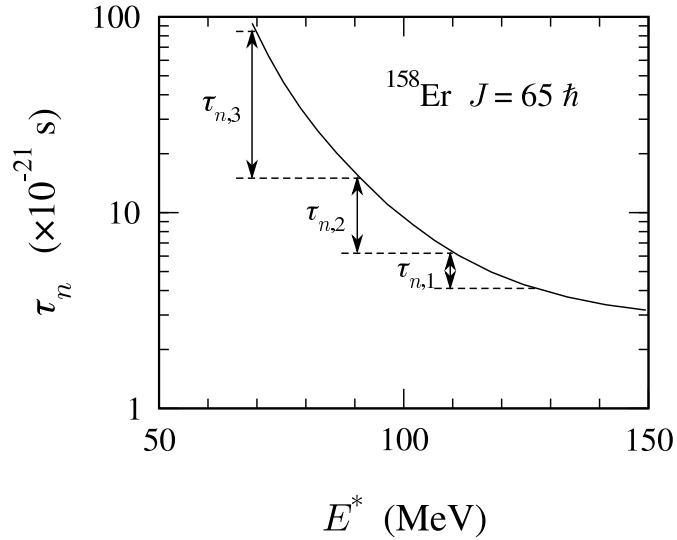
Figure 1.3: Dependence of the neutron evaporation time on excitation energy of the emitting system. The time interval of the neutron clock is the mean evaporation time for one neutron, $\tau_n = \hbar/\Gamma_n$, which is an exponentially decreasing function of the excitation energy, E^*, of the emitting system.

ginning with a fully thermalized system [19, 20]. More recent work in this area has shown that the deduced time scales depend strongly on the assumed initial conditions used in the evaporation calculations. Efforts have been made to account for entrance channel dynamics by incorporating dynamic models to describe the non-instantaneous transfer of energy to the intrinsic modes [21, 8]. This approach allows for the possibility of statistical decay during the formation time of the composite system, i.e. the system may never achieve the maximum possible excitation energy. These efforts have lead to fission time-scales that can differ by as much as an order of magnitude from those obtained assuming strictly statistical evaporation from a fully thermalized source [22].

The pre-scission time determined from M_n^{pre} is actually the time from the moment when the system has achieved sufficient excitation to make neutron evaporation

energetically possible until shortly after the moment of scission. At least in theory the pre-scission time can be further broken down to a pre-saddle time, τ_{sad}, and a saddle-to-scission time, τ_{ssc} (see Fig. 1.1), the latter of which depends sensitively on the nature (one-body *vs.* two-body) and magnitude of the nuclear dissipation. To date there is no reliable experimental method to differentiate pre-saddle neutrons from those emitted during the decent from saddle to scission.

Experimentally measured pre-scission neutron multiplicities as high as 6–8 per fission event have been observed. In light of the results presented in Fig. 1.3 this observation would indicate that fission lifetimes are long compared to that for a typical single particle transition. This is not surprising when one considers the substantial nucleon rearrangement necessary to achieve the deformations realized in fission. The fission lifetime is also influenced by dissipative forces that impede the collective motion toward scission. More recent dynamical model calculations have been used to extract viscosity coefficients by reproducing experimental pre-scission neutron multiplicities. The values for the viscosity coefficient determined from these calculations cover the range of 0.03–0.06 Tp (terapoise) for systems of mass 150–200 [23]. For comparison, the viscosity of water is 1.002 cp (centipoise) at 20° C, which is less than the calculated nuclear viscosity by a factor of $\sim (3–6) \times 10^{12}$.

1.2.3   Ternary Fission

Ternary fission presents a good choice for studying the interplay of dynamical and statistical effects in nuclear decay. The low excitation energies usually involved in ternary fission studies limit the number of available exit channels, which can simplify interpretation of the data. At low excitation energies the observed relative probability for ternary fission compared to binary fission is of the order 10^{-2}–10^{-3}. At higher excitation, as more decay channels become available, the ternary fission channel becomes buried beneath the higher probability for binary and fast non-fission processes, making it increasingly more difficult to isolate true ternary fission events. A cartoon of particle-induced ternary fission is presented in Fig. 1.4. In this picture
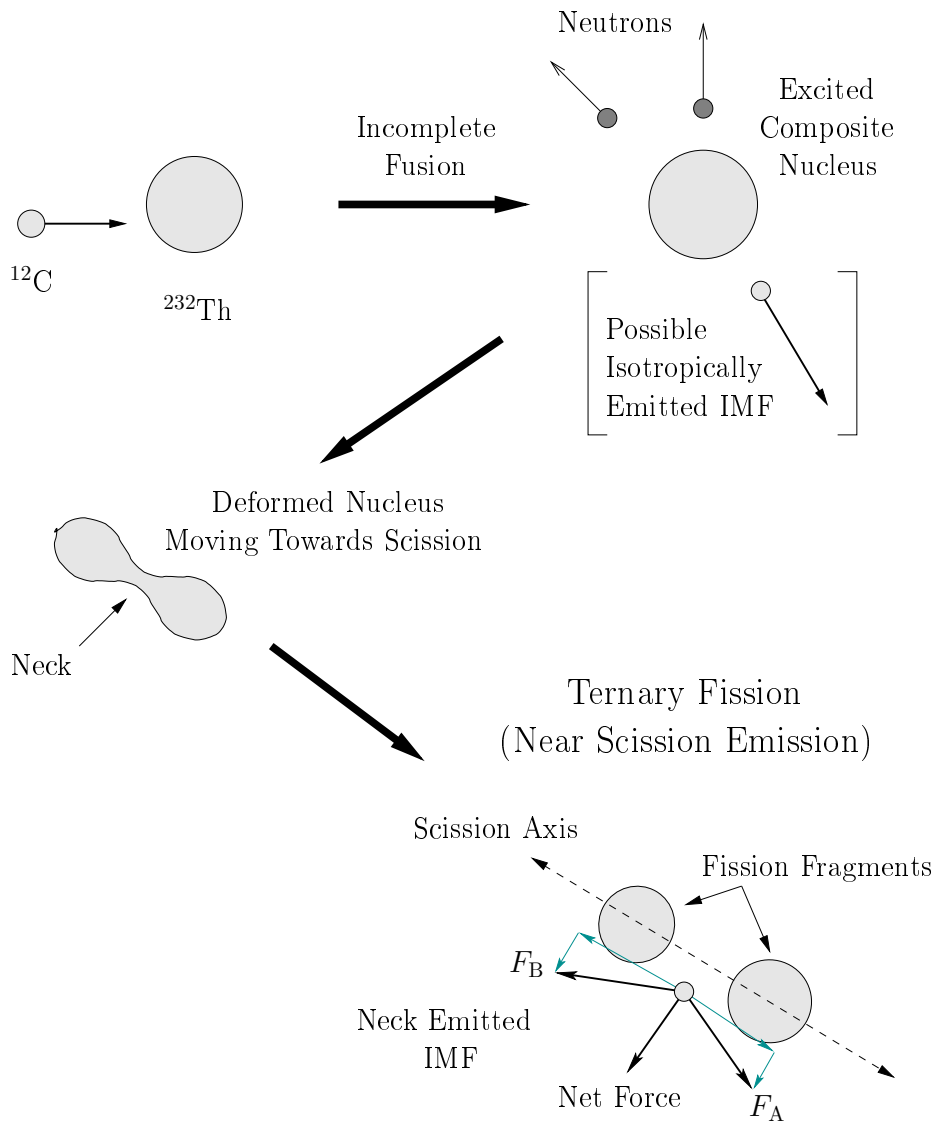
Figure 1.4: Cartoon depicting the ternary fission process. Partial cancellation of the components of the Coulomb forces, F_A and F_B, parallel to the scission axis results in a reduced net force acting on the neck emitted IMF. Parallel and perpendicular components of F_A and F are indicated by the light gray arrows. The partial cancellation of the Coulomb forces also gives rise to the observed angular focusing with respect to the scission axis.

the final energies and angular distributions of fragments emitted near scission from the neck region are expected to be sensitive to the initial separation and velocities of the two heavy fission fragments at the moment of scission.

1.3   Experimental Signatures of Ternary Fission

Figure 1.5 shows the laboratory kinetic energy spectra for ^{10}Be fragments observed in coincidence with two heavy fission fragments in the reaction ^{3}He + ^{232}Th at 270 MeV [10]. Each panel represents the energy spectrum obtained at a different laboratory angle with respect to the beam axis, as labeled in the upper right of each panel. The numbers in parenthesis in each panel are the approximate angles with respect to the scission axis of the coincident fission fragments as defined by two position-sensitive fission fragment detectors centered at laboratory angles of +96° and -64° with respect to the beam axis. The spectrum in panel (a) is for ^{10}Be fragments observed approximately orthogonal ($\sim 90°$) to the scission axis. At this angle the energy spectrum appears to be bimodal, with a significant yield of low energy fragments ($\langle E_{\mathrm{IMF}} \rangle \approx 18$ MeV indicated by the arrow marked Low) in addition to a higher energy component ($\langle E_{\mathrm{IMF}} \rangle \approx 35$ MeV indicated by the arrow marked High). In contrast, for the energy spectra in panels (b) – (d), observed at angles non-orthogonal to the scission axis, the low energy component is strongly suppressed, while the high energy component is almost identical in terms of both the total number of counts and the location of the peak. The location of the peaks in the latter spectra, and the high energy peak in panel (a) is consistent with the Coulomb barrier for emission from a compact source similar in atomic number to the target nucleus. The low energy peak in panel (a) is more consistent with emission from an extended source, similar to the cartoon for ternary fission in Fig. 1.4.

Panel (a) of Fig. 1.6 shows the laboratory angular distribution of ^{10}Be fragments observed in coincidence with two heavy fission fragments [10]. In this plot, the high energy ^{10}Be fragments (open circles) appear to be emitted more or less isotropically, independent of the orientation of the scission axis, while the distribution for the low
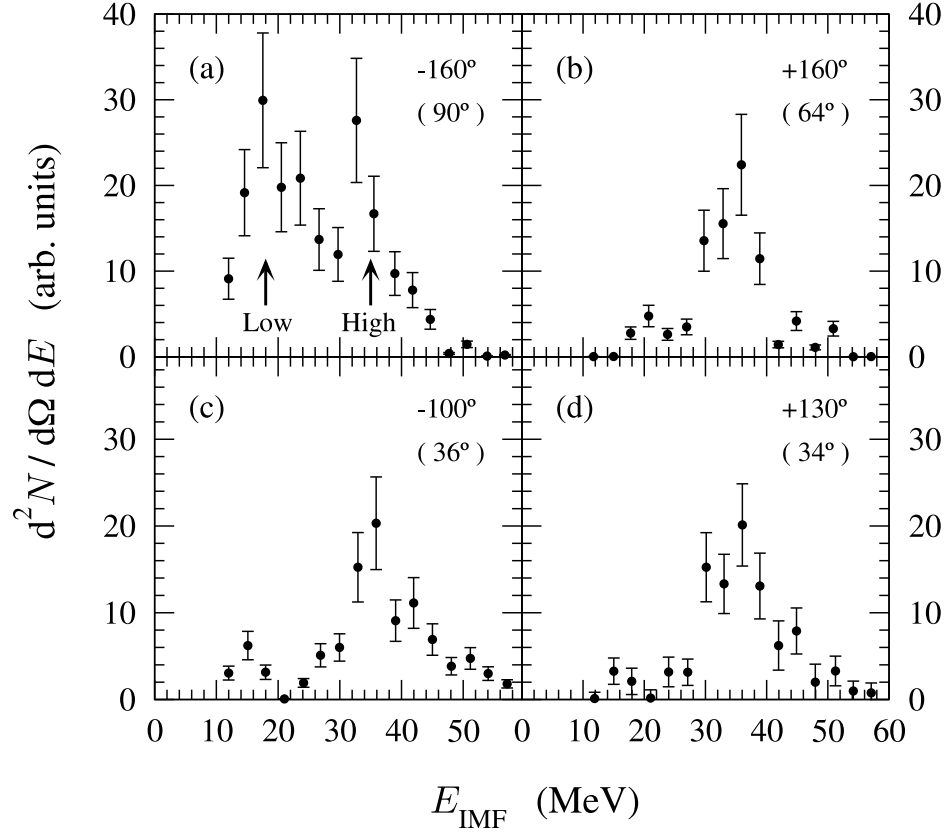
Figure 1.5: Laboratory kinetic energy spectra of ^{10}Be fragments observed in coincidence with two heavy fission fragments in the reaction ^{3}He + ^{232}Th at $E_{\text{lab}} = 270$ MeV [10]. Fragments were observed at backward angles, listed in each panel, with respect to the beam direction. The spectrum in panel (a) corresponds to angles orthogonal to the scission axis, which was defined by two position sensitive fission fragment detectors centered at +96° and -64°.

energy fragments (closed circles) is peaked near an angle of 97° relative to the scission axis, which corresponds to an angle of $\sim 90°$ in the center-of-mass of the fissioning system. To further clarify the angular peaking we constructed a plot of the ratio of the laboratory angular distribution data of the low energy ^{10}Be fragments to that for the high energy fragments, using the data plotted in panel (a). The result is presented in panel (b) of Fig. 1.6. The ratio more clearly demonstrates the enhancement of the yield of low energy fragments near angles orthogonal to the scission axis.

The peaking in the angular distribution of the low energy fragments can be understood by assuming that emission occurs very close to the moment of scission, when the combined Coulomb field of the two heavy fission fragments would have a strong focusing effect on the trajectory of the ternary fragment. Furthermore, that the angular distribution of the low energy fragments is peaked *orthogonal* to the scission axis indicates that these fragments must originate from the neck region, between the two nascent heavy fragments, and are not evaporated from the accelerated heavy fragments.

1.4   Models of Nuclear Fission

Numerous attempts have been made to model the nuclear fission process, both binary and ternary, with varying degrees of success (see [24] and references therein for a more complete overview). The degree of success for any model is determined by the ability of the model to reproduce the important experimentally measured quantities for the process under investigation. For the case of nuclear fission we can immediately list several experimentally measured quantities that should be reproduced by a model. Among these quantities are the kinetic energies, mass yields and angular distributions of the fission fragments and, for the case of ternary fission, the kinetic energies, mass yields and angular distributions of the ternary fragments. The remainder of this section provides a brief introduction to several of the more important models that attempt to describe ternary fission.
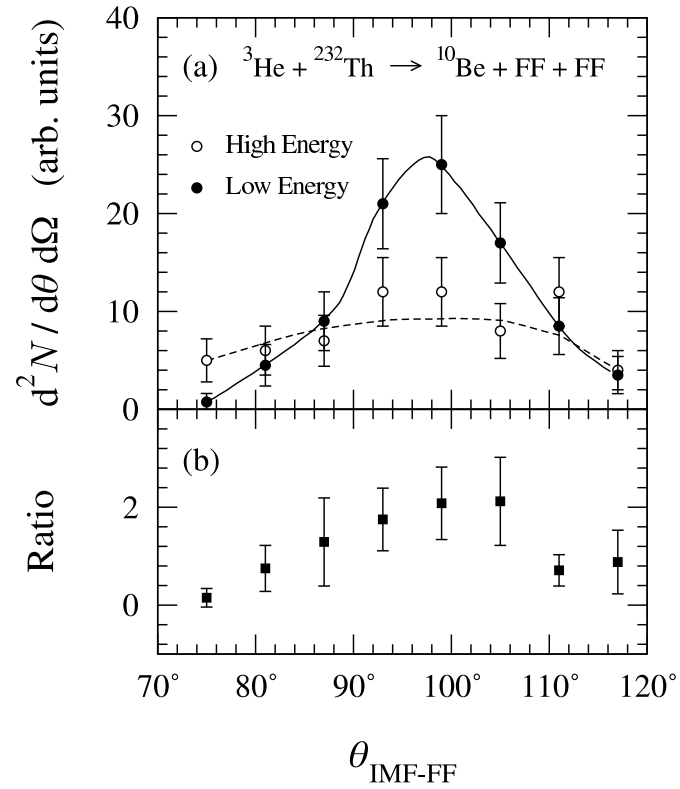
Figure 1.6: Panel (a): laboratory angular distribution relative to the scission axis for [10]Be fragments observed in coincidence with two heavy fission fragments in the reaction ^{3}He + ^{232}Th at $E_{\text{lab}} = 270$ MeV [10]. Closed circles represent data for low energy fragments and open circles represent data high energy fragments. Panel (b): ratio of the angular distribution data of the low energy [10]Be fragments to that for the high energy fragments.

1.4.1 Explaining Ternary Fission Yields with Energetics Considerations

A common theme in physical processes is that the probability for moving from an initial state to a particular final state is inversely proportional to the energy required to make the transition. This base probability can be modified by increasing the energy available to the system, thus increasing the probability for the transition. In the "Halpern model" of ternary fission the energy cost E_c for emission of the third particle is determined by starting with a binary scission configuration as shown in the top of Fig. 1.7 [25]. The energy cost is then calculated as the energy needed to remove a particular third particle from one of the two fission fragments and place it midway between the two heavy fragments. The expression used to calculate the energy cost is,

$$E_c = B + \Delta V + K \tag{1.2}$$

where B is the average binding energy of the third particle to its mother fragment, ΔV is the average difference in Coulomb potential energy between the corresponding binary and ternary configurations and K is the average kinetic energy with which the third particle is released. The binding energy B is computed from mass tables. The last two terms on the right side of Eq. 1.2 can be varied to reproduce experimental results. In particular, the change in Coulomb potential depends on the separation parameter d as defined in Fig. 1.7 - an increase in the separation parameter will result in a decrease in the energy cost. The dependence of the Coulomb potential on the separation d leads to an important, although perhaps only qualitative insight into the ternary fission process: heavier ternary fragments will preferentially result from more stretched scission configurations, where the energy cost is lower and, additionally, more of the available energy is stored in the deformation of the system. Typical values for the calculated energy cost are ~ 21 MeV for ^{4}He and ~ 43 MeV for ^{10}Be [25], which is a significant fraction of the total available energy.

The energy cost described by Eq. 1.2 is an increasing function of the mass of the ternary particle. This would indicate that the yields for the various ternary particles
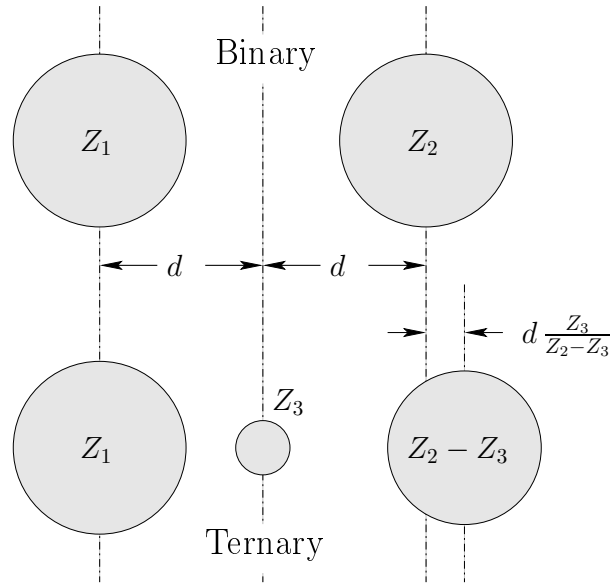
Figure 1.7: Geometry used in the Halpern model of ternary fission. The third particle (Z_3) is removed from one of the binary fragments (Z_2) and placed at a point midway between Z_1 and Z_2 while the residual fragment ($Z_2 - Z_3$) is displaced slightly in order to keep the same center of mass in both configurations.

should be a decreasing function of the energy cost, i.e.

$$Y \propto \exp(-\text{const} \cdot E_c).$$

In order for the energy required for the release of the ternary particle to be readily available, it must be stored in a very few degrees of freedom. The initial storage is generally considered to be in the deformation of the system. This idea implies two important relations between the ternary particle yields and the shape of the parent nucleus at scission. First, if we assume that the decision to breakup into three instead of two fragments, not counting neutrons, is based primarily on the energetics at scission, then events in which more energy is stored in deformation, i.e. more stretched scission shapes, should in general have a higher probability for ternary breakup than events with a more compact scission shape. Second, since

the energy cost is an increasing function of the size of the ternary fragment, we would again expect that larger ternary particles should be preferentially associated with more stretched scission shapes compared to those for smaller ternary particles. Furthermore, the transfer of energy from deformation to create the ternary particle most probably occurs on a very short time scale. A slow transfer of energy would tend to heat the system as a whole as energy is lost to internal degrees of freedom. Requiring that the energy transfer occur on a very short time scale implies that ternary fission is a non-adiabatic process. Results of calculated yields based on the Halpern model are compared to experimental results in Fig. 1.8. The Halpern model results were calculated using a scission configuration with a tip distance $D = d - R_1 - R_2 = 8.7$ fm, where d is the center-to-center distance as defined in Fig. 1.7 and R_1 and R_2 are the effective radii of adjacent fragments 1 and 2. As can be seen the Halpern model is successful in reproducing the gross features of the relative yields of ternary particles.

1.4.2 Nuclear Dynamics: Surface Instabilities and Random Neck Rupture

Since its discovery, nuclear fission has been described in terms of hydrodynamics, i.e. the division of a uniformly charged drop of nuclear 'fluid' into two smaller droplets [28, 29]. In this picture an initially spherical parent nucleus becomes deformed into a series of rotationally invariant shapes. As the parent nucleus becomes more deformed, there is an increasing probability that a neck will develop somewhere along the length of the extended shape. Once formed, the diameter of the neck rapidly decreases until the nuclear drop breaks into two smaller droplets. Theories developed from this rather simple picture generally vary in the parameterization used to describe the non spherical nuclear shapes, but the hydrodynamic description remains a powerful, and popular tool in attempts to model various aspects of nuclear fission.

In his seminal paper in 1878 Lord Rayleigh consolidated and expanded on the
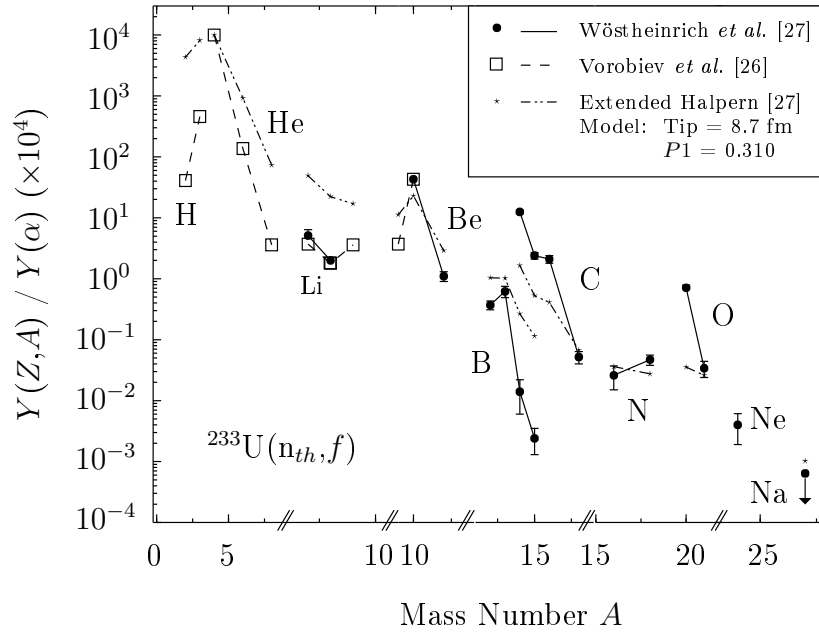
Figure 1.8: Comparison of Halpern-model predictions with experimental yields from thermal-neutron-induced ternary fission. The yields are plotted relative to the yield of ternary α-particles, which was arbitrarily normalized to 10^4. Arrows indicate upper limits. From Ref. [27].

---

earlier work of Joseph Plateau. Rayleigh demonstrated that long, homogeneous, uncharged liquid jets confined by surface tension are unstable with respect to breakup into droplets [30] (see Fig. 1.9). The driving force behind this capillarity instability is a net gain in surface energy, that is the separate droplets have less total surface area than the original cylindrical jet. A necessary pre-condition for this process is the existence of small random fluctuations of the surface shape, which Rayleigh and others modeled as small, azimuthally symmetric sinusoidal distortions of the surface (assuming the z-axis to be defined by the symmetry axis of the cylindrical jet). The small fluctuations are precursors of the eventual breakup, their location at the time of onset of the instability determining the breakup geometry. The condition for onset of the capillary instability was determined by Rayleigh to be that in which an
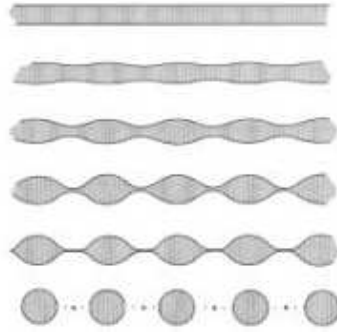
Figure 1.9: Plateau-Rayleigh instability of a long liquid jet.

increase in the amplitude of the small surface distortions results in a reduction in
the total surface area per unit length of the jet. This condition is satisfied by the
expression

$$\lambda \geq \lambda_\circ = 2\pi r_\circ. \tag{1.3}$$

Thus, long liquid jets become unstable with respect to breakup into several droplets
if the wavelength of the initial surface distortion, λ, exceeds the mean circumference
of the jet, $2\pi r_\circ$.

The capillarity, or Rayleigh instability, should be equally applicable to short
liquid jets, such as an extended heavy nucleus. As with any macroscopic liquid,
the nuclear fluid can be ascribed a surface tension, resulting from the nuclear mean
field, which prevents individual nucleons from easily escaping the boundaries of the
nucleus. In macroscopic systems an extended body of liquid, finite or infinite, is
subject to Rayleigh type instabilities that will lead to breakup into two or more
smaller fragments. In this case, however, the condition for onset, Eq. 1.3, needs to
be modified to account for the finite size of the system, as well as the fact that the
nucleus has a non-zero charge. Taking these factors into account, the condition for
onset becomes [31]

$$\frac{2\pi r}{l} \gtrsim \frac{3x^2}{2} \tag{1.4}$$
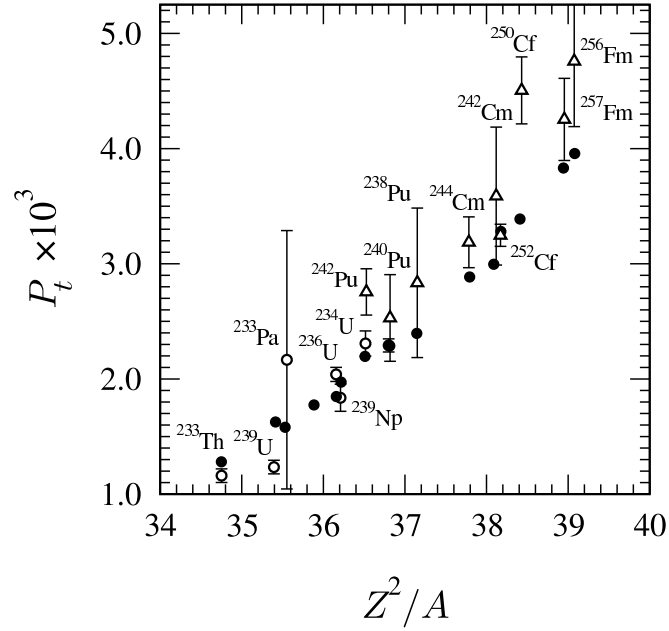
Figure 1.10: Influence of the fissility parameter of the fissioning system, Z^2/A, on the relative probability of ternary fission. Triangles represent experimental data for spontaneous fission, open circles are for particle-induced fission and closed circles are theoretical values. From Ref. [14].

---

where r is the minimum radius of the neck, l is the total length of the system and $x \approx 0.02 \, Z^2/A$ is the fissility of the parent nucleus. The relation expressed in Eq. 1.4 provides only the most general description of the shape of the extended nucleus for which the capillarity instability comes into play. The "random neck rupture" model utilizes the criterion expressed in Eq. 1.4, together with a second, shift instability, and describes the mechanism of nuclear fission as the dynamical development of Rayleigh surface instabilities on a roughly cylindrical nucleus [32, 33, 13]. The addition of the shift instability in the random neck rupture model provides a mathematical description of the variation in the location along the extended nucleus at which the capillarity instability occurs.

For the case of ternary fission the random neck rupture model has been extended
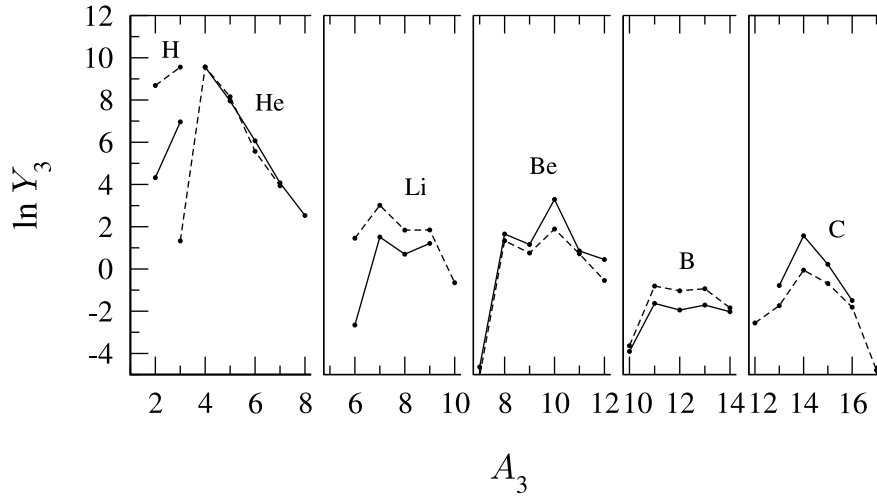
Figure 1.11: Yields of ternary particles in the double-neck-rupture model for thermal neutron induced ternary fission of ^{236}U. A_3 is the mass and Y_3 the yield of the ternary fragments. Solid lines indicate experimental data while dashed lines indicate calculated yields [14].

to the so-called "double-neck-rupture" model [14]. In this view, ternary fission is the result of two statistically independent random neck ruptures, occurring during a time interval on the order of one single-particle period, $\Delta t \simeq \tau_{\text{sci}} \simeq$ single particle period. A comparison of the experimentally measured relative probability for ternary fission, P_t, with values calculated within this physical picture is shown in Fig. 1.10 as a function of the fissility parameter of the fissioning system, Z^2/A. The model clearly reproduces the observed overall increase in the ternary fission probability with increasing fissility. The double-neck-rupture model has also proven successful at reproducing the experimental isotopic yields of ternary particles, as shown in Fig. 1.11, where A_3 is the mass and Y_3 the yield of the ternary fragment.

1.4.3 Nuclear Dynamics: Dissipation

An important question that has received much attention over the years is the nature and magnitude of nuclear dissipation. There is also a question as to the temperature

dependence of the nuclear dissipation. The details of the temperature dependence may provide a means to determine the nature (one-body *vs.* two-body) of the nuclear dissipation. Recent dynamical models, many based on classical Hamiltonian equations of motion and focusing on a limited number of collective coordinates, have been used to investigate these questions. One such model, the Macroscopic Dynamical Model [34, 35], will be covered in some detail in Ch. 5.

1.5   New Insights

To date the vast majority of the experimental work has been limited to the study of low energy (spontaneous, thermal neutron and light-ion induced) ternary fission. In the current work we investigate the important features, ternary fragment energies, angular distributions, and yields, for heavy-ion-induced ternary fission. The higher excitation energies and angular momenta obtainable in heavy-ion induced reactions may provide further insight into the importance of both entrance channel dynamics (incident orbital angular momentum) and the temperature dependence of nuclear dissipation.

References

[1] V. Weisskopf and D. Ewing, Phys. Rev. **57**, 472 (1940).

[2] L. Sobotka *et al.*, Phys. Rev. Lett. **51**, 2187 (1983).

[3] D. Hill and J. Wheeler, Phys. Rev. **89**, 1102 (1953).

[4] J. Zhang *et al.*, Phys. Rev. C **56**, 1918 (1997).

[5] J. Tõke *et al.*, Phys. Rev. Lett. **77**, 3514 (1996).

[6] R. Yanez *et al.*, Phys. Rev. Lett. **82**, 3585 (1999).

[7] V. Viola, Nucl. Phys. **A471**, 53c (1987).

[8] M. Thoennessen, Nucl. Phys. **A599**, 1c (1996).

[9] D. Hilscher, Phys. At. Nucl. **57**, 1187 (1994).

[10] D. Fields *et al.*, Phys. Rev. Lett. **69**, 3713 (1992).

[11] S. Chen *et al.*, Phys. Rev. C **54**, 2114 (1996).

[12] B. Lindl, Z. Phys. A **328**, 85 (1987).

[13] U. Brosa, S. Grossmann, A. Müller, and E. Becker, Nucl. Phys. **A502**, 423c (1989).

[14] V. Rubchenya and S. Yavshits, Z. Phys. A **329**, 217 (1988).

[15] V. Viola, K. Kwiatkowski, and M. Walker, Phys. Rev. C **31**, 1550 (1985).

[16] J. Terrell, Phys. Rev. **113**, 527 (1959).

[17] V. Viola and T. Sikkeland, Phys. Rev. **130**, 2044 (1963).

[18] V. Viola, Nucl. Data Tables **A1**, 391 (1966).

[19] D. Hinde *et al.*, Phys. Rev. C **45**, 1229 (1992).

[20] D. Hilscher and H. Rossner, Annales de Physique Fr. **17**, 471 (1992).

[21] K. Siwek-Wilczyńska, J. Wilczyński, R. Siemssen, and H. Wilschut, Phys. Rev. C **51**, 2054 (1995).

[22] K. Siwek-Wilczyńska, J. Wilczyński, R. Siemssen, and H. Wilschut, Nucl. Phys. **A583**, 141 (1995).

[23] C. Bhattacharya, S. Bhattacharya, and K. Krishan, Phys. Rev. C **53**, 1012 (1996).

[24] *Proceedings of the International Conference on Fifty Years Research in Nuclear Fission*, edited by D. Hilscher, H. Krappe, and W. von Oertzen (North-Holland, Amsterdam, 1989), published as Nucl. Phys. **A502**.

[25] I. Halpern, Ann. Rev. Nucl. Sci. **21**, 245 (1971).

[26] A. Vorobiev *et al.*, Phys. Lett. **B30**, 322 (1969).

[27] M. Wöstheinrich *et al.*, Acta. Phys. Slovaca **49**, 117 (1999).

[28] L. Meitner and O. Frisch, Nature (London) **143**, 239 (1939).

[29] N. Bohr and J. Wheeler, Phys. Rev. **56**, 426 (1939).

[30] J. Rayleigh, Proc. London Math. Soc. **10**, 4 (1878).

[31] U. Brosa and S. Grossmann, Phys. Lett. **126B**, 425 (1983).

[32] U. Brosa and S. Grossmann, Z. Phys. **A 310**, 177 (1983).

[33] U. Brosa and S. Grossmann, J. Phys. G **10**, 933 (1984).

[34] N. Cârjan, A. Sierk, and J. Nix, Nucl. Phys. **A452**, 381 (1986).

[35] N. Cârjan (private communication).

Chapter 2

Detectors

Accurate reconstruction of the reaction kinematics on an event-by-event basis required coincident detection of the two correlated fission fragments along with any low energy intermediate mass fragments (IMFs: $3 \leq Z \leq 20$) emitted at backward angles with respect to the beam axis. In this experiment several quantities were measured simultaneously for both the fission fragments and the IMFs. For the two fission fragments it was important to measure the emission angle and velocity of each fragment. For the IMFs the quantities of interest were the atomic number, emission angle, velocity and kinetic energy. Since the IMFs of interest were to be detected at backward angles, it was also necessary to use a detector with a very low energy threshold to account for the center-of-mass motion of the system. These requirements were satisfied by two types of detectors: a large area, hybrid parallel-plate avalanche counter - multi-wire proportional counter (PPAC-MWPC) for the detection of the fission fragments and a low threshold ionization-chamber/Si(IP)/CsI(Tl) telescope (IC telescope) for the detection of IMFs.

2.1 Introduction to Gas-Ionization Detectors

Both the PPAC-MWPC and IC telescopes used in the current work are gas detectors in which incident radiation ionizes the gas thus providing detection capability. The
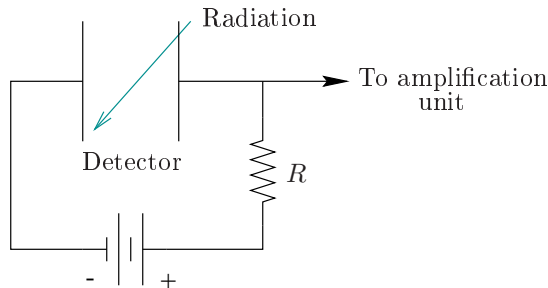
Figure 2.1: Schematic of a simple, pulse mode gas ionization chamber.

simplest form of such a detector is essentially a parallel-plate capacitor in which the region between the plates is occupied by the gas able to be ionized. A schematic diagram for a simple, pulse-mode gas-ionization chamber is shown in Fig. 2.1, where each ionizing event results in an independent signal. As ionizing radiation passes through the gas volume, it dissipates some or all of its energy in collisions with the gas molecules, creating electron-ion pairs. In the absence of an electric field between the parallel plates, the motion of the electrons and positive ions would be random, and the electrons and ions would eventually recombine to form neutral molecules. In this scenario there would be no net flow of charge carriers (electrons or positive ions) and thus no signal could be extracted from the detector. However, when a voltage is applied between the plates the electrons are accelerated and acquire a net velocity v, in the direction of the anode plate. Likewise, the positive ions acquire a net velocity in the direction of the cathode plate. The space-charge resulting from the creation of the electron-ion pairs, as well as their subsequent motion within the electric field, causes an induced current at the electrode plates. This induced current continues to flow until all of the charge has been collected. Measurement of the induced current provides the detector signal.

The electron drift velocity varies as a function of the reduced electric field strength, X/p, where X is the electric field strength between the two plates in V/cm and p is the gas pressure [1]. It can be approximately calculated by the classical

kinetic theory expression

$$v = \frac{e\lambda X}{mup},$$ (2.1)

where, in addition to the electric field strength and pressure described above, e is the electron charge, λ is the mean free path of the electrons in the gas, m is the electron mass, and u is their RMS agitation velocity. Thus, it is clear that one can improve the time resolution of a gas detector by either decreasing the gas pressure and/or increasing the potential difference across the gap between the plates. Indeed, it has been demonstrated that low pressure gas-ionization detectors offer superior time resolution compared to the same detector type operated at higher pressures [2]. Time resolution as good as 175 ps has been reported for very low pressures (2 Torr isobutane) [3].

The drift velocity of the positive ions can be described by an expression similar to that used to describe the motion of the electrons:

$$v^+ = \mu^+ \left(\frac{X}{p}\right),$$ (2.2)

where μ^+ is the mobility of the ion in the gas. With X in units of V/cm and p in atm, the ion mobility generally has a value near unity. This means that the collection time for the more massive positive ions is about 1000 times greater than that for the electrons. Because of this, gas detector designs that require fast timing use the electron collection to provide the time signal.

2.2 General Principles of Gas Amplification

The behavior of a gas-ionization detector varies as a function of the magnitude of the applied electric field. With all other parameters being fixed (detector geometry, gas pressure and type, etc.), it is possible to identify several distinct regions of amplification which depend on the applied voltage as shown in Fig. 2.2.

Region I. At very low voltage the electrons and ions produced by the ionizing radiation move with relatively slow speeds, and the rate of recombination is high. As the voltage increases, the electric field strength increases, the charge carriers move
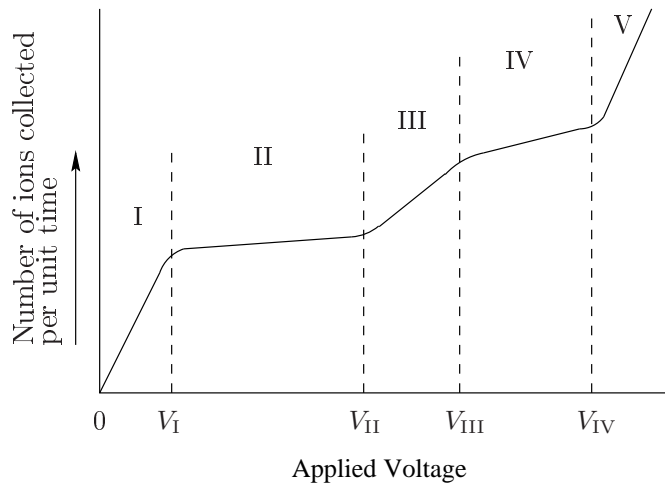
Figure 2.2: Relationship between collected charge and applied voltage in a gas-ionization detector. The different regions are defined in the text.

---

faster, and the rate of recombination decreases toward zero. This region is referred to as the *recombination* region. The voltage V_I is the point at which the rate of recombination is zero, and all of the charge created by the ionizing radiation is being collected at the electrodes.

Region II. As the applied voltage is increased, the rate of recombination decreases to zero, and the collected charge increases to and saturates. All electrons collected at the anode are the result of primary ionizing events, those that resulted directly from interactions between the radiation and the gas molecules. This region is referred to as the *ionization* region, where the amount of charge collected is directly proportional to the amount of energy deposited in the gas, with no internal amplification.

Region III. In this region, the rate of charge collection, as well as the total amount of charge collected, begins to increase. The electric field has become so strong that, in a certain region of the gas volume, electrons formed through primary ionization acquire sufficient kinetic energy between collisions to produce additional

ionization of the gas. The ratio of the total ionization produced to the primary ionization, the gas multiplication factor, is, for a fixed voltage, independent of the amount of primary ionization. Thus the total amount of charge collected remains proportional to the amount of primary ionization, and therefore the amount of energy deposited in the gas. This region is called the *proportional* region.

Region IV. The electric field in this region is so strong that the creation of a single electron-ion pair will initiate an avalanche effect, resulting in a strong signal that is independent of the amount of primary ionization. Because the final signal is not proportional to the amount of primary ionization, particle identification and energy measurement are no longer possible. A detector operating in this region, referred to as the *Geiger-Müller* (GM) region, is only useful for counting the number of events, while providing no information as to the nature of the ionizing radiation.

Region V. If the applied voltage is increased beyond V_{IV} in Fig. 2.2, a single ionizing event will initiate a continuous discharge in the gas. At this point the device is no longer useful as a radiation detector without the addition of a means to quench the discharge between detection events.

Of the two detector designs used in the present work, the PPAC-MWPC operates in the *proportional* region, where the signal is amplified through secondary ionization, but is still proportional to the energy deposited in the gas by the fission fragments. The ion chamber portion of the IC telescope operates in the *ionization* region, where the signal is proportional to the deposited energy, but there is no internal signal amplification.

2.3 Construction and Operating Characteristics of the Parallel-Plate Avalanche Counter - Multi-wire Proportional Counter

The parallel-plate avalanche counter - multi-wire proportional counter (PPAC-MWPC) is a low pressure, transmission-mode gas ionization counter. The good timing and

position resolution obtainable with this detector type makes it ideal for kinematic studies involving detection of fission fragments and other heavy ions [2, 3, 4, 5]. In the current work these detectors were used to measure the velocity and position of fission fragments resulting from intermediate energy heavy ion reactions. The detectors were designed, built and tested by the Nuclear Chemistry group at Indiana University [6]. An exploded transverse view of a PPAC-MWPC is shown in Fig. 2.3. These detectors were designed to be low mass, to allow the possibility of co-incident neutron detection, and easy to disassemble for cleaning and repair. Each PPAC-MWPC is composed of two distinct regions. The first region operates as a multi-wire proportional counter, and the second region operates as a parallel-plate avalanche counter with additional sense wires for position measurement. The active area for this detector design is approximately $9\,\text{cm} \times 17\,\text{cm}$, and the normal operating conditions are a pressure of 4–5 Torr of isobutane and a cathode voltage of -650 V to -700 V.

The multi-wire proportional counter region (MWPC) consists of a plane grid of 68 equally spaced copper-beryllium wires located between, and parallel to, two aluminized mylar cathode foils (see Fig. 2.4). Each wire has a diameter of 50 μm with a spacing of 0.1 inches (2.54 mm) between adjacent wires. This wire plane is referenced as the x-wire plane in Fig. 2.3. The wires are stretched taut and soldered directly onto the printed circuit board (PCB) containing the discrete components of the read-out electronics. Each wire is connected at one end to a tap on a delay line composed of a series of passive LC delay chips (Rhombus Industries model TZB12-5) providing a tap-to-tap delay of 2.0 ± 0.5 ns. The opposite end of each wire is left floating. Both ends of the delay line are connected to ground through a $3\,\text{k}\Omega$ resistor to dissipate the collected charge slowly. The signals are extracted at either end of the delay line through a 10–20 nF capacitor connected in parallel to the grounding resistor (see Fig. 2.3).

The mylar cathode foils (nominal thickness $\approx 0.176\text{mg/cm}^2$) are manually stretched and glued across precision machined G10 frames. The framed cathode foil closest
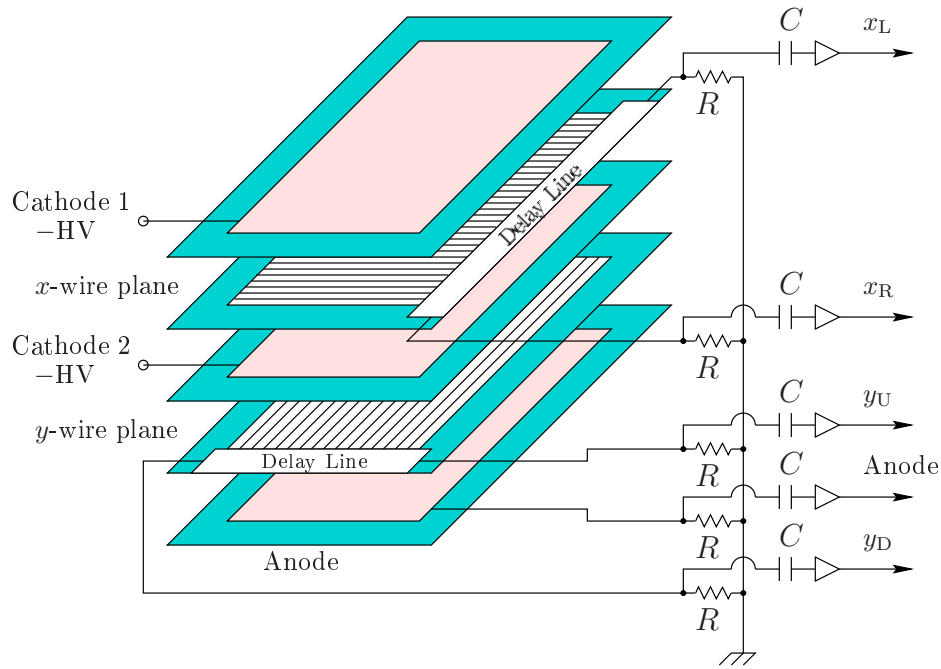
Figure 2.3: Exploded schematic of a PPAC-MWPC used in the ternary fission studies. The delay lines for the wires are shown, as well as the signal readout locations for, y_U, y_D, x_L, and x_R, used to determine position.

to the x-wires in Fig. 2.4 is aluminized only on the side facing the x-wires and is mounted on the same PCB as the x-wires. The second framed cathode foil is mounted on an adjacent PCB, described later. This cathode foil also serves as the cathode for the PPAC region, and therefore is aluminized on both sides. In addition to contact by compression, where necessary silver paint was used to ensure good electrical contact between the aluminized surfaces of the mylar foils and the high voltage trace on the PCB.

As described in Sec. 2.1, ionizing radiation passing through the gas volume creates electron-ion pairs. Due to the strength of the electric field in the vicinity of the wires (as shown in Fig. 2.5) the majority of the charge is collected by the wire nearest to the trajectory of the ionizing particle. Close to the anode wires the potential
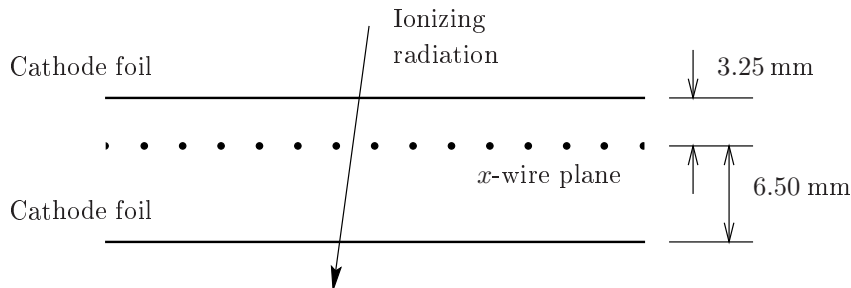
Figure 2.4: Cross-sectional diagram detailing the MWPC region of a PPAC-MWPC used in the ternary fission studies.

---

gradient increases rapidly, allowing the electrons to achieve sufficient kinetic energy to cause secondary ionization of the gas molecules. This "internal amplification" is characteristic of a gas detector operating in the proportional region. Since the total signal resulting from the passage of an ionizing particle will be dominated by the contribution from the wire closest to the ionization track, the position resolution is directly related to the wire spacing. It has further been shown that the absolute position resolution obtainable with a MWPC of this type is on the order of one half the distance between adjacent wires [3, 7]. This position resolution corresponds to an angular resolution of $\approx 0.5°$ and exceeds the experimental requirements ($\theta \lesssim 2°$) of the present work.

Once the signal reaches the LC delay line, it is split, with part of the signal traveling through the delay line in either direction. The difference between the time of arrival of the signal at the two ends of the delay line is directly related to the position of the wire where the signal originated. There is, however, a limit on the coverage that can be obtained with a single detector of this type. The relative amplitudes of the signals extracted at either end of the delay line depends on the impedance as viewed in either direction from the initiating anode wire. For a signal originating from the center wire, the impedance would be roughly equal in either direction. In this case the two extracted signals would be roughly equal in amplitude.
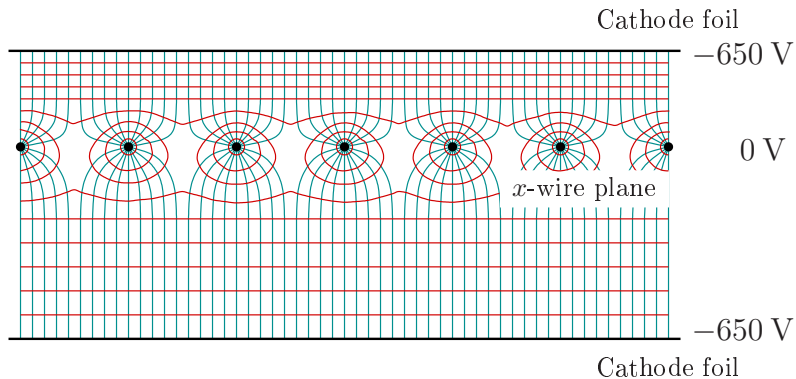
Figure 2.5: Diagram of the electric field lines in the MWPC region. Charged particles move along the electric field lines (lines running from the foils to the wires) to be collected at either the anode wires (electrons) or the cathode foils (positive ions). Close to the anode wires the potential gradient increases rapidly, resulting in a corresponding increase in the acceleration of the electrons (see Eq. 2.1 in Sec. 2.1).

For a signal originating from one of the peripheral wires, the ratio of amplitudes is found to be about 2:1 for this detector design. Thus, for a fixed wire spacing, the delay line will eventually grow to a point where, for a signal originating from a peripheral wire, no signal is seen at the opposite end of the delay line because of the increasing impedance. One possible way to overcome this limitation would be to divide the delay line into multiple sections, with each section covering a limited number of position-sensing wires. However, such a solution would require additional signal processing electronics.

After being read out from either end of the delay line, the signals are passed through a charge-sensitive fast amplifier before being processed through the data-acquisition electronics. The two signals are recorded separately with a time-to-digital converter (TDC), using the anode foil signal from the parallel-plate region (discussed below) or a logic signal as the TDC start. The two times recorded with the TDC are referred to as x_{Left} and x_{Right} to indicate the side of the detector from which
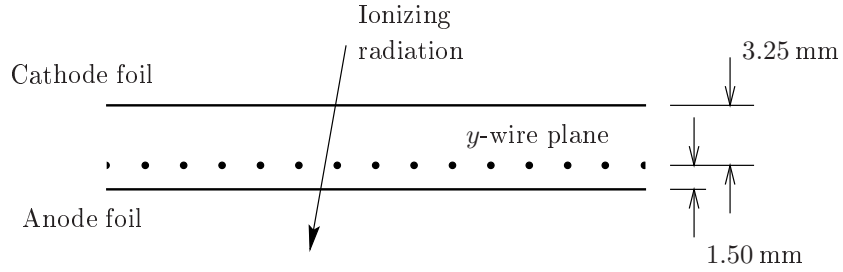
Figure 2.6: Cross-sectional diagram detailing the PPAC region of a PPAC-MWPC used in the ternary fission studies.

the signal originated. These two times are used to construct the time difference $dx = x_{\text{Left}} - x_{\text{Right}}$. Panel (a) of Fig. 2.7 is a plot of the time difference spectrum for the MWPC, demonstrating the single-wire resolution that can be obtained with this method. The time difference dx is used to determine the horizontal position of the incident particle within the active volume of the detector. The current design allows for position measurements in the x coordinate of the detector with a resolution of ~ 1.5 mm ($< 0.5°$ when the detector is positioned 30 cm from the target).

The parallel-plate avalanche counter region (PPAC) is similar to the MWPC region, consisting of a plane grid of 37 equally spaced copper-beryllium wires, referred to as the y-wire plane in Fig. 2.3, oriented orthogonal to the wires in the MWPC region. Each wire has a diameter of 50 μm with a spacing of 0.1 inches (2.54 mm) between adjacent wires. The y-wires are soldered onto a second PCB, separated from the first PCB by an 8.0 cm precision machined lexan spacer. The second PCB also contains the discrete components, including the LC delay chips and decoupling capacitors, of the read-out electronics for the PPAC region. As in the MWPC region, each wire is connected at one end to a tap on a delay line and the other end is left floating. Components of the delay line and position signal readout are the same as for the x-wire plane. As mentioned previously, the cathode foil separating the two detector regions also acts as the cathode for the PPAC region. A second, singly
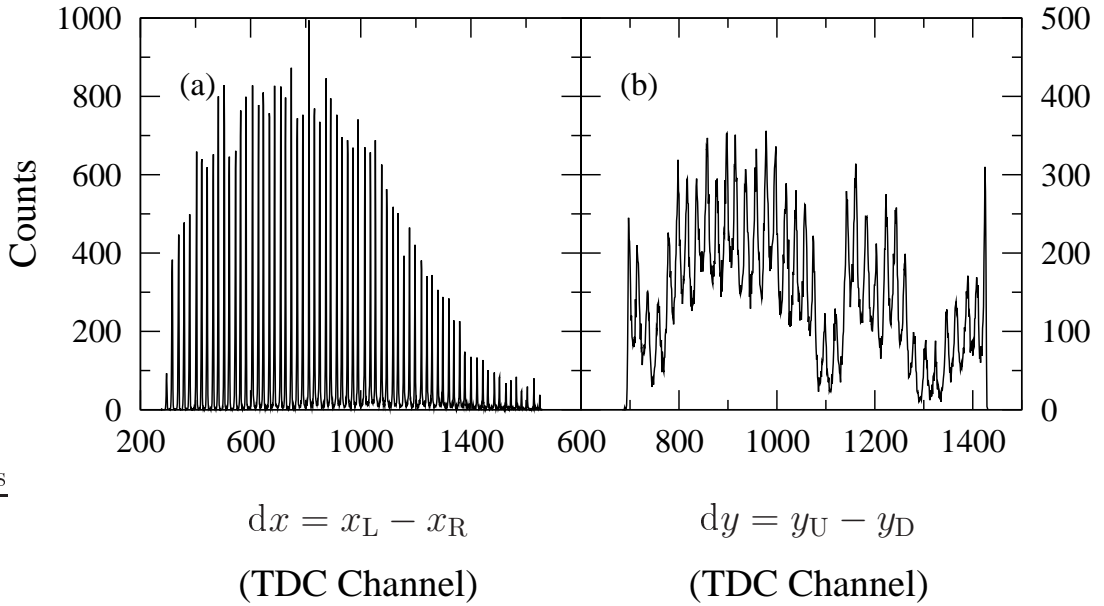
Figure 2.7: Spatial resolution of the PPAC-MWPC detectors. The data used are from the reaction ^{12}C $+^{232}$Th at 193 MeV/A. Panel a) is a plot of the constructed quantity $dx = x_{\text{Left}} - x_{\text{Right}}$ as described in the text. Panel b) is an analogous plot for the quantity $dy = y_{\text{Up}} - y_{\text{Down}}$.

aluminized mylar foil, opposite the y-wire plane, acts as the anode (see Fig. 2.6).

The general operating principles of the PPAC are also similar to the operating principles of the MWPC. Electrons created in the gas volume by ionizing radiation are accelerated in the electric field toward the anode foil where they are collected. As the electrons pass by the y-wires, they induce a current in the wires closest to the particle trajectory [8]. This induced current results in a positive pulse that is transmitted through the delay line, and is read out at either end. Very few of the electric field lines emanating from the cathode foil terminate at the position-sensing wires; most pass by the wires and terminate at the anode foil. Since, in this case, the electric field does not focus the moving cloud of electrons created by the ionizing particle, it tends to experience a greater degree of dispersion compared to the electron

cloud formed in the MWPC region.

Other than the process of inverting the signals with 100 MHz pulse transformers, the position wire signals for the PPAC region are treated identically to the x-wire signals of the MWPC region. The processed timing signals, y_{Up} and y_{Down}, are used to construct the time difference $dy = y_{\text{Up}} - y_{\text{Down}}$. As can be seen in panel (b) of Fig. 2.7, the y-wires do not provide the same level of resolution as the x-wires. We hypothesis that this reduced position resolution afforded by the y-wires is a consequence of the signal arising from an induced current on the wires as opposed to the direct collection of electrons, as is the case for the x-wire signals. Because of the azimuthal symmetry inherent in the reactions of interest, the resolution in the x direction is more imortant than the resolution in the y direction. Thus the inferior resolution of the y-wires did not have a significant impact on the quality of the physically extracted quantities.

The signal resulting from the electrons collected at the anode foil is read out through a decoupling capacitor. The signal is then amplified using a timing filter amplifier (TFA) with both a fast and a linear output. The fast signal from the TFA is passed through a constant fraction discriminator with four fast outputs. One output signal is used as a start (MSU experiment) or stop (ANL experiment) for a time-to-digital converter to be used in the time-of-flight analysis, while a second is used to increment the event scalers. The remaining two output signals are used to generate the event type selection trigger. The linear signal from the TFA is digitized with an analog-to-digital converter (ADC) for anode pulse-height analysis.

Figure 2.8 shows an example anode pulse-height spectrum. The large peak above $\Delta E \simeq 250$ channels is the result of fission fragments passing through the PPAC region of the detector. The narrower peak at low channel numbers is from α-particles. Since these experiments involved the use of targets composed of elements that are spontaneous α emitters, the detectors are subject to a steady flux of isotropically-emitted α particles in addition to those resulting from induced α radioactivity. The clean separation of the α's from the fission fragments in the anode pulse-height
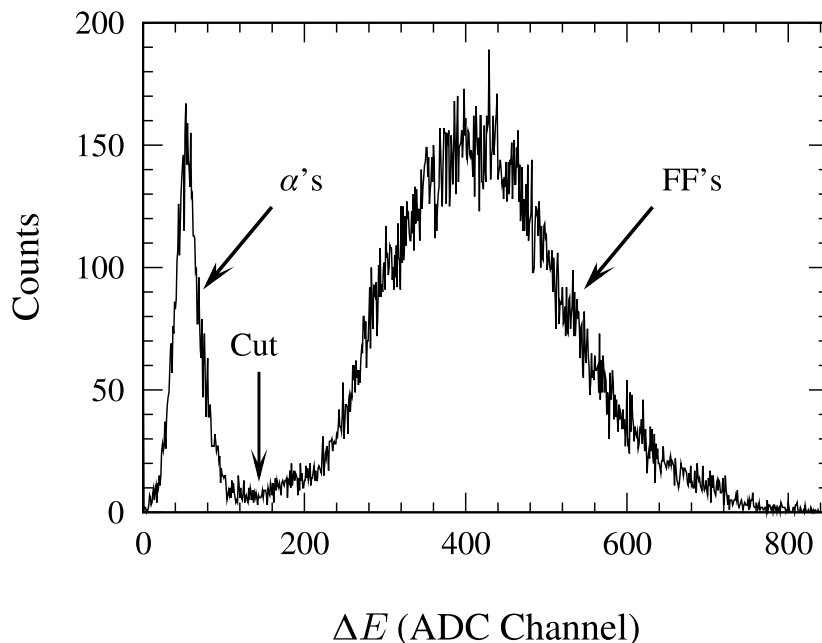
Figure 2.8: Example anode signal pulse-height distribution from the PPAC detectors. Data were obtained from the reaction ^{12}C $+^{232}$Th at 264 MeV/A. The arrow labeled "Cut" marks the ADC channel above which particles are identified as fission fragments (FFs). This allowed for rejection of events involving reaction and target decay α's detected in the PPACs.

distribution provides a simple means to reject non-fission events.

As mentioned earlier, the TDC information from the anode signal is used for fission fragment time-of-flight (TOF) analysis. This information, coupled with the kinematical relations developed in Sec. B.2 allowing a measure of the fragment masses. Panel (a) of Fig. 2.9 shows an example TOF spectrum for fission fragments detected in triple coincidence (ternary) events. The measured TOF was used to deduce the mass of the fission fragment as shown in panel (b) of Fig. 2.9.
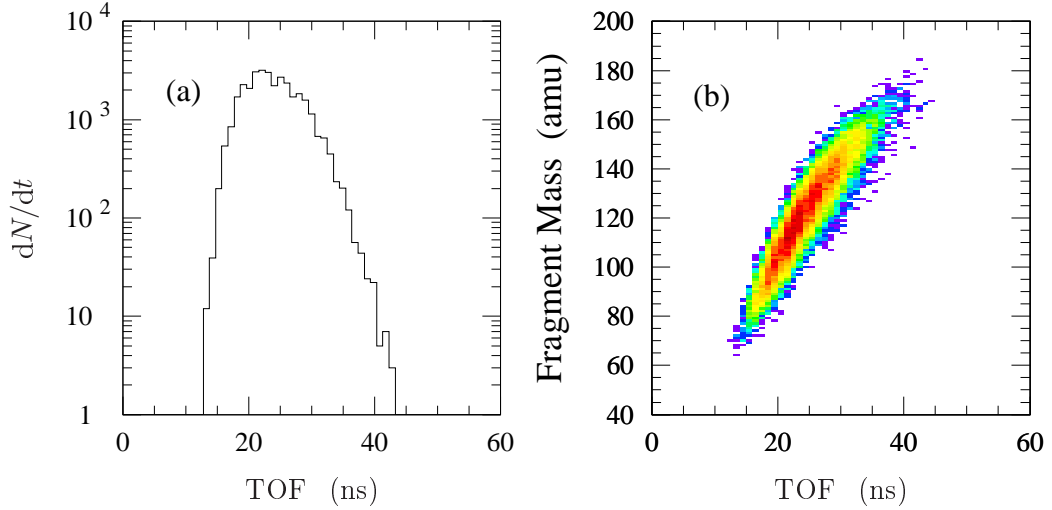
Figure 2.9: Example fission fragment time-of-flight (TOF) distribution: (a) TOF spectra for fission fragments detected in triple coincidence (ternary) events, (b) relation between fragment mass and the measured TOF from (a). Data are for the reaction ^{12}C + ^{232}Th at 16 MeV/A.

2.4   Ion Chamber Telescopes

A number of low threshold, large dynamic range ionization-chamber/Si(IP)/CsI(Tl) detector telescopes were used for IMF detection in the current work. These detector telescopes were designed, built and tested by the Nuclear Chemistry group at Indiana University [9]. The detector elements were housed inside trapezoidal steel cans with a front flange to attach the thin mylar entrance window (nominal thickness $\approx 0.176 \, \mathrm{mg/cm^2}$) and a rear flange that contained vacuum feed-throughs for detector bias, extracted signals and gas inlet and outlet.

The first active element of this telescope design is an axial-field, pulse-type gas-ionization chamber with an active path length of $\sim$ 6cm [10]. The electric field is shaped at the edges by seven 2 mm thick copper rings spaced 4 mm apart by nylon spacers. The anode is composed of a doubly aluminized mylar foil stretched across
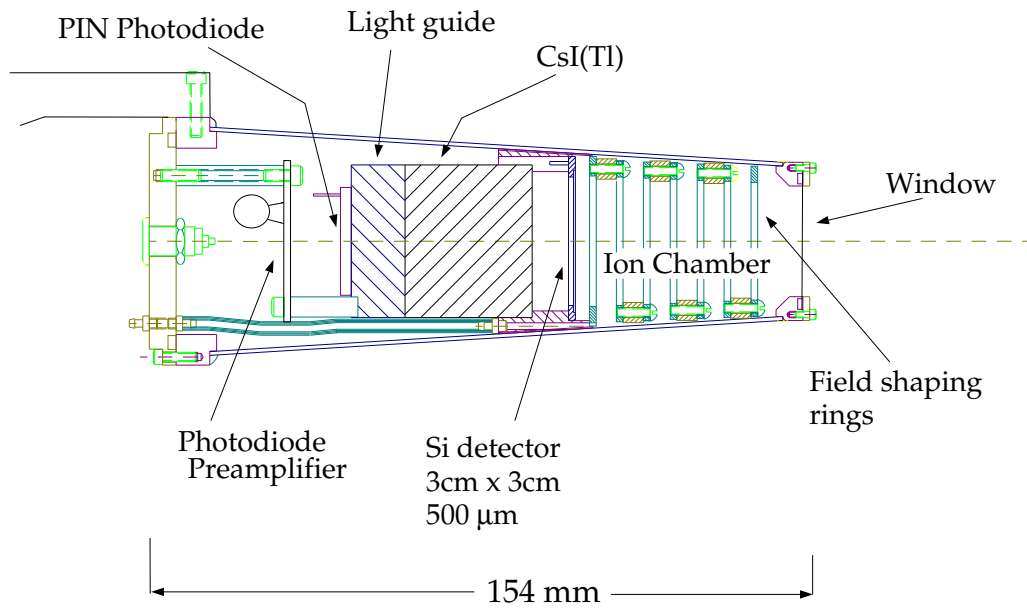
Figure 2.10: Schematic diagram of an ionization-chamber/Si(IP)/CsI(Tl) detector telescope.

the central field-shaping ring. This placement of the anode foil has the effect of minimizing the electron collection time by reducing the electron drift path length. Charged particles passing through the gas volume lose all or part of their energy in collisions with the gas molecules. A certain fraction of the energy lost to collisions results in ionization of the gas molecules into electron-ion pairs. The resulting free electrons are then accelerated under the influence of the applied electric field toward the anode foil where they are collected. Both sides of the anode foil are electrically shorted to the central ring, allowing collection of charge from the entire gas volume. Brass collimators were added at the front of the telescopes to suppress particles that might pass too close to the field-shaping rings, where fringe effects of the electric field were discovered to lead to non-linearities in the charge collection. The addition of the collimator resulted in an active area of $3.7\text{cm} \times 3.7\text{cm}$ at the front face of the telescope. The normal operating conditions for this detector is 18–20 Torr of CF_4
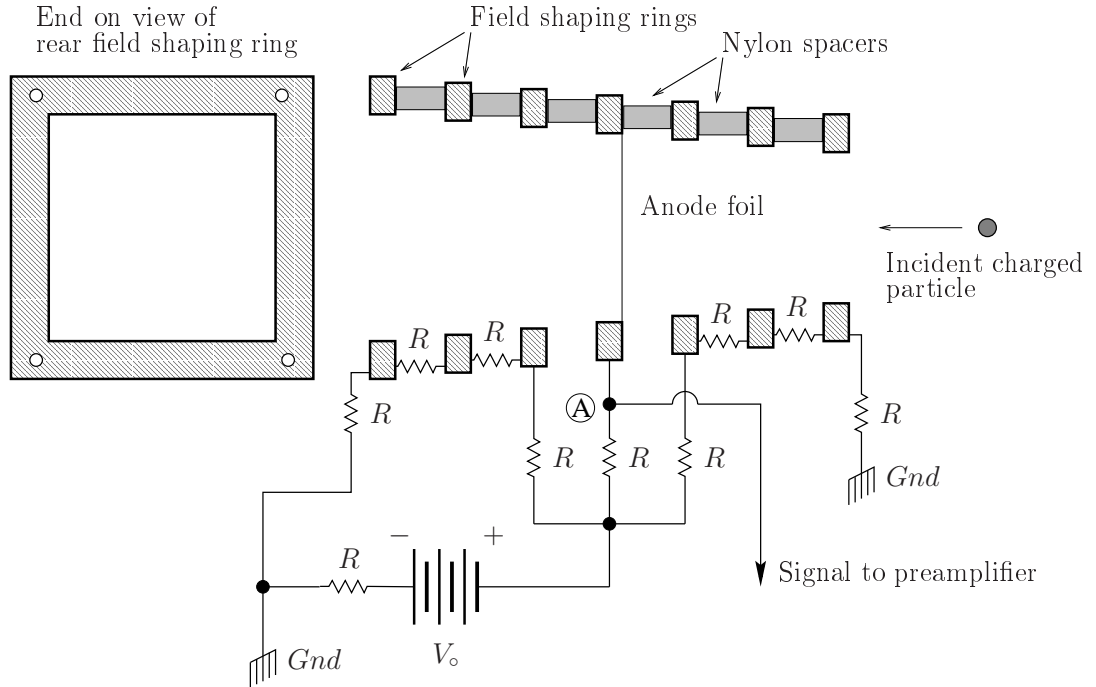
Figure 2.11: Schematic cross-sectional diagram of the ion-chamber region of an IC telescope. A schematic representation of the field-shaping electronics and signal read out is also shown at the bottom of the diagram.

and an anode voltage of $\sim$450 V.

A positive bias voltage is applied to the central field-shaping ring as shown in Fig. 2.11. A series of resistors that connect the rings is used create the potential gradient within the active volume of the detector. Charge collected at the anode foil causes a voltage drop at point A in Fig. 2.11. The signal produced by this voltage drop is processed by an external preamplifier located near the detector.

The second element of the telescope is an ion-implanted passivated Si detector (Micron Semiconductor model MSQ25-300) placed directly behind the ion chamber region. Each Si crystal measured 5cm$\times$5cm and was segmented into four quadrants. The nominal thickness of the crystals is 300 μm. Each quadrant is read out separately by a charge-coupled preamplifier. Due to our particular interest in low energy
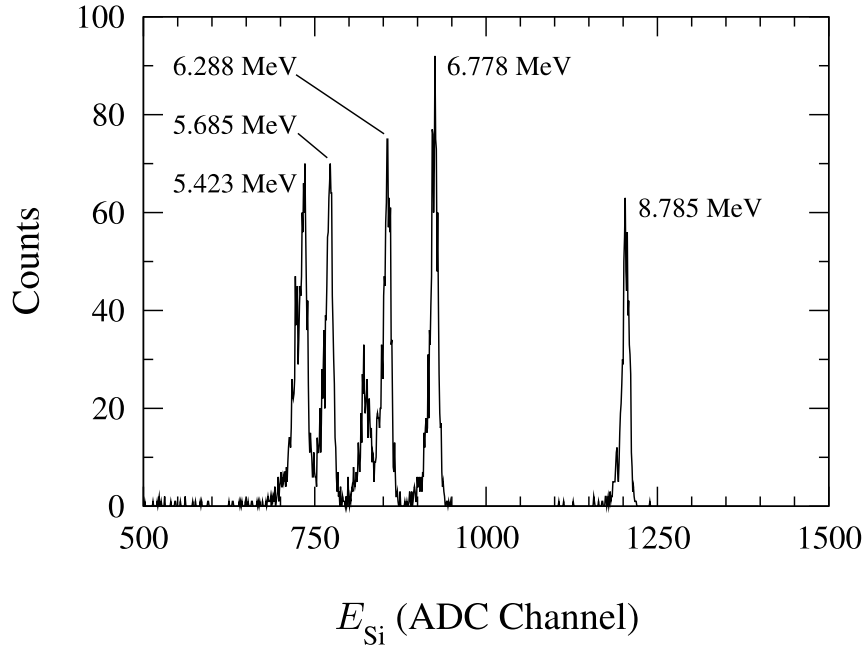
Figure 2.12: Example α-particle energy spectrum from one of the Si(IP) detectors used in the IC telescopes. The spectrum was acquired using a collimated ^{232}Th source positioned ~ 5cm from the front window of the telescope. The corresponding energies of the various α peaks are also shown.

particles, the front dead layer was carefully measured for each crystal to increase the accuracy of particle energy reconstruction. Fig. 2.12 shows a typical energy spectrum obtained during our calibrations using a ^{232}Th α source. The energy spectrum was acquired with no gas in the telescope, so the only additional factors to influence the energy resolution was introduced by the front window and the anode foil. In this example, the energy resolution was found to be $\sim 1.4\%$ or 95 keV for the 6.778 MeV α peak.

The final element of the telescope is a set of four thallium-doped cesium iodide scintillator crystals, CsI(Tl), one behind each quadrant of the silicon crystal. Each crystal measures $2.5\text{cm} \times 2.5\text{cm} \times 3.0\text{cm}$. Each CsI(Tl) crystal is wrapped around the sides with Teflon tape to improve diffuse reflectivity and to optically isolate adjacent

crystals to prevent cross-talk. The front face of each crystal is covered with 1.5 μm aluminized Mylar to reflect light back into the crystal. The rear face of each crystal is optically coupled to a 0.50 inch thick Plexiglas light guide which is in turn optically coupled to a 2cm $\times$ 2cm photodiode (Hamamatsu Photonics model S3204-03). The signal from each photodiode is processed by a charge-sensitive preamplifier, located in the rear of the steel can that houses the detector elements. As the preamplifier is within the gas volume, it is potted in silicon elastomer (Dow Corning Sylgard 184) in order to reduce the sensitivity of the field-effect-transistor to electrical discharges within the gas volume.

Two independent gas-handling systems were used to maintain a stable operating pressure for both the PPAC-MWPCs and the ionization chamber portion of the IC telescopes. The gas-handling systems were also designed to provide a steady flow of the filling gas through the detectors. This is necessary to prevent a build up of the slow moving positive ions, which would eventual begin to reduce the detector efficiency by recombining with the ionization electrons used to generate the detector signals.

References

[1] H. Fulbright, Nucl. Instrum. and Methods **162**, 21 (1979).

[2] F. Binon *et al.*, Nucl. Instrum. and Methods **94**, 27 (1971).

[3] J. van der Plicht and A. Gavron, Nucl. Instrum. and Methods **211**, 403 (1983).

[4] A. Breskin, Nucl. Instrum. and Methods **141**, 505 (1977).

[5] A. Breskin, Nucl. Instrum. and Methods **196**, 11 (1982).

[6] R. de Souza, Characterization of the Multifragmentation Decay Channel in Highly Excited Nuclei, Progress Report, 1993.

[7] G. Charpak and F. Sauli, Nucl. Instrum. and Methods **162**, 405 (1979).

[8] G. Charpak, G. Petersen, A. Policarpo, and F. Sauli, Nucl. Instrum. and Methods **148**, 471 (1978).

[9] D. Fox *et al.*, Nucl. Instrum. and Methods A **368**, 709 (1996).

[10] K. Kwiatkowski *et al.*, Nucl. Instrum. and Methods A **299**, 166 (1990).

Chapter 3

Experimental Setup and Detector Calibrations

The reaction ^{12}C + ^{232}Th was studied at incident energies of $E/A = 16$ and 22 MeV in order to probe the effects of excitation energy and angular momentum on the ternary fission process. Since the incident energy requirements could not both be achieved at a single accelerator laboratory, it was necessary to use both the Michigan State University Superconducting Cyclotron Facility (MSU: $E/A = 22$ MeV) and the ATLAS Accelerator Facility at Argonne National Laboratory (ANL: $E/A = 16$ MeV). Table 3.1 lists the maximum and observed excitation energies for the two experiments, along with data from an earlier ternary fission study [1].

3.1 Experimental Setup

The first experiment was conducted at the Michigan State University National Superconducting Cyclotron Facility (MSU-NSCL) using the 92" scattering chamber. The K1200 cyclotron was used to deliver a ^{12}C beam with an energy of $E/A = 22$ MeV ($E_{\mathrm{lab}} = 264$ MeV) and an average intensity of $\sim 10^{10}$ particles per second. The beam was directed at a self-supporting ^{232}Th target foil with an areal density of 700 μg/cm^2. The target foil was mounted on a metal frame with a 7/8" diameter

Reaction	^{12}C + ^{232}Th		^{4}He + ^{232}Th
Incident energy	22 MeV/A	16 MeV/A	50 MeV/A
$E^*_{\max}$ MeV/A (MeV)	0.91 (222.0)	0.64 (156.2)	0.77 (181.7)
$FLMT_{\mathrm{obs}}$	83%	100%	100%
E^*_{obs} MeV/A (MeV)	0.70 (169.4)	0.64 (156.2)	0.77 (181.7)

Table 3.1: $E^*_{\max}$ indicates the maximum initial excitation energy that could be achieved assuming complete fusion of projectile and target, calculated using the massive transfer model (see Appendix B for details of calculating the initial excitation energy). E^*_{obs} indicates the maximum excitation energy the could be obtained based on the maximum experimentally observed linear momentum transfer from the projectile to the composite nucleus, $FLMT_{\mathrm{obs}}$, for ternary events in which $Z_{\mathrm{IMF}} = 2$. For reference, the last column contains information about an earlier study of ternary fission which focused on the reaction ^{4}He + ^{232}Th at an incident energy of $E/A = 50$ MeV [1].

hole, that was rotated 45° with respect to the beam axis. A set of six large area, position-sensitive, hybrid parallel-plate avalanche counter/multi-wire proportional counters (PPACs) was used for detection of correlated fission fragments, three on either side of the beam axis (details of the operation of the PPACs are provided in Sec. 2.3). Light charged particles (LCP: $1 \leq Z_{\mathrm{LCP}} \leq 2$) and intermediate mass fragments (IMF: $3 \leq Z_{\mathrm{IMF}} \leq 13$), observed in coincidence with two correlated fission fragments, were measured at mid and backward angles relative to the beam axis by five low threshold ion chamber/Si(IP)/CsI(Tl) telescopes (details of the operation of the IC telescopes are provided in Sec. 2.4). A schematic diagram of the general layout for both experiments is given in Fig. 3.1.

The second experiment was performed at the ATLAS Accelerator Facility at Argonne National Laboratory. A ^{12}C beam was accelerated to an energy $E/A = 16$
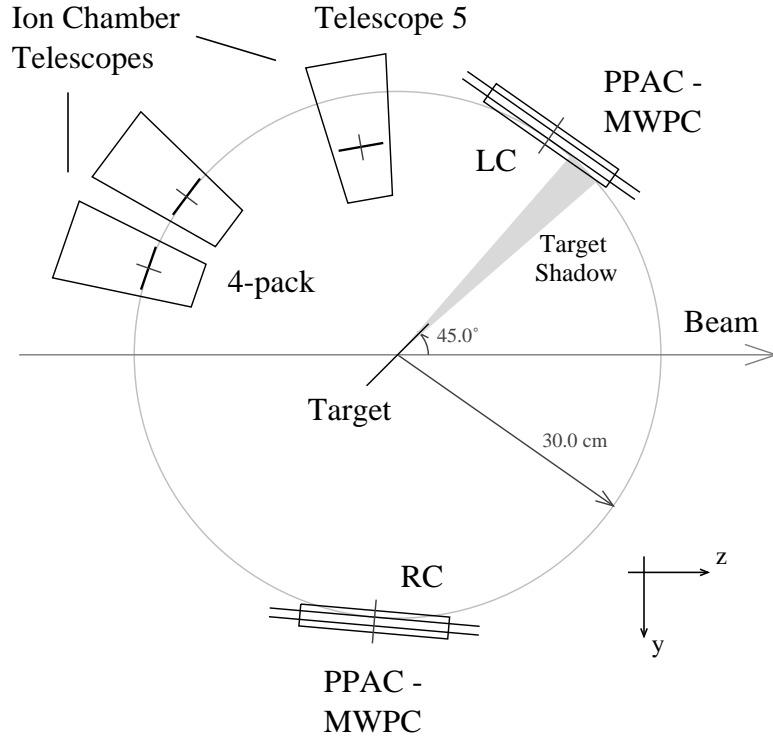
Figure 3.1: Schematic view of detector placement relative to the incident beam. Details of the detector designs can be found in Ch. 2. The out-of-plane PPACs have been left out for clarity.

MeV ($E_{\text{lab}} = 193$ MeV) by the ATLAS Tandem Linac Accelerator and directed on to a self-supporting ^{232}Th target foil with an areal density of 700 μg/cm^2. The target foil was mounted in a metal frame with the same characteristics as in the MSU-NSCL experiment. The average beam current was $\sim 4 \times 10^{10}$ particles per second. The target in this experiment was also rotated 45° with respect to the beam axis. The same detectors were used for identifying fission fragments, LCPs and IMFs. The PPACs were again grouped in pairs, one on either side of the beam axis with one pair centered in the (y, z)-plane, and a second pair rotated out of the (y, z)-plane by 27.5° (space limitations in the scattering chamber prevented using all three pairs).

At periodic intervals during both experiments the ^{232}Th target foil was replaced by an identical, empty target frame to assess the extent of beam scattering off the target frame. Negligible scattering from the target frame was observed.

As stated above, the target was rotated to 45° with respect to the beam axis in both experiments. This orientation was chosen for two reasons. First, to minimize the effects of target shadowing of the PPACs, illustrated as the gray wedge in Fig. 3.1. Second, to minimize the target foil thickness, as viewed in the direction of the IC telescopes, to limit the amount of energy lost by the IMFs while escaping from the target foil. This orientation of the target foil resulted in a loss of $\sim 25\%$ of the active area for the left side in-plane PPAC (LC in Fig. 3.1), and $\sim 30\%$ for the two left side out-of-plane PPACs due to target shadow.

3.1.1 Detection of Fission Fragments: PPACs

The PPACs were grouped in pairs, one on either side of the beam axis, as shown in Fig. 3.2, with one pair centered in the (y, z)-plane and one or two additional pairs rotated out of the (y, z)-plane by an angle $\varphi = \pm 27.5°$ directly above or below the center PPAC. The front window of each PPAC was positioned 30 cm from the target. The two in-plane PPACs, labeled LC and RC in Figs. 3.1 and 3.2, were centered at angles (ϑ, φ), as described in Table 3.2, to account for the reaction kinematics (see Appendix A for the details of converting the detector position angles (ϑ, φ) to polar spherical coordinate angles (θ, ϕ) in the laboratory system). Each PPAC had an active area of 8cm $\times$ 14cm, which provided an angular coverage of $\sim 32°$ in θ when positioned 30 cm from the target. The PPAC placement described in Table 3.2 allowed measurement of laboratory fission fragment folding angles, taking into account target shadow, over the range of $128° \leq \theta_{AB} \leq 178°$ in the MSU experiment and $128° \leq \theta_{AB} \leq 180°$ in the ANL experiment. The PPACs were operated in transmission mode, with a differential gas pressure of ~ 4 Torr of isobutane, as described in Sec. 2.3.
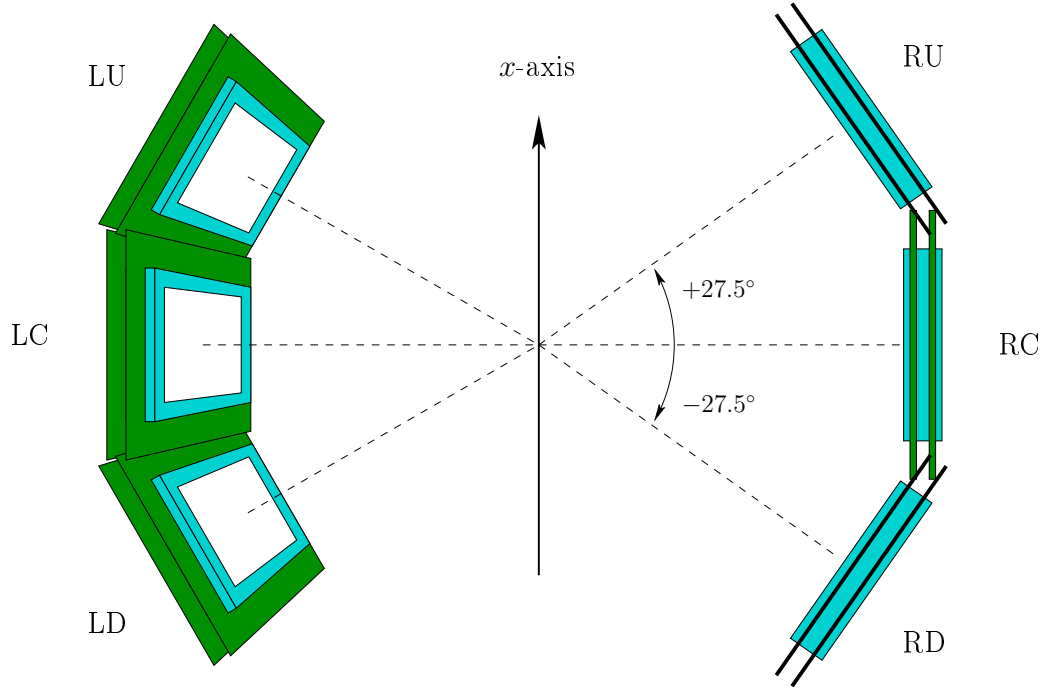
Figure 3.2: Schematic of the PPAC positions as viewed along the beam axis.

PPAC #		LC	RC	LU	RD	LD	RU
22 MeV/A	ϑ	$+51.3°$	$-95.2°$	$+51.3°$	$-95.2°$	$+51.2°$	$-95.2°$
	φ	$0.0°$	$0.0°$	$+27.5°$	$-27.5°$	$-27.5°$	$+27.5°$
16 MeV/A	ϑ	$+55.0°$	$-95.0°$	$+55.0°$	$-95.0°$	n/a	n/a
	φ	$0.0°$	$0.0°$	$+27.5°$	$-27.5°$	n/a	n/a

Table 3.2: Angular positions (ϑ,φ) of the PPACs during the two experiments. See Fig. 3.2 for definitions of the PPAC labels.

Telescope #		1	2	3	4	5
22 MeV/A	ϑ	$+167.6°$	$+167.6°$	$+149.9°$	$+149.9°$	$+100.6°$
	φ	$+8.8°$	$-8.8°$	$-8.8°$	$+8.8°$	$0.0°$
16 MeV/A	ϑ	$+160.8°$	$+160.8°$	$+143.2°$	$+143.2°$	$+100.0°$
	φ	$-8.8°$	$+8.8°$	$+8.8°$	$-8.8°$	$0.0°$

Table 3.3: Angular positions (ϑ,φ) of the IC telescopes during the two experiments. See Fig. 3.3 for definitions of the telescope labels.

3.1.2 Detection of Intermediate Mass Fragments: IC Telescopes

Four of the low threshold ion-chamber/Si(IP)/CsI(Tl) telescopes, referred to as the 4-pack in Figs. 3.1 and 3.3, were placed at backward angles in the laboratory and $\sim 90°$ with respect to the scission axis, as defined by the PPAC positions. Locating these detectors at backward angles effectively suppressed the detection of particles resulting from pre-equilibrium emission, as well as elastic and inelastic scattering of the projectiles. This suppression aided the detection of the low energy neck IMFs which were the principal interest in these experiments. These four telescopes were arranged in a box shape as depicted in Fig. 3.3. The fifth IC telescope was positioned at a smaller angle with respect to the scission axis ($\sim 50°$) to provide a measure of isotropically emitted charged particles. The angular positions of the IC telescopes in both experiments are listed in Table 3.3.

3.2 Detector Calibrations

The detectors were calibrated by utilizing both radioactive sources and precision pulse generators. Electronic pulsers were used to test linearity of the analog and digital electronics (pre-amplifier, shaper, digitizers, etc.) while the radioactive sources were used to provide an absolute reference. Calibrations were performed at the
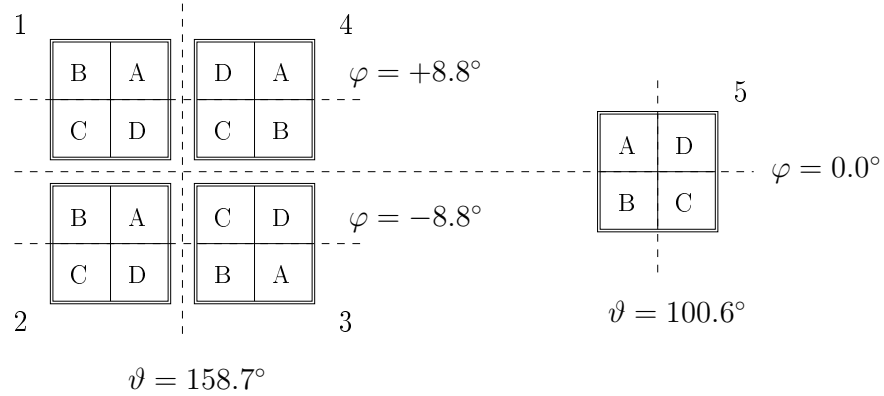
Figure 3.3: Schematic of the IC telescope positions as viewed from the target position. ϑ is the angle with respect to the beam axis in the forward direction. φ is a rotation out of the horizontal plane containing the beam axis (see Appendix A for a more detailed description). The individual telescopes are indicated by the numbers 1–5, and the quadrants within a telescope are indicated by the letters A–D. The block of four telescopes on the left side is collectively referred to as the 4-pack (see Fig. 3.1). The telescope number order and angular values given in the figure are for the MSU experiment.

end of each experiment, using the same detector and electronic configurations used during the experiments.

3.2.1 IC Telescope Energy Calibrations

The energy calibration of the IC telescopes was performed using a ^{228}Th α-source placed at the target position (see Fig. 3.1). The energies of the source α's were insufficient to pass through to the CsI(Tl) crystals, but since the CsI(Tl) signal was only used to reject high energy LCPs and not to determine particle energies, there was no need for a calibration. The target ladder was rotated to illuminate each telescope in turn, and three spectra were recorded for each telescope: one with no filling gas in the telescopes, a second with the filling gas at the same pressure as was

used during the experiment, and a third with twice the gas pressure used during the experiment. The first set of spectra, acquired with no filling gas in the telescopes, was used as an absolute calibration for the energy deposited in the Si(IP) detector element. A typical spectrum for one quadrant of a Si(IP) detector is shown in panel (a) of Fig. 3.4. Although an independent energy calibration based on the source α's was performed for the ionization-chamber data, its only purpose was to be able to sum spectra over several telescopes (specifically the ΔE-E spectra discussed in Sec. 3.2.3).

Each quadrant of a segmented silicon detector was calibrated separately by fitting each peak in the α spectra with a Gaussian and extracting the centroid. The resulting centroids, in ADC channel number, were then plotted against the corresponding, well known α-particle energies for the ^{228}Th decay chain (displayed in Fig. 3.5), after correcting for all "dead layers". The "dead layers" included all intervening material, between the source of the radiation and the active detector element, that degrades the energy of incident radiation but does not contribute to the detector signal extracted from that element. For determination of the energies of the α-particles entering the signal generating region of the Si(IP) detector elements, the dead layers considered were the mylar window and anode foils, the gas of the ionization chamber (if present) and the aluminum layer on the surface of the Si crystal. The α calibration of the Si(IP) detector element was performed using the energy spectrum acquired with no filling gas. This choice was made to avoid uncertainties associated with the dead layer correction for the filling gas (variation of gas pressure with temperature and variation of path length through the gas introduced by bowing of the mylar window). The source α-particle data were fit with a linear function as shown in panel (b) of Fig. 3.4. This linear fit was used as an initial calibration curve to relate ADC channel number to energy, in MeV, deposited in the Si(IP) detector, E_{Si}.

The linearity of the Si(IP) detectors and the associated electronics was checked over the full dynamic range of the ADCs by injecting precise amounts of charge from a research pulser coupled to a charge terminator into the input of the charge-

Chapter 3: Experimental Setup and Detector Calibrations   52
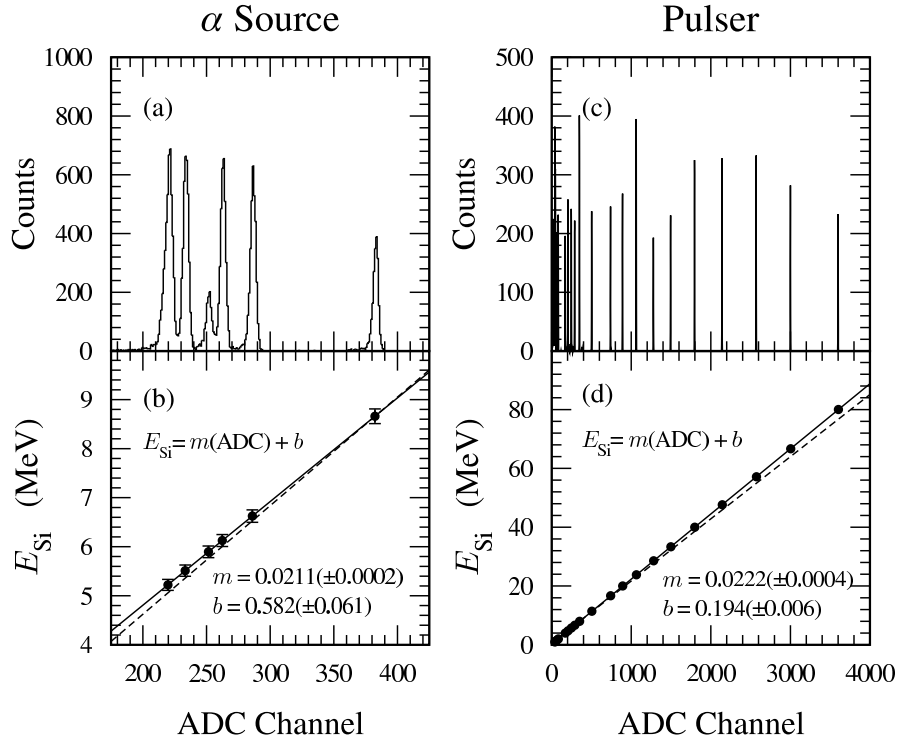
Figure 3.4: Si(IP) detector energy calibration for one Si quadrant. Panel (a) shows the uncalibrated energy spectrum, in ADC channels, obtained from a ^{228}Th α-source. The spectrum was acquired with no filling gas in the IC telescope. Panel (b) shows the relationship between ADC channel number and energy deposited in the Si(IP) detector (after accounting for intervening dead layers: window foil, anode foil, etc.) for the α-source calibration. The solid line is the result of a linear fit to the α calibration points. The dashed line is the calibration curve from the pulser data. Panel (c) shows the uncalibrated spectrum obtained by injecting precise amounts of charge from an Ortec model 448 research pulser through a charge terminator and into the preamplifier input. The picket-fence spectrum was generated by varying the attenuation setting for the pulser signal output. Panel (d) shows the energy calibration based on the data from the precision pulser. The solid line is the pulser energy calibration curve. The dashed line is the α energy calibration curve.
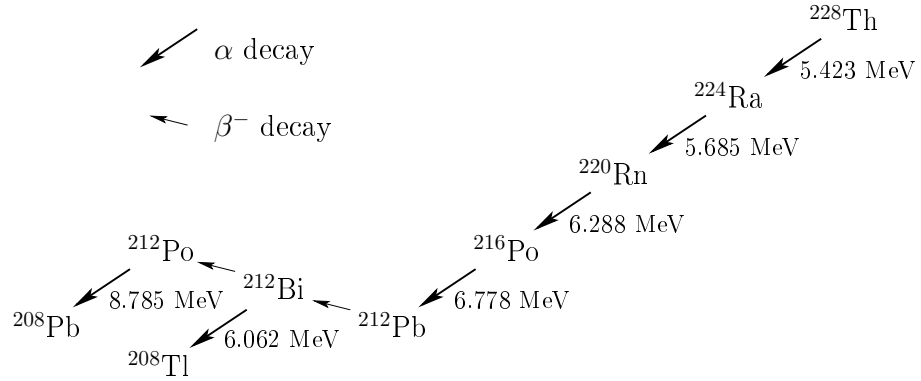
Figure 3.5: ^{228}Th decay chain used in the IC telescope energy calibrations. The average energy for each decay α is listed next to the α decay arrows.

sensitive pre-amplifier of each Si(IP) quadrant. While performing this calibration, the Si(IP) detectors, connected to the pre-amplifiers, were biased to their operating voltage to maintain the same detector capacitance as during the experiment. For the 193 MeV ^{12}C + ^{232}Th reaction, an Ortec model 448 research pulser was used, and for the 264 MeV ^{12}C + ^{232}Th reaction, a BNC model PB-4 pulser was used. The pulser was initially set, with no attenuation, so as to simulate the largest pulses observable within the dynamic range ADCs. The amount of injected charge was then reduced by known amounts, using the precision attenuation switches on the pulser. A "picket-fence" spectrum, shown in panel (c) of Fig. 3.4, was generated in this manner for each Si(IP) quadrant.

In the pulser spectrum the ith peak is associated with a specific pulser attenuation setting, f_i, with the first peak (lowest channel number) having the highest attenuation factor. However, it is more convenient to associate each peak with the relative attenuation, f_1/f_i, where f_1 is the attenuation factor for the first peak. Thus the extracted centroids, x_i, were associated with the corresponding relative attenuation, and the resulting data were fit with a linear function. The fit provided a

calibration curve of the form

$$\frac{f_1}{f_i} = mx_i + b \tag{3.1}$$

where m is the slope and b the intercept. At this point, the pulser calibration expresses a relation between ADC channel number and relative attenuation factor. To convert this expression to a calibration for the energy deposited in the Si(IP) detector, E_{Si}, we introduce the quantity E_0/f_1, where E_0 is the equivalent Si(IP) energy in MeV for no attenuation of the pulser signal, and f_1 is the maximum attenuation factor used in the calibrations. The quantity E_0/f_1 is thus the energy per unit of attenuation over the full range of the pulser calibration. Multiplying both sides of Eq. 3.1 by E_0/f_1 gives

$$\frac{E_0}{f_1} \cdot \frac{f_1}{f_i} = \frac{E_0}{f_1} \cdot mx_i + \frac{E_0}{f_1} \cdot b,$$

which reduces to

$$\frac{E_0}{f_i} = E_i = \left(\frac{mE_0}{f_1}\right) x_i + \left(\frac{bE_0}{f_1}\right), \tag{3.2}$$

where E_i is the energy of the ith pulser calibration point in MeV. Equation 3.2 provides the desired linear relation between ADC channel number and energy deposited in the Si(IP) detector element, in which the slope, m', and intercept, b', are given by

$$m' = \frac{mE_0}{f_1} \qquad \text{and} \qquad b' = \frac{bE_0}{f_1},$$

where m and b are the slope and intercept from Eq. 3.1.

The unknown quantity E_0 was determined by inserting the centroid channel number and deposited energy for one of the α calibration points, x_α and E_α, into Eq. 3.2 and solving for E_0. This calculation was performed for each of the α calibration points, but the best agreement between the α calibration curve and the resulting pulser calibration curve was obtained when using the values for the 8.785 MeV α. Inserting the degraded energy and centroid channel for this α point, and the relative attenuation fit parameters extracted from the pulser spectrum in panel (c) of Fig. 3.4, we get

$$E_0 \quad = \quad E_\alpha \left(\frac{m}{f_1} x_\alpha + \frac{b}{f_1}\right)^{-1}$$

$$= (8.660 \text{ MeV}) \left(\frac{0.02325}{84} (382.3) + \frac{0.20350}{84} \right)^{-1} = 80.009 \text{ MeV}.$$

The slope and intercept for the pulser energy calibration curve are then calculated to be

$$m' = \frac{(0.02325)(80.009 \text{ MeV})}{84} = 0.0222 \text{ MeV/ADC channel}$$

$$b' = \frac{(0.20350)(80.009 \text{ MeV})}{84} = 0.194 \text{ MeV}$$

as shown in panel (d) of Fig. 3.4.

The quality of the two energy calibration curves was examined by plotting the percent difference between each calibration curve and the corresponding calibration points. Panel (a) of Fig. 3.6 shows the percent difference for the α energy calibration. The maximum deviation, of only 0.2%, occurs for the lowest energy point. Panel (b) of Fig. 3.6 is a plot of the percent difference for the pulser energy calibration. The deviation is consistently small at high Si(IP) energies, $< 1\%$, indicating negligible non-linearities over this portion of the dynamic range. However, focusing on the low energy region in panel (c) shows that, although the pulser calibration curve deviates little from the pulser calibration points even over the range covered by the α calibration, it diverges rapidly below a Si(IP) energy of ~ 2–3 MeV. This range in E_{Si} corresponds to a range in the total IMF energy of ~ 4–5 MeV for $Z = 3$ and ~ 9–10 MeV for $Z = 6$. The observed deviations indicate that the detector response becomes non-linear at low energies. This was not a concern, however, since this energy range is at or below the detection threshold for all light fragments investigated (detection threshold is ~ 0.8 MeV/A). Finally, panel (d) shows the percent difference between the pulser and α calibration curves.

3.2.2 Determination of IMF Energies

From the measured energy, E_{Si}, deposited in the Si(IP) detector element, the total energy of a particle can be deduced by calculating the energy loss incurred by its passage through the gas in the ionization chamber and the intervening dead layers.
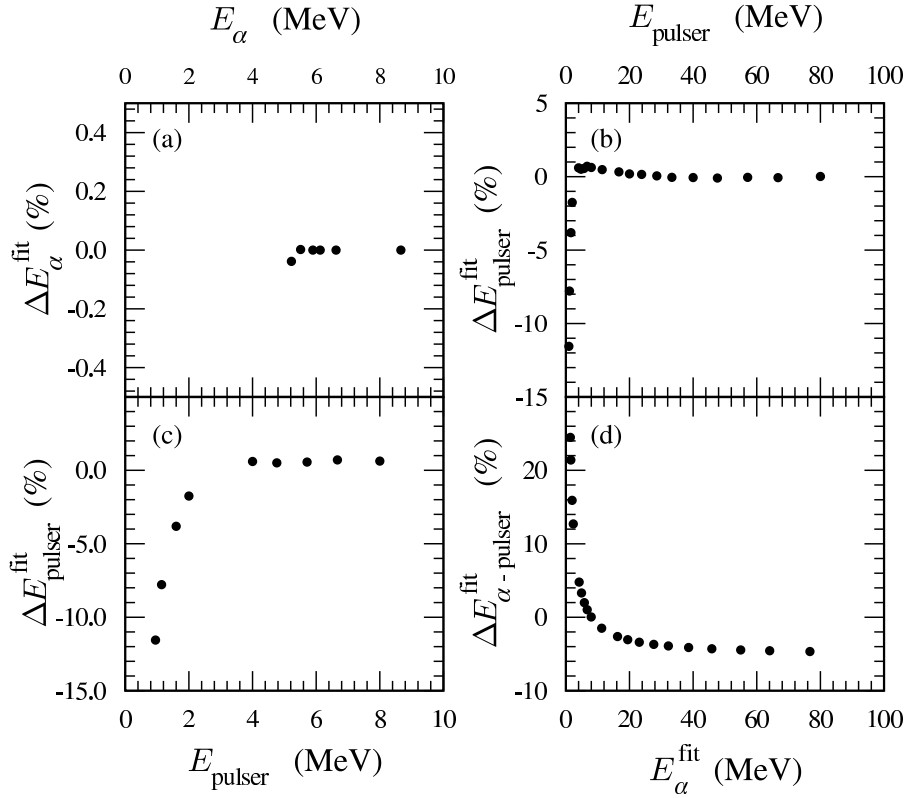
Figure 3.6: Comparison of α and pulser energy calibrations for one Si quadrant. Panel (a) shows the variation between the α calibration points and the energy calculated from the linear calibration curve. The variation is plotted as the percent difference $\Delta E_{\alpha}^{\text{fit}} = (E_{\alpha} - E_{\alpha}^{\text{fit}})/E_{\alpha}$ as a function of E_{α}, where E_{α} is the source α energy and E_{α}^{fit} is the corresponding energy calculated from the α calibration curve. Panel (b) shows the same for the pulser calibration points, i.e. $\Delta E_{\text{pulser}}^{\text{fit}} = (E_{\text{pulser}} - E_{\text{pulser}}^{\text{fit}})/E_{\text{pulser}}$ as a function of E_{pulser}. Panel (c) is an expanded view of the low energy portion of the variation of the pulser calibration in panel (b). The energy range corresponds to that used in panel (a). Panel (d) shows the variation between the α and pulser calibration curves, $\Delta E_{\alpha-\text{pulser}}^{\text{fit}} = (E_{\alpha}^{\text{fit}} - E_{\text{pulser}}^{\text{fit}})/E_{\alpha}^{\text{fit}}$ as a function of E_{α}^{fit}.

Z_{IMF}	2	3	4	5	6	7	8	9	10	11	12	13
A_{IMF}		4	7	10	11	14	16	18	20	22	24	26	29

Table 3.4: IMF mass, A_{IMF}, as a function of the atomic number, Z_{IMF}, used to deduce total particle energies.

The energy loss, $\mathrm{d}E$, incurred by a particle of incident energy E_i, atomic number Z and mass number A, in traversing an infinitesimal amount of matter, $\mathrm{d}x$, is given by the Bethe-Bloch formula [2, 3, 4]:

$$\frac{\mathrm{d}E}{\mathrm{d}x} = \left(\frac{e^2}{4\pi\epsilon_0}\right)^2 \frac{4\pi Z_i^2 N_0 Z \rho}{mc^2 \beta^2 A}\left[\ln\left(\frac{2mc^2\beta^2}{I}\right) - \ln\left(1-\beta^2\right) - \beta^2\right] \qquad (3.3)$$

where $v = \beta c$ is the velocity of the incident particle, Z_i is its atomic number, Z, A, and ρ are the atomic number, atomic weight, and density of the material through which the particle is moving. Total particle energies were obtained from lookup tables generated using the FORTRAN energy loss code published by Ziegler *et.al.* [5], which utilizes Eq. 3.3. These lookup tables expressed the total particle energy, E_{total}, as a function of the mass number, A, and atomic number, Z, of the particle, and the energy deposited in the Si(IP), E_{Si}. Since the IC telescopes did not provide mass resolution, a most probable mass had to be assumed for each element. Table 3.4 lists the mass numbers used in the energy loss calculations as a function of the atomic number of the incident particle. These values were chosen based on results from earlier investigations of spontaneous, thermal-neutron induced, and light-ion induced ternary fission [6, 1].

The energy-loss calculations took into account all known active and dead layers in the telescopes, including the mylar window and anode foils, pressure of the filling gas, and the silicon oxide dead layer. To minimize digitization effects, a granularity of 100 keV in Si(IP) energy was used in constructing the lookup tables. As mentioned previously, the calculated energy loss in the ionization chamber was subject to uncertainties associated with the variation of gas pressure with temperature as

well as variations in path length through the gas caused by bowing of the entrance window. The uncertainties in the energy deposited in the gas lead to an uncertainty of $\sim$1–3% in the deduced particle energy, depending on the mass of the incident particle.

3.2.3 Particle Identification

Particle identification was performed using the ΔE-E technique. This technique relies upon the stopping power of ionizing radiation in matter. The Bethe equation, Eq. 3.3, may be approximated for non-relativistic particles by the expression

$$\Delta E = \frac{kZ^2 A}{E} = f(Z, A, E) \tag{3.4}$$

where Z is the charge of the incident particle, A is its mass number, and k is a constant that depends on the stopping material. One can utilize this energy-loss relation to identify particles by allowing them to penetrate a stack composed of at least two detector elements. The first element operates in transmission mode, that is, the incident particle with initial energy E is not stopped within the detector medium but passes completely through it. Since the incident particle is not stopped, it deposits only a portion of its initial energy, ΔE, within the detector, and exits the back of the detector with a reduced energy $E' = E - \Delta E$. The remaining energy of the incident particle, E', is then deposited in the second detector element, which must be thick enough to stop the particle. Thus, for particles that are stopped in the second detector element, Eq. 3.4 indicates that a plot of ΔE *vs.* E would result in a set of hyperbole, each corresponding to a different value of $Z^2 A$. If ΔE is small compared to E, it is also possible to achieve the same result by plotting ΔE *vs.* E', since now E' is approximately equal to E.

Two dimensional (2D) histograms of ion-chamber energy, ΔE_{IC} (ΔE), *vs.* Si(IP) energy, E_{Si} (E'), were generated for each IC telescope. Panel (a) of Fig. 3.7 is an example of the 2-D spectrum for Si singles events (only one Si quadrant recorded a particle with nothing in any of the PPACs). In this spectrum particle identification
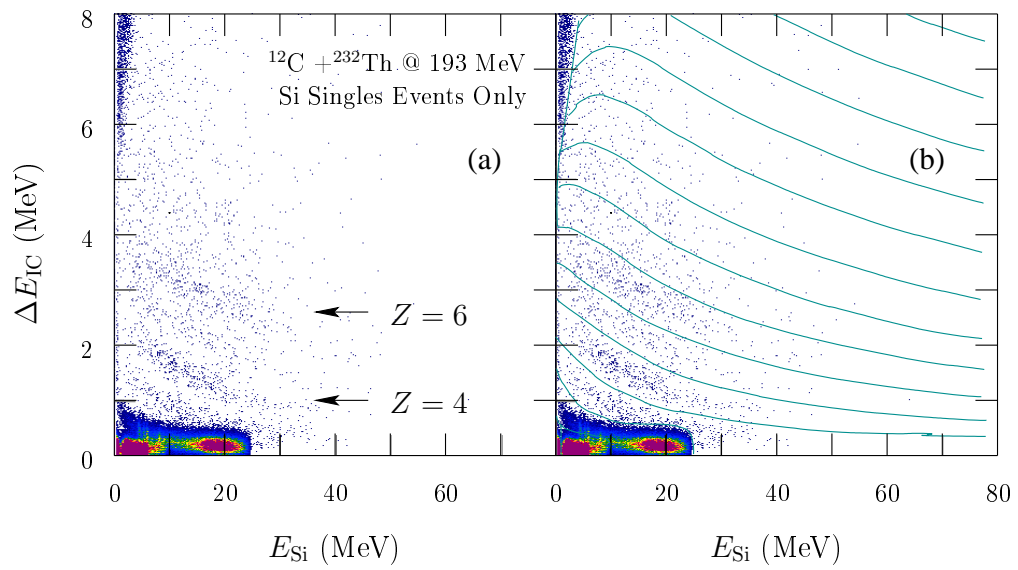
Figure 3.7: ΔE_{IC}–E_{Si} map used for particle identification in the IC telescopes. Panels (a) and (b) show the same 2D spectrum, panel (b) includes the particle identification gates used in the analysis.

was possible by visual inspection for $2 \leq Z \leq 6$. Particle Z identification was achieved over this range by hand-drawn selection gates as shown in panel (b) of Fig. 3.7. For $Z \geq 7$ the experimental statistics were insufficient to allow for reliable hand-drawn gates. Particle-identification gates for higher values of Z were calculated using the Ziegler energy loss code [5] described previously. Particle-identification gates were also calculated for $2 \leq Z \leq 6$, for comparison with the hand drawn gates. The differences between the hand-drawn and calculated particle-identification gates for $2 \leq Z \leq 6$ were found to be negligible except for the low edge of the $Z = 2$ gate (the line separating $Z = 1$ and $Z = 2$ in panel (b)). This agreement provided a high level of confidence in the accuracy of the calculated particle-identification gates for higher Z.

3.2.4   PPAC Position Calibrations

The position signal provided by the PPAC detectors was calibrated by exposing them to a ^{252}Cf fission source mounted at the target position. The source was rotated to illuminate each set of PPACs on either side of the beam axis. The PPACs were exposed to the source for a sufficiently long time so that all of the position sensing wires were visible, as can be seen in Fig. 3.8. In this plot, each peak corresponds to one of the position sensing wires. While the discrete wire resolution provides an excellent relative reference frame, it is necessary to ensure the absolute position of each PPAC by determining the absolute position of at least one wire. To provide such absolute position information, a second calibration run was performed with the ^{252}Cf source, this time with an aluminum mask placed over the PPAC face. The mask was sufficiently thick to stop all fission fragments as well as the ^{252}Cf decay α's. Each mask was pierced in the center with a cross pattern that left the center wires in both the x and y planes exposed. Examples of the mask spectra are shown in panels (c) and (d) of Fig. 3.8, along with a schematic of the masks used to create them. Transiting of the detector positions at the end of the experiment provided the absolute position of the two center wires.
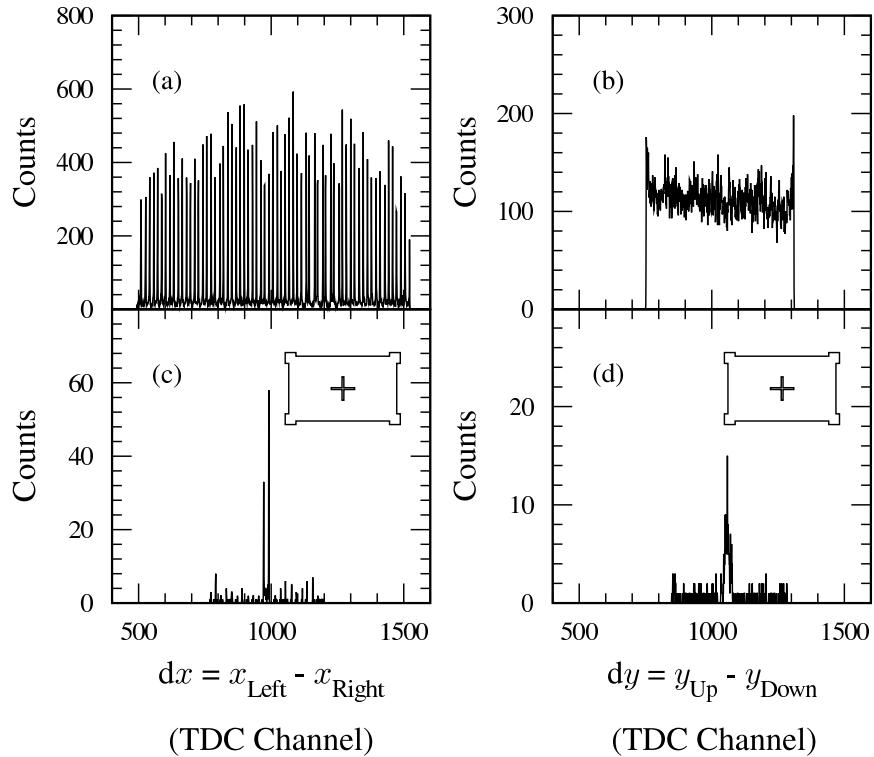
Figure 3.8: TDC time difference spectra, dx and dy, used for position calibrations of one in-plane PPAC. A ^{252}Cf fission source was used to illuminate each of the PPAC detectors. Panel (a) is the position spectrum of the x coordinate, d$x = x_{\text{Left}} - x_{\text{Right}}$. Panel (b) is the position spectrum of the y coordinate, d$y = y_{\text{Up}} - y_{\text{Down}}$. Panel (c) is the position spectrum of the x coordinate when the mask has been placed over the front face of the PPAC. Panel (d) is the position spectrum of the y coordinate with the mask. A schematic of the mask is included in panels (c) and (d).
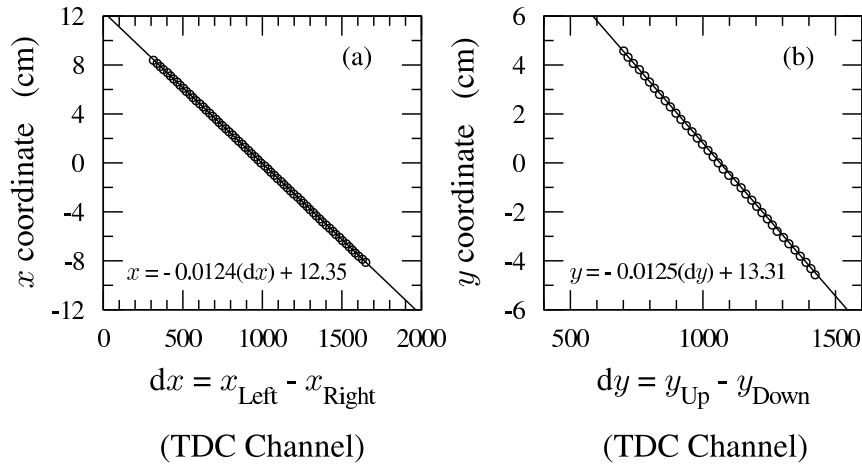
Figure 3.9: Relation between the absolute wire positions in the detector coordinate system, in cm, and the peaks of the time difference spectra. Panel (a) shows the relation for the x-wire plane, and panel (b) shows the same for the y-wire plane.

Once the absolute position of the center wires was established, a relation was made between the peaks in the time difference spectra, panels (a) and (b) of Fig. 3.8, and the position in cm of each wire relative to the center wires, based on the known wire spacing of the detectors. The centroids of the peaks in the time-difference spectra were extracted and plotted against the position of the corresponding wires. The center wire was always assigned the position value of 0.0 cm in the detector coordinate system. Figure 3.9 is a plot of the position, in cm, in the detector coordinate system *vs.* the centroids extracted from the time difference spectra for one PPAC. Panel (a) is for the PPAC x coordinate, and panel (b) is for the PPAC y coordinate. Calibration curves for both planes in each PPAC were generated by applying a linear fit to these points. Finally, an Euler transformation was used, on an event-by-event basis, to convert the absolute position in the detector coordinate system to an absolute position in the laboratory coordinate system.

3.2.5   PPAC Time Calibrations

The TDCs used with the PPACs were calibrated in time by using a Ortec 462 Time Calibrator. The Time Calibrator was set to generate signals that differed in time by 8 ns. The resulting spectra were a "picket fence" in TDC channels for which the peak-to-peak time was 8 ns. Panels (a) and (b) of Fig. 3.10 are plots of the picket fence spectra for the anode (time-of-flight) and accelerator RF TDCs respectively for one PPAC. A linear fit was then applied to a plot of TDC time in ns *vs.* the extracted centroids from the picket fence spectra for each TDC signal. Panels (c) and (d) of Fig. 3.10 show the plots and fits used to generate the calibration curves for the spectra shown in panels (a) and (b) respectively.
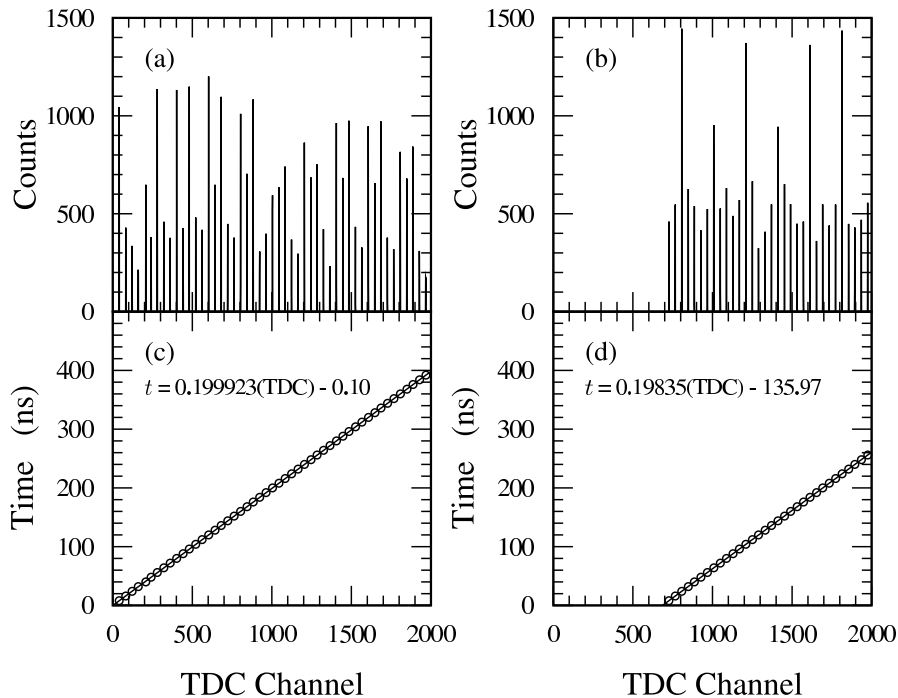
Figure 3.10: TDC time calibrations for anode (time-of-flight) and accelerator RF for one of the in-plane PPACs. Panels (a) and (b) are the recorded spectra from the Time Calibrator for the anode and RF TDCs respectively for one PPAC. The distance between adjacent peaks is 8 ns. Panels (c) and (d) are the points (time,channel) and corresponding fits for the spectra in panels (a) and (b) respectively.

References

[1] S. Chen *et al.*, Phys. Rev. C **54**, 2114 (1996).

[2] H. Bethe, Ann. Physik **5**, 325 (1930).

[3] F. Bloch, Ann. Physik **16**, 285 (1933).

[4] H. B. J. Ashkin, (1953).

[5] J. Ziegler, J. Biersack, and U. Littmark, *The Stopping and Range of Ions in Solids* (Pergamon Press, New York, 1985).

[6] G. Mütter and D. Poenaru, in *Nuclear Decay Modes*, edited by D. Poenaru (Institute of Physics Pub., Philadelphia, 1996), Chap. Particle-accompanied Fission.

Chapter 4

Experimental Results

In order to examine the general characteristics of ternary fission in comparison to binary fission, as well as the characteristics specific to ternary fission, we present the in-plane and out-of-plane angular correlations between coincident fission fragments. For ternary fission the dependence of the in-plane angular correlation, and thus the deduced linear momentum transfer, on Z_{IMF} of the ternary fragment can provide information on possible entrance channel effects (central *vs.* peripheral collisions). Examination of the Z_{IMF} dependence of the fractional linear momentum transfer (*FLMT*) will then be used to investigate the possible influence of angular momentum on the three body breakup of the composite system. Next, the energy spectra for ternary fragments will be discussed, including the energy cuts used to separate fragments emitted isotropically and near-scission. The Z dependence of the center-of-mass energy of ternary fragments will also be considered. The yields of ternary fragments emitted isotropically and near-scission are then examined and compared to previous data for both statistical (isotropic) and near-scission emission. Particular insight is provided by examining the dependence of relative yields of ternary fragments (both isotropic and near-scission) on the deduced excitation of the composite system. Finally, the absolute cross-sections for ternary fragments emitted near-scission will be presented.

To facilitate understanding of the scattering process, the azimuthal symmetry of

the scattering with respect to the beam direction was utilized. Detector placement was defined in terms of a Cartesian coordinate system in which the z-axis was oriented along the beam direction, and the horizontal or (y, z)-plane was defined by the beam and the centers of the two "in-plane" PPACs as shown in Fig. 3.1 in Chapter 3. The origin was defined by the intersection of the beam and the target foil. Angular quantities were calculated in terms of a spherical coordinate system corresponding to the chosen Cartesian coordinate system. Unless specifically stated otherwise, all data have been corrected for geometric efficiency of the detectors. Details of the geometric efficiency corrections are described in Appendix C.

4.1 Fission Fragment Angular Correlations

The azimuthal (out-of-plane) angular correlation distributions for coincident fission fragments is shown in Fig. 4.1. The data plotted in panel (a) are for the case of binary fission at the two incident energies, while the data in panel (b) are for the case of ternary fission including both the isotropic and near-scission components. The data for ternary fission are summed over $3 \leq Z_{IMF} \leq 13$ of the ternary fragment for the 22 MeV/A data and $3 \leq Z_{IMF} \leq 12$ for the 16 MeV/A data. The ternary cases include both isotropic and near-scission emission. In both cases, the azimuthal correlation angle is defined as the difference between the azimuthal coordinates of the two coincident fission fragments, i.e. $\phi_{AB} = |\phi_A - \phi_B|$. For the case of binary fission, conservation of linear momentum requires that the angle ϕ_{AB} be 180° in the center-of-mass of the fissioning nucleus. Because this angle is measured perpendicular to the direction of motion of the composite system, it is invariant under a transformation to the laboratory reference frame. Therefore, it is expected that the average azimuthal correlation angle, as measured in the laboratory, be 180° for binary events. Table 4.1 lists the mean values, $\langle \phi_{AB} \rangle$, and second moments, $\mu_2 = \sigma^2$, obtained by fitting a Gaussian to each of the distributions in Fig. 4.1. Second moments were corrected
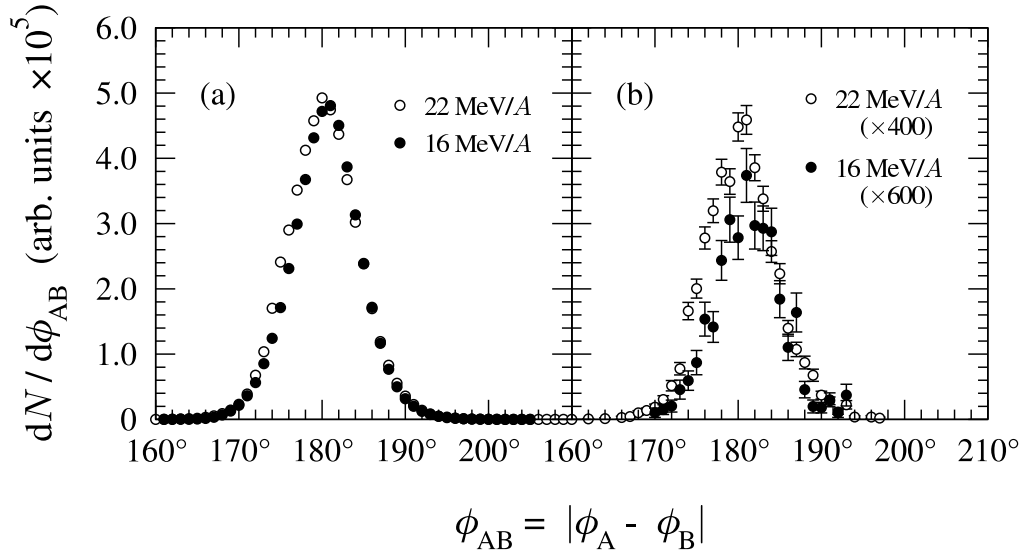
Figure 4.1: Azimuthal correlation angle distributions for coincident fission fragments in the reaction ^{12}C + ^{232}Th at 16 and 22 MeV/A. Measured values for the case of (a) binary and (b) ternary fission. The ternary cases include both isotropic and near-scission emission.

for finite detector resolution using a value of $\sigma_{\mathrm{resolution}} = 0.8°$ for each PPAC, i.e.

$$\mu_2 = \sigma^2 = (\sigma_{\mathrm{measured}})^2 - 2\,(\sigma_{\mathrm{resolution}})^2 \,.$$

The factor 2 in the last term arises from the fact that we must consider the finite resolution of both PPACs used in the measurement.

The mean values for binary events are effectively equal to 180° for both incident energies, indicating that the events in question were indeed composed of correlated fission fragments. Detection of correlated fission fragments was a requirement for the kinematic reconstruction used later to deduce other quantities of interest. The mean values for ternary events are also near to 180°, with widths comparable to those observed for binary events. Two factors contribute to the width of the out-of-plane angular distributions. The dominant factor is emission of neutrons or charged particles following scission (post-scission), which can perturb the angular correlation

Incident Energy	$\langle\phi_{\mathrm{AB}}\rangle_{\mathrm{Binary}}$	$\langle\phi_{\mathrm{AB}}\rangle_{\mathrm{Ternary}}$
22 MeV/A	180.1° ($\mu_2 = 16.0°$)	180.3° ($\mu_2 = 17.9°$)
16 MeV/A	180.6° ($\mu_2 = 14.0°$)	180.7° ($\mu_2 = 15.8°$)

Table 4.1: First and second moments, $\langle\phi_{\mathrm{AB}}\rangle$ and $\mu_2 = \sigma^2$, of the azimuthal correlation angle distributions for coincident fission fragments. Second moments have been corrected for finite detector resolution as described in the text.

between the two fission fragments. These post-scission particles are emitted isotropically in the rest frames of the two accelerated fission fragments, causing the emitting fission fragment to recoil. The random orientation of the recoil momentum leads to a broadening the angular correlation distribution. The width of the out-of-plane angular correlation can be used as an indicator of the excitation energy of the fission fragments following scission [1] (i.e. higher excitation would allow emission of more particles which would lead to a broader distribution of the angular correlation). The smaller values of the second moments observed for ternary events may be an indication that the fission fragments emerge with less excitation energy in ternary fission than in binary fission. This view is consistent with the large energy cost expected for emission of a third fragment from the neck region (see Sec. 1.4.1). However, in the current work the azimuthal correlation angle was used simply to verify the correlation of coincident fission fragments. The second factor that can influence the azimuthal angular correlation is scattering of the fission fragments in the target foil. Although of relatively minor importance compared to post-scission particle emission, scattering of the fission fragments can be a measurable affect the final width of the distribution.

The fission-fragment folding angle, $\theta_{\mathrm{AB}} = \theta_{\mathrm{A}} + \theta_{\mathrm{B}}$ for two correlated fission fragments A and B, (see Fig. 4.2) can be related to the longitudinal component of the linear momentum transferred from the incident projectile to the composite

In the laboratory frame:

$$\theta_{AB} = \theta_A + \theta_B < 180°$$

In the cm frame of the Fissioning Nucleus:

$$\theta'_{AB} = \theta'_A + \theta'_B = 180°$$
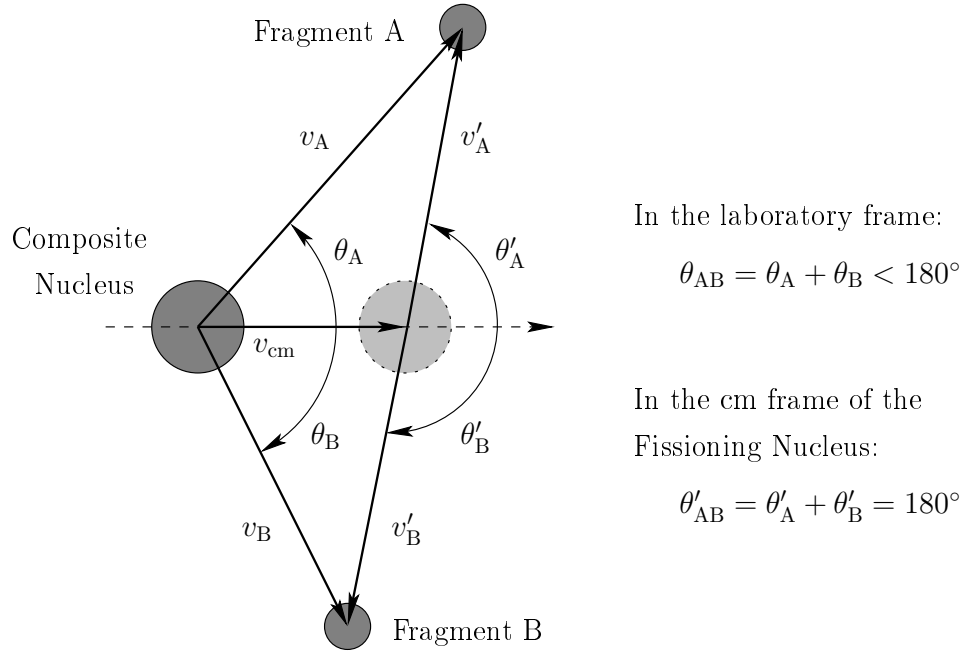
Figure 4.2: Vector diagram defining the fission fragment folding angle, θ_{AB}, for particle induced binary fission. In the center-of-mass of the fissioning nucleus the relative angle of emission between the two fission fragments is constrained by conservation of linear momentum. The forward motion of the composite nucleus leads to a smaller angle ($< 180°$) between the two fission fragments as measured in the laboratory system.

---

system [2]. Knowledge of the linear momentum transfer (LMT) for a given event provides a means to extract information about the collision, such as its centrality or the initial excitation of the composite system [2, 3, 4]. At low to intermediate incident energies, where complete and incomplete fusion are the dominant interaction mechanisms [5], a central, or head-on collision will transfer an appreciable portion of the momentum of the incident particle to the composite nucleus. Conversely, a more peripheral interaction will result in the transfer of considerably less linear momentum, but will lead to composite states of higher angular momentum.

The relationship between the fission-fragment folding angle and LMT has been
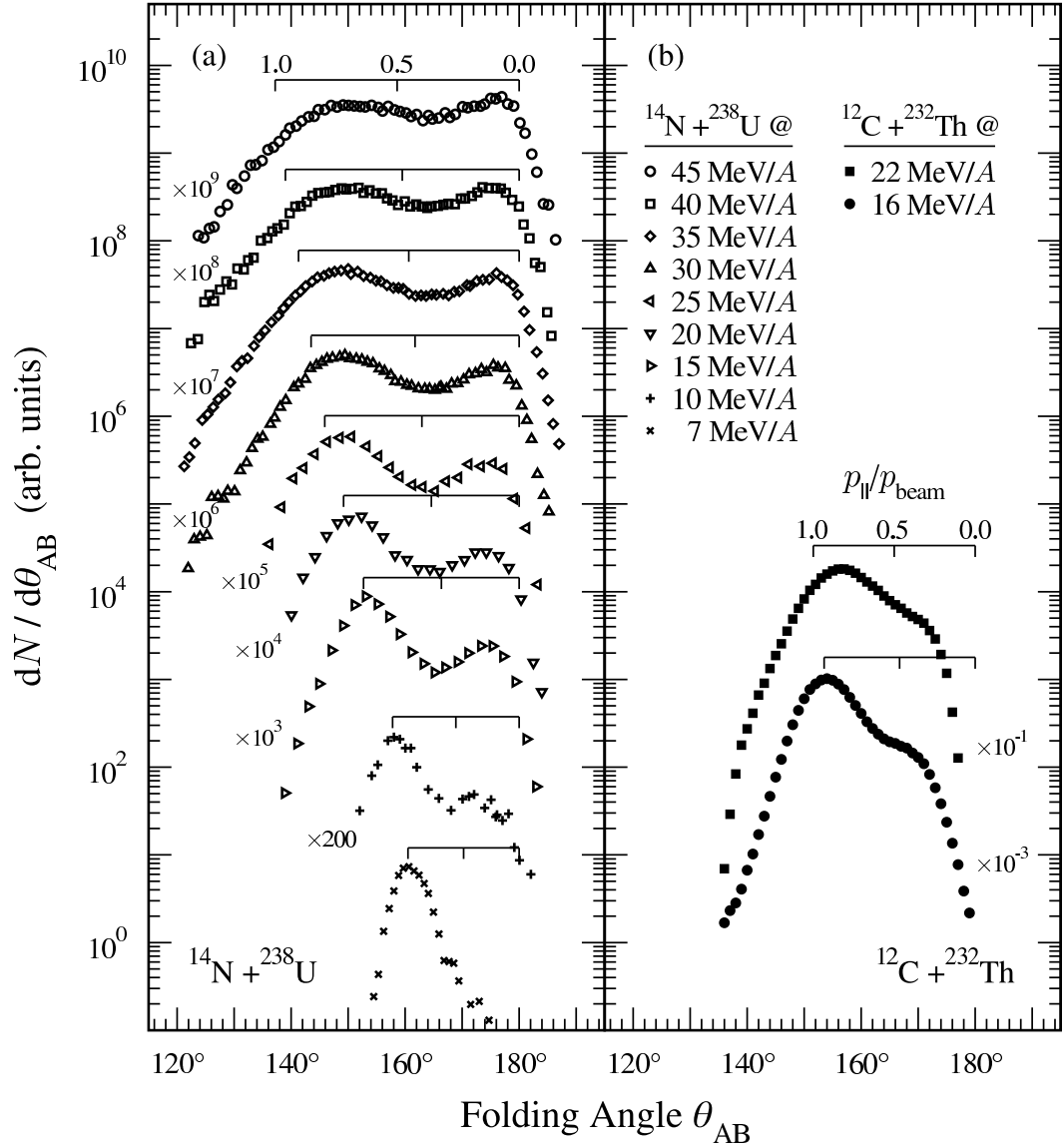
Figure 4.3: Effect of incident energy on the binary folding-angle distributions for coincident fission fragments in the reactions (a) ^{14}N + ^{238}U, and (b) ^{12}C + ^{232}Th at the listed incident energies. The deduced fractional linear momentum transfer (FLMT) scale, $p_{||}/p_{\text{beam}}$, is shown above each distribution. Data for ^{14}N + ^{238}U are from Ref. [5].

well documented for numerous cases of light and heavy-ion-induced binary fission [1, 2, 5, 6, 7, 8, 9]. Figure 4.3 provides a comparison of the measured binary folding-angle distributions from the present work with those for the system ^{14}N + ^{238}U at a number of incident energies [5]. Looking first at the data for the ^{238}U(^{14}N,f) reactions in panel (a), there are several important features to note: (1) At low incident energies, near the Coulomb barrier, the distribution of folding angles shows a high probability for events involving full LMT ($p_{||}/p_{\mathrm{beam}} = 1.0$). Events resulting from peripheral interactions are strongly suppressed, even for the highly fissile ^{238}U nucleus. (2) As the incident energy increases, the probability for fission arising from more peripheral interactions ($p_{||}/p_{\mathrm{beam}} << 1.0$, incomplete fusion) increases. At the highest incident energies indicated in the figure, the probability for fission arising from less than full LMT is comparable or greater than for complete fusion. (3) As the incident energy increases the entire distribution becomes broader.

Looking now at the ^{232}Th(^{12}C,f) binary fission data (panel (b) in Fig. 4.3), the following observations can be made: (1) The peripheral component of the folding-angle distribution is more prominent for the higher incident energy, in agreement with the trends observed in the ^{238}U(^{14}N,f) data. The probability for fission following incomplete fusion increases with increasing incident energy. (2) For both incident energies, the peripheral component is less pronounced than for ^{238}U(^{14}N,f) at similar energies. This difference can be understood by considering the lower fissility of ^{232}Th compared to ^{238}U. (3) The most probable folding angle, $\theta_{\mathrm{AB}}^{mp}$ (denoted by arrows in Fig. 4.4), is higher for the 22 MeV/A data than for the 16 MeV/A data, indicating a decreased probability for complete fusion at the higher incident energy. This trend is also consistent with the results from [5]. At higher energies incomplete fusion begins to dominate the total reaction cross section, either through projectile breakup and subsequent capture or the onset of pre-equilibrium emission.

Figure 4.4 presents the measured fission fragment folding angle distributions for both binary and ternary events in the ^{12}C + ^{232}Th reaction at (a) 22 MeV/A and (b) 16 MeV/A. Again, the results for ternary events are integrated over $3 \leq Z_{\mathrm{IMF}} \leq 13$
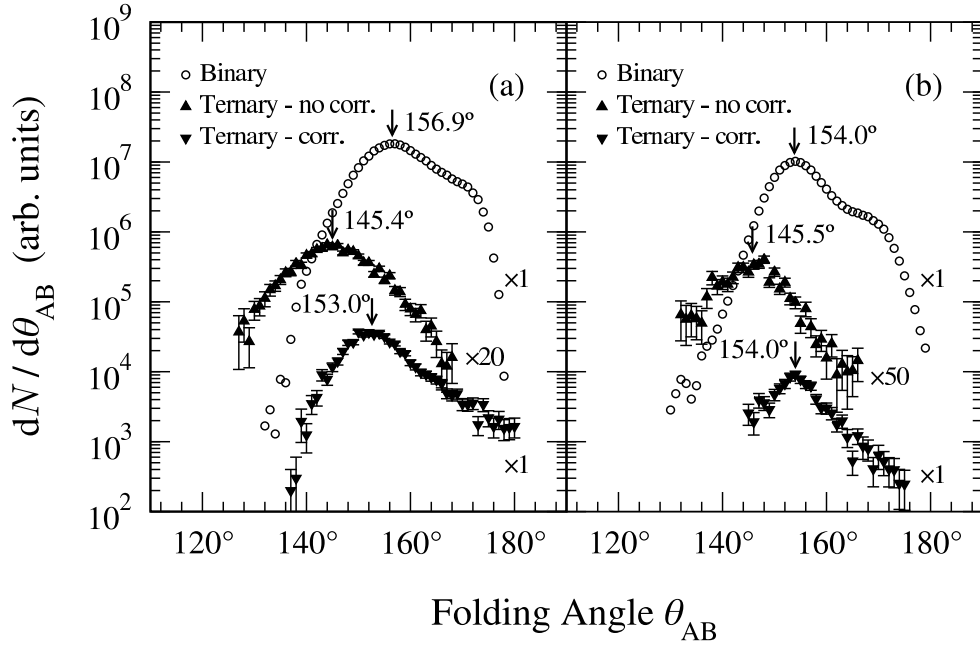
Figure 4.4: Folding angle distributions for coincident fission fragments in the reaction ^{12}C + ^{232}Th at (a) 22 MeV/A and (b) 16 MeV/A. Measured values for the case of binary fission (open circles), ternary fission without correcting for recoil of the fissioning nucleus (up triangles) and ternary fission after correcting for recoil (down triangles). The ternary cases include both isotropic and near-scission emission.

for the 22 MeV/A data and $3 \leq Z_{IMF} \leq 12$ for the 16 MeV/A data. To compare with the results for binary fission the data for ternary fission are presented before (up triangles) and after (down triangles) correcting for the recoil of the fissioning nucleus due to emission of the ternary particle at backward angles (necessary for deducing the FLMT, see App. B). At both incident energies the uncorrected ternary folding angle distribution is peaked near 145° (indicated by the arrows in the figure), $\approx 10°$ less that the most probable values for binary fission. Most of this difference is the result of the recoil, as can be seen by comparing the binary and corrected ternary distributions. For the 22 MeV/A data the difference between the binary and corrected ternary values is now only 3.9°, and there is no difference in the 16 MeV/A

data. Based on the observations from Fig. 4.3 we can conclude that ternary fission is preferentially associated with larger LMT. At both incident energies the corrected distributions are peaked near 100% LMT and seem to lack the low LMT shoulder observed for binary fission.

4.2   IMF Energies

Center-of-mass kinetic energy distributions for beryllium and carbon fragments detected in coincidence with two correlated fission fragments are displayed in Fig. 4.5. Panels (a) and (b) show the center-of-mass energy spectra, for beryllium and carbon fragments respectively, as measured $\sim 50°$ with respect to the scission axis. Gaussian fits to the energy spectra yielded mean center-of-mass energies of $\langle E_{\mathrm{cm}} \rangle = 43.8$ ($\sigma = 10.5$) MeV for beryllium and $\langle E_{\mathrm{cm}} \rangle = 54.5$ ($\sigma = 8.0$) MeV for carbon. The horizontal bars in Fig. 4.5 indicate the ranges used for the fits. The energy spectra and the extracted mean energies are consistent with the Coulomb barrier for emission from a nearly spherical source the size of the emitting composite system.

Panels (c) and (d) of Fig. 4.5 depict the center-of-mass energy spectra for beryllium and carbon fragments, respectively, measured $\sim 90°$ with respect to the scission axis. Both spectra exhibit a bimodal distribution, in agreement with earlier investigations of ternary fission [10]. Vertical dotted lines indicate the energy cuts used to separate the low energy component, associated with near-scission emission, from the high energy, isotropic component. Gaussian fits to the low energy components yielded mean center-of-mass energies of $\langle E_{\mathrm{cm}} \rangle = 21.9$ ($\sigma = 10.6$) MeV for beryllium and $\langle E_{\mathrm{cm}} \rangle = 26.1$ ($\sigma = 12.0$) MeV for carbon. These values are well below the Coulomb barrier for emission from a compact source. Fits to the high energy components yielded values of $\langle E_{\mathrm{cm}} \rangle = 42.5$ ($\sigma = 7.0$) MeV for beryllium and $\langle E_{\mathrm{cm}} \rangle = 53.3$ ($\sigma = 10.9$) MeV for carbon. These values are in good agreement with those determined over a similar energy range in panels (a) and (b). Also, the overall yield of the high energy component, after accounting for variations in detector
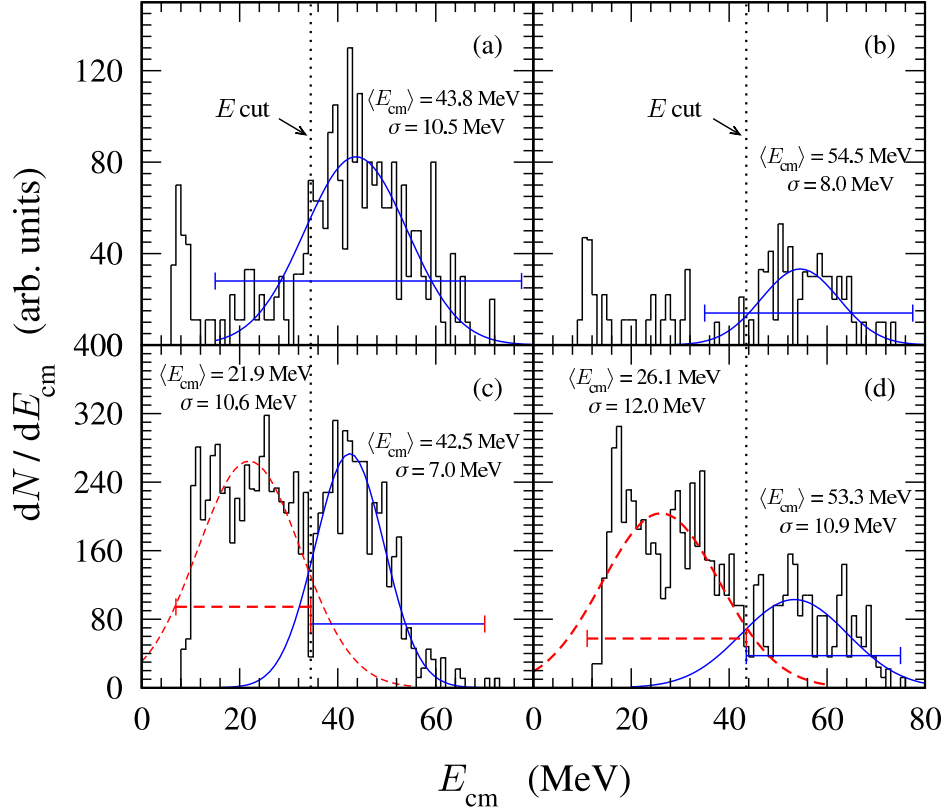
Figure 4.5: Center-of-mass energy spectra for Be and C fragments measured in coincidence with two correlated fission fragments. Panels (a) and (b) show energy spectra for Be and C respectively, measured ∼50° with respect to the scission axis. Panels (c) and (d) show energy spectra for Be and C respectively, measured ∼90° with respect to the scission axis. The dotted lines indicate the energy cut used to separate the low energy, near-scission component from the high energy, isotropic component. The curves represent Gaussian fits to the high energy (solid blue) and low energy (dashed red) components. Mean energies and standard deviations from the fits are listed. The capped horizontal lines indicate the ranges used for the corresponding fits.
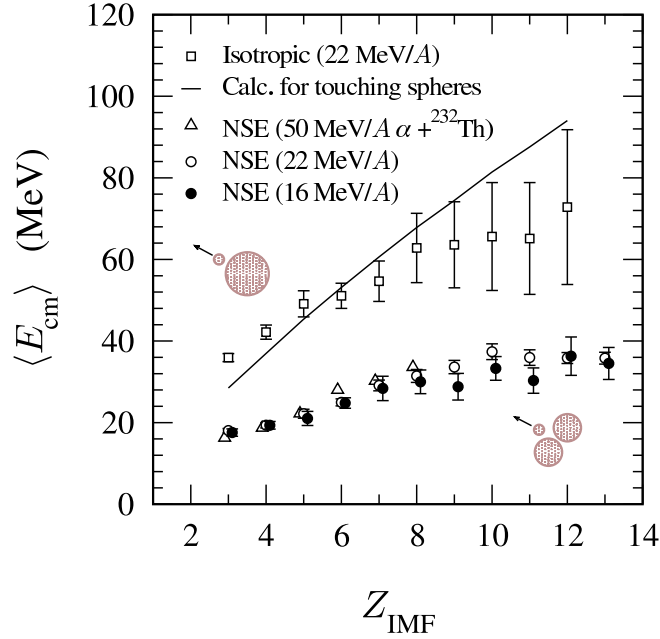
Figure 4.6: Mean center-of-mass kinetic energy of ternary fragments as a function of Z_{IMF} for near-scission (open and closed circles and open triangles) and isotropic (open squares) emission.

solid angle, is comparable between the two angular regions, indicative of an isotropic emission mechanism, for which there is no correlation with the orientation of the scission axis.

The dependence of the average center-of-mass kinetic energy on Z of the emitted fragment is depicted in Fig. 4.6. Both the isotropic and near-scission components exhibit a roughly linear dependence of the average energy on Z_{IMF}. The solid line indicates the Coulomb barrier for a touching-spheres scenario given by,

$$E_c = \frac{1.44 Z_{\text{IMF}} \left(Z_{\text{source}} - Z_{\text{IMF}} \right)}{1.4 \left[A_{\text{IMF}}^{1/3} + \left(A_{\text{source}} - A_{\text{IMF}} \right)^{1/3} \right] + 2} \text{ MeV} \tag{4.1}$$

where Z_{source} and A_{source} have been approximated by 90 and 232, respectively, to account for incomplete fusion and pre-scission emission of nucleons. The kinetic

energies for isotropically emitted fragments are roughly consistent with this simple formula, indicating that these fragments are emitted while the excited composite system is still relatively compact. Fragments emitted near scission have average kinetic energies significantly lower than those associated with statistical emission from a spherical source. This result is consistent with emission of the near scission IMFs from an extended source as depicted by the cartoon in the lower right corner of the figure. Data are also included for near-scission emission observed in the reaction ^{4}He + ^{232}Th at 50 MeV/A (open triangles) [11]. The agreement between the data for near-scission emission in the three reactions would indicate that the extent of the emitting system is not greatly affected by the initial excitation energy.

4.3 Kinematic Correlations Between Fission Fragments and IMFs

In order to understand the conditions under which fragments are emitted, we have examined the correlations between the fission-fragment folding angle and IMF emission. The folding-angle technique has been well established as a means of deducing the linear momentum imparted to the fissile target nucleus [5], from which the resulting excitation of the composite system can be inferred. For reference, binary fission following complete fusion (full linear momentum transfer) should yield an average folding angle of $\langle \theta_{AB} \rangle = 152°$ for the 22 MeV/A case. In contrast, the most probable folding angle observed for binary fission events associated with non-peripheral collisions is $\theta_{AB} = 156.9°$ (as indicated in panel (a) of Fig. 4.4), which is consistent with the incomplete fusion of projectile and target nucleus in the formation of the composite system.

In Fig. 4.7 the dependence of the average folding angle on Z_{IMF} in ternary fission events is presented. In panel (a) we compare the results for isotropic and near-scission emission in the 22 MeV/A reaction, and in panel (b) the results for near-scission emission at the two incident energies are compared. For the isotropically

emitted fragments (open squares) the mean folding angle decreases monotonically with increasing Z_{IMF} due to the recoil imparted to the fissioning system by the backward emitted IMF. Since the angle, kinetic energy, and Z of the IMF are measured, the magnitude of this recoil can be calculated by assuming a Z/A ratio for the IMF that is consistent with previous measurements [10, 11]. The solid line in panel (a) represents the mean folding angle predicted by the assumption of 87% linear momentum transfer from the projectile to the composite system (incomplete fusion), including corrections for recoil of the fissioning system due to the IMF emission prior to significant deformation and subsequent fission of the residual nucleus. The folding angle associated with isotropically emitted ternary fragments can be understood reasonably well within such a scenario. In contrast, IMFs emitted near-scission (open and closed circles) exhibit a more complex behavior. While the mean folding angle for near-scission IMFs with $Z \leq 7$ also decreases monotonically, for $Z \geq 8$ the trend is reversed, and the mean folding angle begins to increase (decreasing LMT) with increasing Z. This trend would indicate that the latter fragments are emitted in events in which less linear momentum was initially transferred to the composite system, i.e. near-scission emission of IMFs with $Z \geq 8$ are associated with more peripheral collisions.

The dashed line in both panels of Fig. 4.7 represents the mean folding angle associated with the assumption of 83% linear momentum transfer from the projectile to the composite system, including corrections for recoil of the fissioning system due to the IMF emission and subsequent fission. However, as with the solid line in panel (a), it is assumed that IMF emission occurs prior to significant deformation of the composite system. Since this is not the case for near-scission emission (the net Coulomb repulsion immediately after IMF emission is significantly lower for near-scission emission), it is expected that the linear momentum transfer is actually greater than 83% for the near-scission events. This expectation is confirmed in the event-by-event analysis, where the recoil is determined by conservation of linear momentum using the assumed mass of the IMF and its energy as measured in the
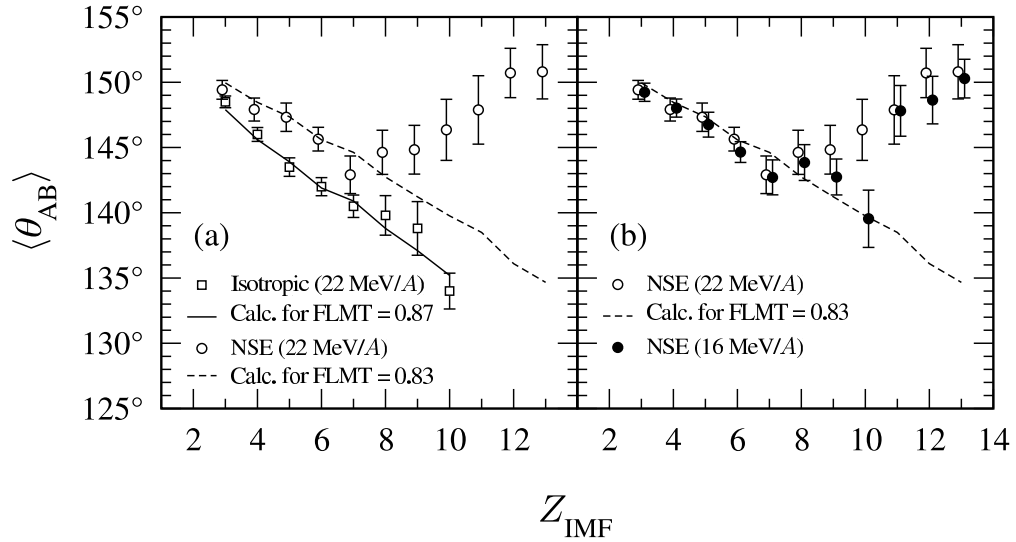
Figure 4.7: Dependence of the mean fission-fragment folding angle on Z_{IMF} for near-scission (open and closed circles) and isotropic (open squares) emission. The points for NSE are offset ± 0.1 units in Z_{IMF} for clarity.

IC telescopes. In comparing the results for near-scission emission at the two incident energies, panel (b) of Fig. 4.7, we find that there are no significant differences aside from the points for $Z_{IMF} = 10$. Since there is good agreement for all other values of Z_{IMF}, the disagreement for $Z_{IMF} = 10$ is most likely due to a systematic error in the analysis that has so far eluded identification.

We have determined the average fraction of the linear momentum transferred ($\langle FLMT \rangle$) by the projectile to the composite system by iteratively correcting on an event-by-event basis for the recoil of the backward emitted IMF (for details see Appendix B). The dependence of $\langle FLMT \rangle$ on Z_{IMF} is shown in Fig. 4.8. The "isotropically emitted" fragments are associated with a nearly constant $\langle FLMT \rangle$ of 90% within the measurement uncertainties. The $\langle FLMT \rangle$ associated with NSE IMFs decreases monotonically from 83% to 25% with increasing Z_{IMF}. Decreasing linear momentum transfer is presumably associated with decreasing energy deposition into the composite system. Hence, the observed decrease in $\langle FLMT \rangle$ with the Z of the
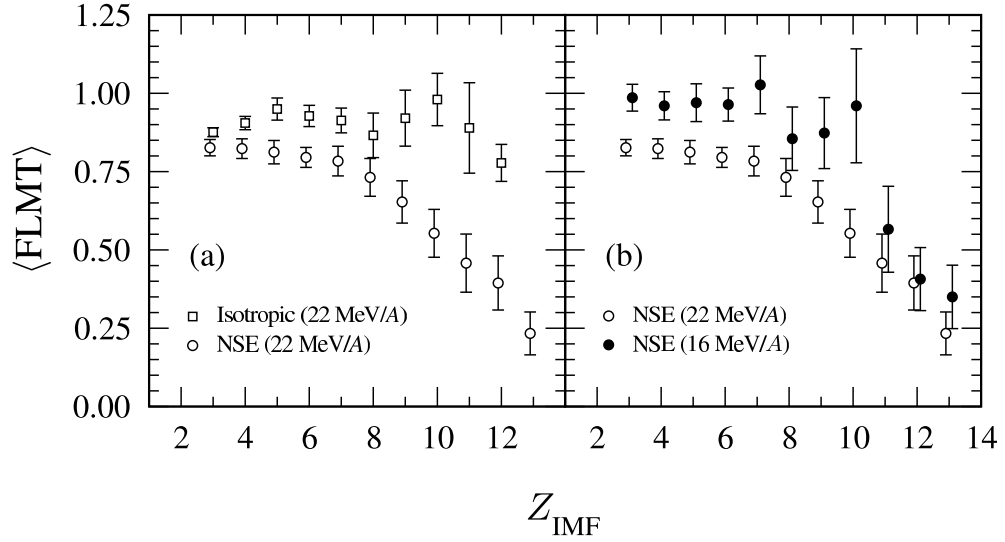
Figure 4.8: Dependence of the mean fractional linear momentum transfer (FLMT) on Z_{IMF} for near-scission (open and closed circles) and isotropic (closed squares) emission. The points for NSE are offset ± 0.1 units in Z_{IMF} for clarity.

near-scission IMFs qualitatively suggests that NSE of heavy fragments is *not* driven solely by excitation energy considerations.

4.4   IMF Yields

The yield distributions of the isotropic and the near-scission components are shown in Fig. 4.9 for the 22 MeV/A reaction. Both components are reasonably well described by a power-law type behavior $\sigma(Z) \propto Z^{-\tau}$. For the isotropic component the power-law parameter is $\tau = 2.94 \pm 0.14$. Near-scission emission has a much flatter Z distribution ($\tau = 1.17 \pm 0.10$), consistent with previous measurements [10, 11], and for heavy IMFs ($Z \geq 8$) the yield distribution is essentially constant. The power law parameter, τ, is believed to be indicative of the details of the fragmentation process [12]. For multifragmentation reactions induced by light and heavy ions, τ is observed to be a monotonically decreasing function of the projectile energy, down to
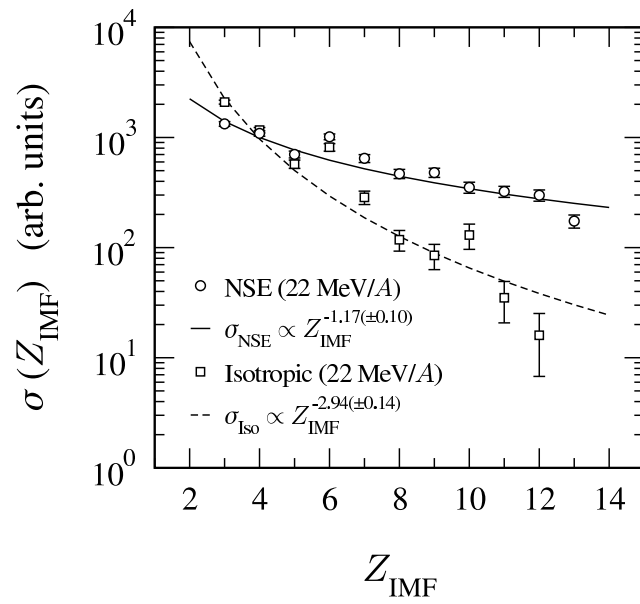
Figure 4.9: Yield distributions of ternary fragments for near-scission (circles) and isotropic (squares) emission. Curves represent power-law fits to the data.
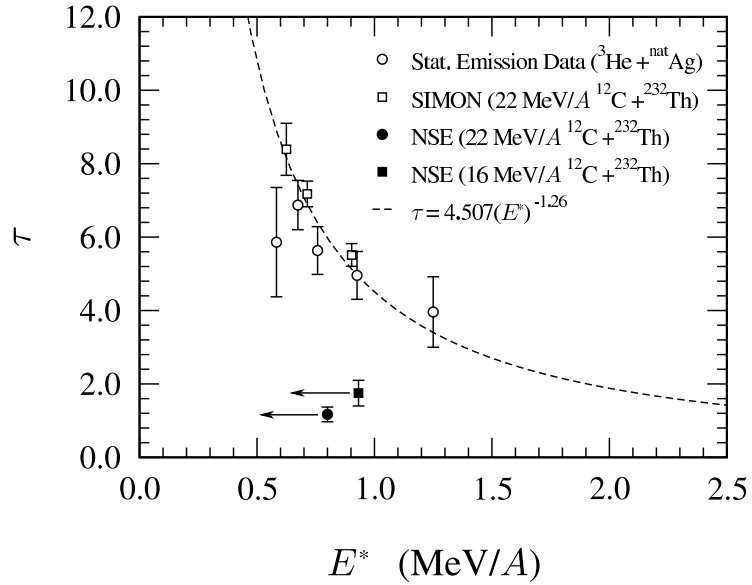
Figure 4.10: Comparison of the experimental τ parameters for NSE from the current work with values deduced from experimental statistical emission data and statistical model calculations. The dashed line is a power-law fit to the data for statistical emission.

a minimum of $\tau \simeq 2.0$, which occurs at $E_{\mathrm{lab}} \simeq 2$ GeV [13]. The systematic behavior of the power law parameter for multifragmentation reactions has been frequently cited as evidence that these reactions proceed by a common decay mechanism. In a statistical emission framework, a flatter yield distribution (smaller τ) is associated with higher excitation of the emitting system. Due to prior neutron emission from the composite system, as well as transfer of energy into deformation, one would expect near-scission emission to be associated with lower excitation energy than the isotropic component. Consequently, the flatter yield distribution for near-scission emission suggests a decay mode *not* solely dependent on excitation energy. This view is supported by the apparent dependence of the NSE fragment mass on the angular momentum of the entrance channel discussed in Sec. 4.3.

The τ parameters extracted from the IMF yield distributions in the present work are compared to values obtained from experimental and theoretical statistical emission data in Fig. 4.10. The data are plotted as a function of the initial excitation energy per nucleon of the composite system. Open circles are the result of power-law fits to the elemental yields for $3 \leq Z_{\rm IMF} \leq 11$, observed in the reaction ^{3}He + $^{\rm nat}$Ag at incident energies of 45–130 MeV [14]. Open squares are from power-law fits to the yield of fragments with $3 \leq Z_{\rm IMF} \leq 6$ obtained using the statistical decay code SI-MON [15]. The model calculations were for the reaction ^{12}C + ^{232}Th at 264 MeV assuming fractional linear momentum transfer values of $FLMT = 1.00$, 0.83, and 0.75. For these data the power-law parameter τ decreases monotonically with increasing excitation, in agreement with the systematics described in Ref. [13]. This trend expresses the increasing probability for the emission of larger fragments as the necessary energy becomes available [16]. The dashed line is a power-law fit to the statistical emission data made primarily to guide the eye.

The closed points in Fig. 4.10 represent the results for NSE in the two ^{12}C-induced reactions of the current work. The initial excitation energy was calculated on an event-by-event basis within the framework of the massive transfer model as described in Sec. B.4. The mean value was integrated over $3 \leq Z_{\rm IMF} \leq 12$ in the 16 MeV/A reaction and $3 \leq Z_{\rm IMF} \leq 13$ in the 22 MeV/A reaction and plotted against the corresponding power-law parameter. It should be further noted that the deduced excitation energy for the NSE case corresponds to an upper limit based on the deduced $FLMT$ in the entrance channel. At scission much of the initial excitation will have been converted into deformation energy or lost to pre-equilibrium particle emission. This fact is indicated in the figure by the arrows on the two NSE points. However, even if we consider just the initial excitation energy, we see a marked difference for NSE when compared to the points for statistical evaporation. The value of the τ parameter is significantly lower, by a factor of three or more, for the case of NSE at similar initial excitation. This difference further supports the idea of a substantially different emission mechanism than that believed to be responsible

for strictly statistical emission.

Figure 4.11 shows a comparison of NSE yields for heavy-ion-induced ternary fission from the current work with yields for spontaneous and thermal-neutron-induced (n_{th}-induced) ternary fission. The spontaneous and n_{th}-induced data show a strong odd-even effect indicating that the near-scission IMFs are being emitted from a system at low temperature, where shell effects are still important. As the interaction becomes more violent, the features in the yield curve arising from shell structure begin to disappear, indicating emission from a hotter source, i.e. there is more excitation energy available at scission which washes out the shell structure seen at lower energies. Also, in heavy-ion-induced ternary fission the yields extend to heavier Z_{IMF}. This extension to heavier neck fragments could be another indication that the angular momentum of the fissioning system plays an important role in the dynamics of the three-body breakup.

4.5   Relative IMF Yields

To explore the role of excitation energy on fragment emission further, we have constructed the yield ratios between different IMFs as a function of excitation energy. For statistically emitted fragments these ratios should be sensitive to the IMF emission barriers. The average initial excitation of the composite system, $\langle E^* \rangle$, was calculated in the framework of an incomplete fusion model using the deduced FLMT,

$$\langle E^* \rangle = E_p \, \rho \, \frac{A_t}{A_t + \rho A_p} \sqrt{1 - \left(\frac{v_p}{c} \right)^2} + \langle Q \rangle \tag{4.2}$$

where E_p is the projectile energy, ρ is the fractional linear momentum transfer from the projectile to the composite system (*FLMT*), A_t and A_p are the mass numbers of the target and projectile, respectively, v_p is the velocity of the projectile and $\langle Q \rangle$ is the average Q value of reaction channels consistent with the given ρ (see Sec. B.4 for a detailed description of how the initial excitation energy was determined). Deduced values for the linear momentum transfer covered a range of $0.25 \lesssim \rho \lesssim 1.0$ as shown in Fig. 4.8.
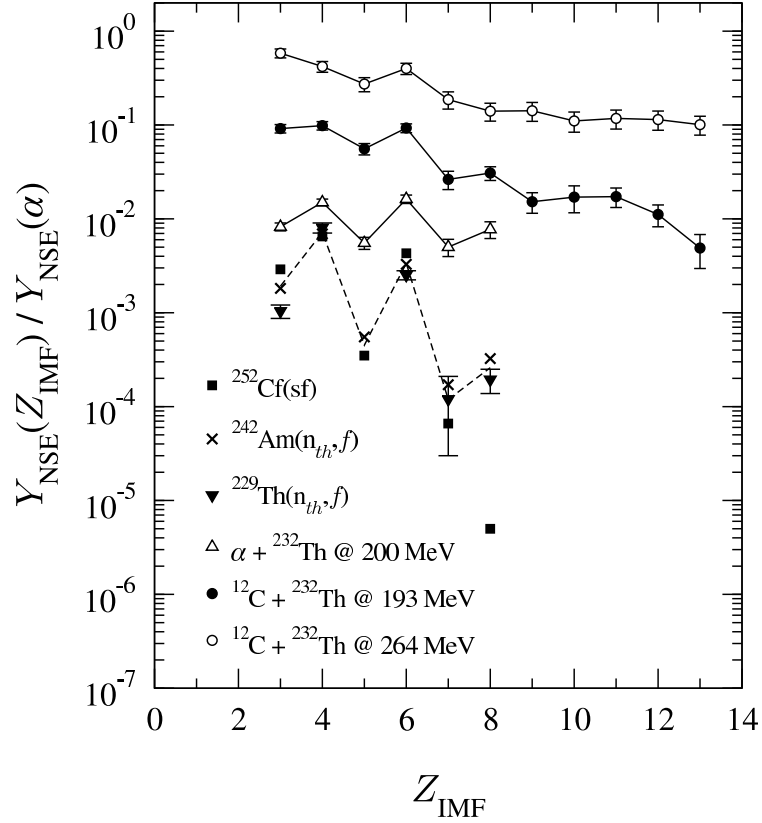
Figure 4.11: Relative IMF yields for near scission emission. Comparison of results from the current work with data from spontaneous ternary fission of ^{252}Cf [17], n_{th}-induced ternary fission of ^{242}Am [18] and ^{229}Th [19] and α-particle induced ternary fission [11]. Yields are plotted relative to the near-scission α yield for each system. Lines are to guide the eye with the dashed line representing the average for the spontaneous and n_{th}-induced data.
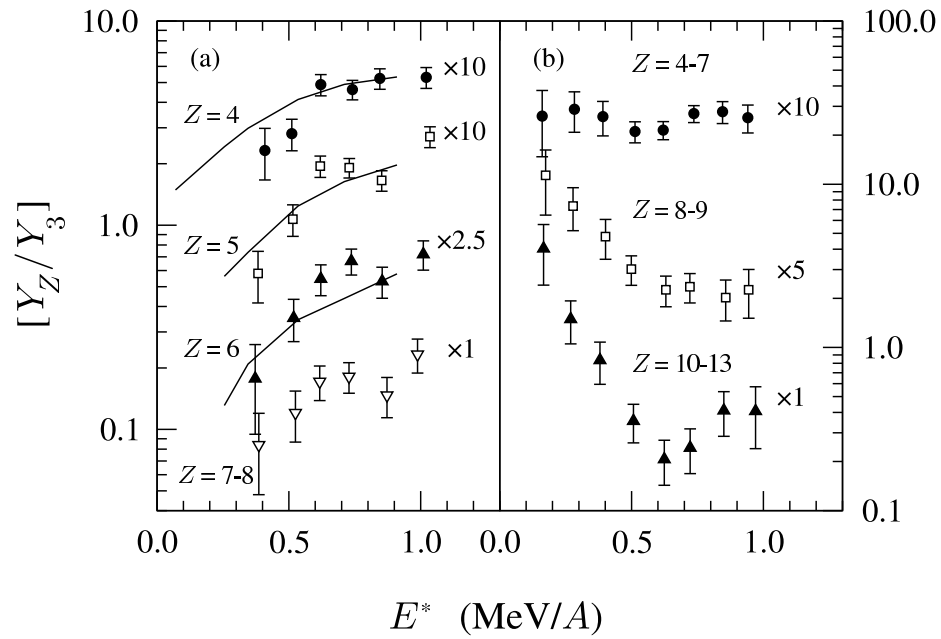
Figure 4.12: Relative yields of various IMFs as a function of the initial excitation of the composite system. Data are for (a) isotropically emitted IMFs, and (b) IMFs emitted from the neck region (NSE). Renormalized predictions of the statistical model SIMON are shown as solid lines in (a). Yields are plotted relative to the Li yield.

The dependence of the isotropic IMF yield relative to lithium on excitation energy is shown in panel (a) of Fig. 4.12. The experimental data exhibit an exponential increase with increasing excitation energy. This behavior can be qualitatively understood in terms of the Z dependence of the IMF emission barriers. Since the emission barrier increases with increasing Z_{IMF}, for a given excitation energy one observes a reduced emission probability for IMFs with larger Z. With increasing excitation energy this suppression in emission probability decreases.

We also compared the experimental data with the predictions of the statistical model SIMON [15]. The solid lines in panel (a) of Fig. 4.12 depict the predicted yields of Be, B and C relative to Li fragments as a function of E^*/A. As SIMON tends to seriously under-predict fragment yields it was necessary to renormalize the results of the calculations for comparison with the data. The model semi-quantitatively reproduces the main trend observed in the experimental data, showing a 3-4 fold increase in the relative yield over the measured excitation energy window. Thus, the behavior of isotropically emitted IMFs is consistent with statistical emission from a compact source.

The dependence of the relative yields of NSE on the initial excitation of the system is shown in panel (b) of Fig. 4.12. The yields of near-scission fragments with $Z = 4 - 7$, $Z = 8 - 9$, and $Z = 10 - 13$ have been normalized by the yield of near-scission $Z = 3$ fragments. In marked contrast to the trends observed in panel (a) of Fig. 4.12, the relative yields in panel (b) do not show an exponentially increasing behavior with increasing excitation energy. For neck-emitted $Z = 4 - 7$ fragments the relative yield is approximately constant with increasing excitation energy. Such behavior could be understood if the emission barriers were essentially the same or if no emission barriers existed – consistent with emission of neck fragments from extended configurations. For $Z = 8 - 9$, however, the relative yield *decreases* with increasing excitation energy. A factor of 5 decrease is observed between the cases involving the lowest excitation (peripheral collisions) and cases involving the highest excitation (more central collisions). In the case of $Z = 10 - 13$, a suppression by a
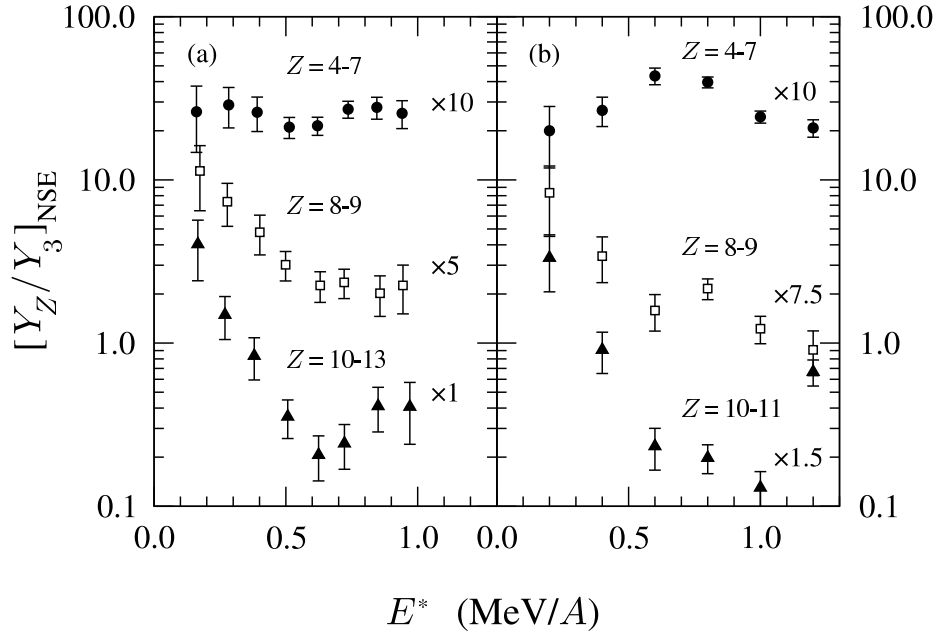
Figure 4.13: Relative yields of various IMFs emitted from the neck region (NSE) as a function of the initial excitation of the composite system. Data are for the ^{12}C + ^{232}Th reaction at (a) 22 MeV/A and (b) 16 MeV/A. Yields are plotted relative to the Li yield.

factor of approximately 20 is observed between $E^*/A = 0.2$ and $E^*/A = 0.6$. This behavior is inconsistent even with a zero emission barrier scenario and, we believe, is a strong indication of a non-statistical, dynamical origin of NSE of heavy fragments.

In understanding the association of significant heavy fragment neck yield with low linear momentum transfer, two points are noteworthy. First, for heavy fragments ($Z \geq 10$) the mass of the fragment approaches the mass of the neck. Thus, statistical emission from the neck would require evaporation of almost the entire "source" and is suppressed on the basis of source size effects. Suppression of statistical emission is important if one is to isolate a co-existing/competing decay mechanism clearly. Second, for collisions involving modest linear momentum transfer (25%), the deformation (stretching) introduced into the target nucleus may be significant. In
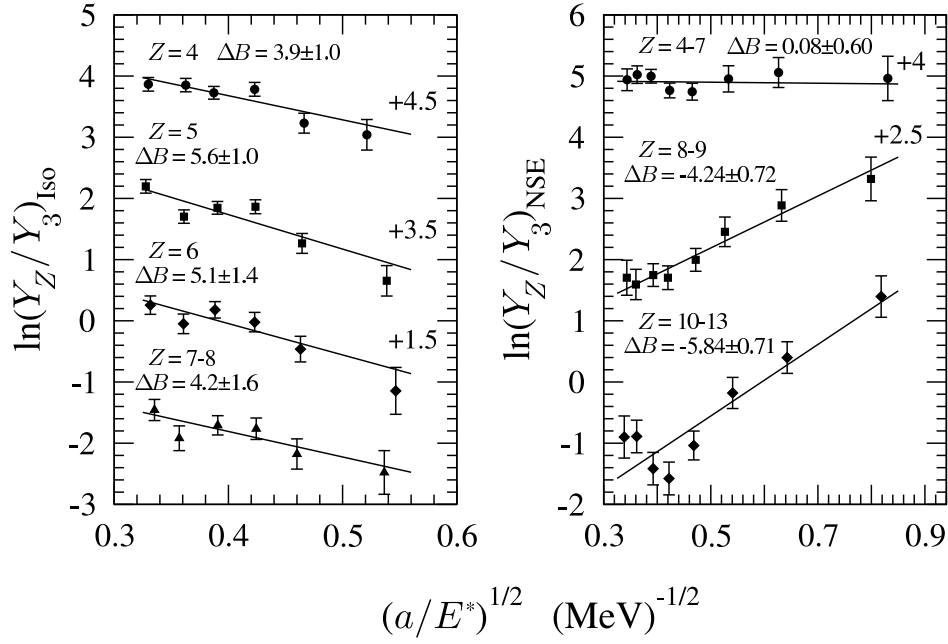
Figure 4.14: Relative yields of isotropic (left panel) and neck (right panel) emitted IMFs as a function of $\sqrt{a/E^*}$ for the reaction ^{12}C + ^{232}Th at 22 MeV/A. Extracted values for the relative emission barrier, ΔB, are given for each fit. The level density parameter was calculated as $a = A/9$ where A is the mass of the composite system.

contrast, central collisions should yield less deformation and greater heating of the system. Qualitative expectations dictate that survival of any initial stretching of the excited composite system into the fission channel results in a more elongated scission configuration and consequently a larger middle fragment. The survival of such an initial stretching should depend sensitively on the nature of nuclear dissipation. Preliminary calculations with a dynamical model of fission [20] bear out these qualitative expectations [21].

It has recently been suggested by Moretto *et. al.* that the results obtained in this work ARE consistent with statistical emission [22]. We present their argument

(based on our data) and our counter-argument. In terms of statistical theory, the emission probability for a fragment with a Z dependent emission barrier B_Z can be written as

$$P_Z \propto A_Z \, e^{-B_Z/T}$$

where P_Z is the probability for emission, T is the temperature of the emitting system and A_Z is a proportionality constant that depends on Z. The emission probability for a fragment with atomic number Z relative to that for $Z = 3$ can then be constructed:

$$P_Z/P_3 = K_Z \, e^{-(B_Z - B_3)/T} = K_Z \, e^{-\Delta B/T}$$

where $K_Z = A_Z/A_3$ and $\Delta B = (B_Z - B_3)$ represents the relative emission barrier. Taking the natural logarithm of both sides of this expression gives

$$\ln(P_Z/P_3) = \ln(K_Z) - \Delta B/T = \ln(K_Z) - \sqrt{a/E^*} \, \Delta B. \qquad (4.3)$$

Here we have made the substitution $1/T = \sqrt{a/E^*}$ where a is the level density parameter, calculated as $a = A/9$ MeV^{-1}, where A is the average deduced mass of the composite system. A transformation of the data in Fig. 4.12 results in a plot that is consistent with Eq. 4.3 as is shown in Fig. 4.14. Linear fits to the data allow the extraction of the relative emission barrier, ΔB, with respect to the emission barrier for Li fragments (cf. Eq. 4.3). For the case of isotropic emission the slopes are positive, indicating an increasing barrier which is qualitatively consistent with the results from liquid drop model calculations [22]. For neck emission however, the relative emission barriers are nearly zero for $Z = 4$–7 and decrease for $Z = 8$–9 and $Z = 10$–13. The interpretation for these trends is consistent with that of the present work but based strictly on statistical model arguments [22]. These trends suggest that the neck is thick for $Z = 3$–7, the barrier being the energy necessary to create the extra surface in the two cuts required to break the fragment loose, while for $Z = 8$–13 the neck is long and *thin* and the two cuts are less expensive in terms of the required energy. However, an attempt to explain the results of the current work in terms of purely statistical decay ignores several important points [23].

The entire question of statistical emission depends critically upon which modes constitute the "bath". The substantial excitation of collective modes in spontaneous fission suggests that the evolution from saddle to scission is non-adiabatic. For example, the excitation of angular momentum bearing modes is somewhat more than would be expected if the saddle to scission energy were distributed amongst all degrees of freedom [24, 25]. Within this context one could ask, "Should the energy for neck fragment formation (i.e. pinching off of the neck) be taken from the collective or the intrinsic bath?" While a non-adiabatic evolution is thus very possible, let us assume for the sake of argument that the evolution is adiabatic.

The process of ternary fission can then be considered as a slow evolution of the shape, during which statistical decay could produce neck fragments. Here to rephrase Moretto *et al.'s* argument, the events which survive to make the longer, thinner necks are more likely to generate the larger middle fragments ($Z \geq 7$) while those which are less long lived and have shorter thicker necks, are more likely to produce the smaller middle fragments ($Z \leq 6$). The simple energy considerations proposed by Moretto make this scenario plausible and in fact it is supported by the results of more complete dynamical calculations [26]. However, one must question if the conditions which led to the formation of the configurations with short, thick necks and long, thin necks are the same. In this regard, it is important to recall that in spontaneous ternary fission large ($Z \geq 7$) neck fragments are not observed with any significant probability. Why is the present case different? Is it just a hotter heat bath?

It is critical to remember that the excitation energy deduced from the measured linear momentum transfer is at best the *initial* excitation of the composite system. For the isotropically emitted fragments, which are emitted when the system is relatively spherical and before any significant deformation occurs, this initial excitation energy should correspond closely to the excitation at the time of emission of the IMF. In fact, the observed excitation functions are consistent with the fractional linear momentum transfer being closely related to excitation at the time of emission

and shows a clearly Z dependent emission barrier, as seen in Fig. 4.12, by the agreement between the results of the SIMON statistical simulation code (Z dependent emission barriers) and the data for isotropic emission. For these emissions, it seems the hotter bath explains the increased yield as compared to SF.

On the other hand, for fragments emitted later, near scission, the emission probability is more weakly related to the initial excitation. However, the fractional linear momentum transfer is also related to the impact parameter, b, or the angular momentum, ℓ, of the collision. A smaller linear momentum transfer (lower deduced initial excitation) is associated with a more peripheral collision, and a larger linear momentum transfer (higher deduced initial excitation) is associated with a more central collision. The results of the current work suggest that the larger neck emitted fragments ($Z \geq 7$) are preferentially associated with more peripheral collisions. Thus, larger neck fragments arise from different initial angular momentum states than do the smaller neck fragments, and the parent distributions for the two types are different. This fractionation of angular momentum into different parent distributions which subsequently decay statistically is analogous to the situation in strongly damped/deep inelastic heavy-ion collisions. As in that case, the question of interest concerns the dynamical formation of the parent distributions.

Nuclear dissipation of course couples the collective modes to intrinsic ones leading to excitation of the system at scission. Thus, the interplay of dynamics and statistics depends sensitively on the nature of nuclear dissipation. Detailed studies of neck/ternary fission may provide new insight into the dynamical and statistical factors influencing fragment formation and ultimately lead to a better understanding of nuclear dissipation.

4.6   Ternary Fission Cross-section

In order to determine the ternary fission cross-section, it was first necessary to calculate the binary fission cross-section from the measured binary fission data. Table 4.2 summarizes the measured binary fission rates for the reaction ^{12}C + ^{232}Th at 193

MeV for four runs. Cross-sections for the 264 MeV experiment were not determined because these data were not available. In Table 4.2, t is the duration of each run in seconds, N indicates the uncorrected total number of binary events measured in each run, N' takes into account corrections due to the geometric efficiency of the detector coverage as well as down-scaling in the data acquisition electronics and detector/data acquisition dead-time, and R' is the corrected binary fission rate in events per second. The dead-time reflects the time necessary for the data acquisition system to process an event. While an event is being processed, any additional events must be discarded. Since the ternary fission cross-section was expected to be several orders of magnitude less than the cross-section for binary fission, a down-scaler unit was used to limit the possibility that the data acquisition system would be in a busy state due to a binary event and be unavailable to record a ternary event. Binary events were down-scaled by a factor of 32 in both experiments; that is, only every 32nd binary event was processed by the data acquisition system and written to tape. The time-to-live factor, $f_t = t_{\text{live}}/t_{\text{real}}$, is a ratio of the time during which the data acquisition system was able to accept new events to the actual time of the run. This factor quantifies the dead-time allowing the data to be corrected to account for events that occurred during the time the data acquisition system was busy. The binary fission rate was calculated as

$$R' = \frac{N'}{t} = \frac{N\,s}{\epsilon f_t t} \tag{4.4}$$

where s is the down-scaling factor, ϵ is the geometric efficiency correction (see Appendix C), and the remaining variables are as described above.

In order to extract the fission cross-section it is necessary to know the incident beam current, I_{beam}. To determine the beam current an Ortec 439 Digital Current Integrator was connected to the data acquisition system during the last four data runs (46,47,51 and 52). The module was set to provide one logic pulse for every 10^{-9} Coulombs of charge collected at the beam dump Faraday cup (F.C.). This amount of charge is equal to 6.242×10^9 units of elementary charge, e, or 1.040×10^9 $(e/6)$ $^{12}\mathrm{C}^{6-}$ nuclei. To ensure its accuracy, this F.C. was calibrated by comparison with

Run #	t (s)	N	f_t	N'	R' (s^{-1})
46	12420	7961400	0.719909	635436708	5.116×10^4
47	13020	8573100	0.667081	738533588	5.672×10^4
51	4920	3094845	0.643116	276336275	5.617×10^4
52	780	389820	0.617089	36262630	4.649×10^4

Table 4.2: Experimental rates for binary fission in the reaction ^{12}C + ^{232}Th at 193 MeV. See text for a description of the headings.

Run #	R' (s^{-1})	$\langle I_{\text{beam}} \rangle$ (proj/s)	σ_f (b)
46	5.116×10^4	8.560×10^9	2.326
47	5.672×10^4	8.857×10^9	2.493
51	5.617×10^4	8.340×10^9	2.621
52	4.649×10^4	6.938×10^9	2.608

Table 4.3: Deduced experimental cross-sections for binary fission for the reaction ^{12}C + ^{232}Th at 16 MeV/A.

an electron suppressed F.C. (incident electrons are deflected away from the F.C. and thus the integrated charge is due only to ^{12}C^{6-} nuclei) located upstream from the scattering chamber. The comparison was made for two beam currents differing by a factor of 10, and it was found that a factor of 0.502 was needed to convert the beam current measured at the beam dump to the true beam current as measured at the electron suppressed F.C.

The output from the current integrator was recorded as a scalar for each run representing the total charge collected at the beam dump. The calibrated beam current obtained from the current integrator was then used to determine the binary fission cross section for these four runs by the standard expression

$$\sigma = \frac{R'}{I_{\text{beam}} n x}$$

where $nx = 2.569(\pm 0.130) \times 10^{18}$ target nuclei/cm^2 for the $700\,\mu$g/cm^2 ^{232}Th target foil rotated to $45°$ with respect to the beam axis. In Table 4.3 R' represents the corrected binary fission reaction rate, $\langle I_{\text{beam}} \rangle$ is the average beam current in projectiles per second as determined from the current integrator and duration of each run, and σ_f is the resulting binary fission cross section. The mean value for σ_f weighted by the uncorrected number of binary fission events in each of the four runs was

$$\sigma_f = 2.45 \pm 0.11 \text{ b.}$$

This result is in agreement with the asymptotic value for binary fission excitation functions for the same and similar systems as shown in Fig. 4.15. The binary fission cross section deduced from the last four runs was then used to calculate the average beam current $\langle I_{\text{beam}} \rangle$ for all earlier runs (those for which the current integrator was not present). In Table 4.4 R'_v is the binary fission reaction rate corrected for geometric efficiency, down-scaling and detector/DAQ dead time, $\langle I_{\text{beam}} \rangle$ is the average beam current calculated for each run, and N_{proj} is the corresponding number of projectiles incident on the target during the run.

To simplify the determination of the ternary fission cross section, a weighted average over all runs of interest was calculated for both the average beam current and the time-to-live correction factor. The weighting factors used for both averages was the corrected numbers of binary events, N', for each run.

$$\langle I'_{\text{beam}} \rangle = \frac{\sum N' \langle I_{\text{beam}} \rangle}{\sum N'} = 8.811(\pm 1.102) \times 10^9 \text{ proj./s}$$

$$\langle f_t \rangle = \frac{\sum N' f_t}{\sum N'} = 0.716 \pm 0.078$$

Total time for the runs used was $t = 1.213(\pm 0.011) \times 10^5$ s, assuming an uncertainty of ± 60 s for each run. In Table 4.5, Z_{IMF} represents the atomic number of the ternary fragment, N represents the uncorrected total number of such fragments detected, N' represents the total number of fragments after correction for geometric efficiency effects and detector/DAQ dead-time, R' is the corresponding corrected reaction rate, and σ_{NSE} is the resulting ternary fission cross section in μb. The deduced ternary
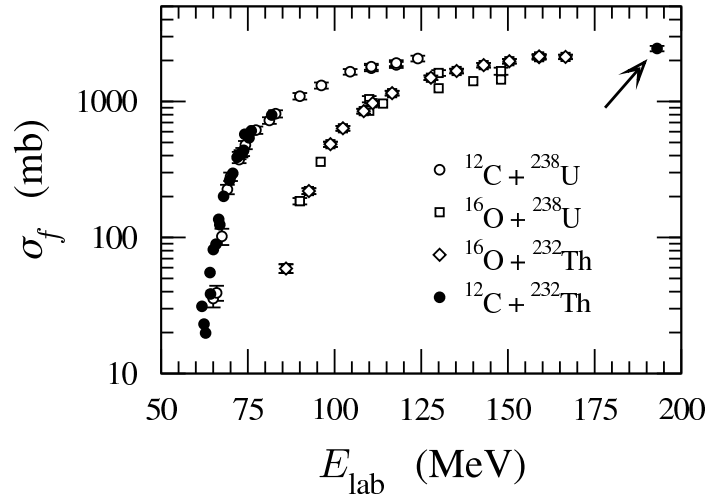
Figure 4.15: Excitation functions for binary fission in the reactions: ^{12}C + ^{238}U [27], ^{16}O + ^{238}U [27, 28], ^{16}O + ^{232}Th [29], and ^{12}C + ^{232}Th [30, 31, 32, 33]. The arrow indicates the point for the binary fission cross-section determined in the current work ($\sigma_f = 2.45 \pm 0.11$ b for incident energy $E_{\text{lab}} = 193$ MeV).

fission cross-sections for fragments with $3 \leq Z_{\text{IMF}} \leq 12$ are presented in Table 4.5 for the reaction ^{12}C + ^{232}Th at 16 MeV/A. A plot of the deduced ternary fission cross-sections as a function of Z_{IMF} of the NSE fragment is provided in Fig. 4.16.

Run #	R' (s^{-1})	$\langle I_{\mathrm{beam}} \rangle$ (proj/s)	N_{proj}
23	5.265×10^4	8.370×10^9	4.520×10^{13}
24	5.298×10^4	8.421×10^9	4.042×10^{12}
26	4.298×10^4	6.831×10^9	5.656×10^{13}
29	6.756×10^4	1.074×10^{10}	2.384×10^{13}
31	6.317×10^4	1.004×10^{10}	1.416×10^{14}
32	5.871×10^4	9.332×10^9	2.368×10^{14}
33	5.581×10^3	8.871×10^8	1.224×10^{12}
36	4.407×10^4	7.005×10^9	1.345×10^{13}
37	6.227×10^4	9.898×10^9	7.424×10^{13}
39	4.660×10^4	7.407×10^9	3.600×10^{13}
41	4.454×10^4	7.079×10^9	1.317×10^{13}
42	5.030×10^4	7.994×10^9	3.502×10^{13}
43	4.924×10^4	7.828×10^9	4.180×10^{13}
44	4.869×10^4	7.740×10^9	4.226×10^{13}
45	9.044×10^3	1.438×10^9	2.329×10^{12}

Table 4.4: Calculated beam currents based on the deduced binary fission rate.

References

[1] T. Sikkeland and V. Viola, in *Proceedings of the Third Conference on Reactions Between Complex Nuclei*, edited by A. Ghiorso, R. Diamond, and H. Conzett (University of California Press, Berkeley, 1963), pp. 232–240.

[2] V. Viola Jr. *et al.*, Phys. Rev. C **26**, 178 (1982).

[3] D. Hilscher *et al.*, Phys. Rev. C **36**, 208 (1987).

[4] E. Mordhorst *et al.*, Phys. Rev. C **43**, 716 (1991).

[5] V. Viola, Nucl. Phys. **A471**, 53c (1987).

[6] M. Fatyga *et al.*, Phys. Rev. C **32**, 1496 (1985).

Z_{IMF}	N	N'	R' (s^{-1})	σ_{NSE} (μb)
3	139	12107.9 ± 1027.0	$1.012(\pm0.966) \times 10^{-1}$	4.40 ± 0.28
4	138	13015.6 ± 1108.0	$1.088(\pm0.093) \times 10^{-1}$	4.74 ± 0.29
5	74	7354.3 ± 854.9	$6.147(\pm1.218) \times 10^{-2}$	2.67 ± 0.22
6	116	12267.7 ± 1139.0	$1.025(\pm0.096) \times 10^{-1}$	4.46 ± 0.28
7	30	3482.2 ± 635.8	$2.910(\pm1.743) \times 10^{-2}$	1.27 ± 0.15
8	34	4067.7 ± 697.6	$3.400(\pm1.616) \times 10^{-2}$	1.48 ± 0.16
9	19	2012.5 ± 461.7	$1.682(\pm2.279) \times 10^{-2}$	0.74 ± 0.11
10	20	2253.5 ± 503.9	$1.884(\pm2.156) \times 10^{-2}$	0.82 ± 0.12
11	22	2282.5 ± 486.6	$1.907(\pm2.142) \times 10^{-2}$	0.84 ± 0.12
12	13	1473.9 ± 408.8	$1.232(\pm2.657) \times 10^{-2}$	0.54 ± 0.10

Table 4.5: Experimental cross-sections for near-scission emission as a function of Z_{IMF} of the ternary particle for the reaction ^{12}C + ^{232}Th at 16 MeV/A.

[7] M. Fatyga *et al.*, Phys. Rev. C **35**, 568 (1987).

[8] V. Viola, Nucl. Phys. **A502**, 531c (1989).

[9] W. Skulski *et al.*, Phys. Rev. C **40**, 1279 (1989).

[10] D. Fields *et al.*, Phys. Rev. Lett. **69**, 3713 (1992).

[11] S. Chen *et al.*, Phys. Rev. C **54**, 2114 (1996).

[12] J. Hufner, Phys. Rep. **125**, 129 (1985).

[13] W. Trautmann, U. Milkau, U. Lynen, and J. Pochodzalla, Z. Phys. **A344**, 447 (1993).

[14] M. McMahan *et al.*, Phys. Rev. Lett. **54**, 1995 (1985).

[15] D. Durand (unpublished).

[16] M. Marsili and Y. Zhang, Phys. Rev. Lett. **77**, 3577 (1996).
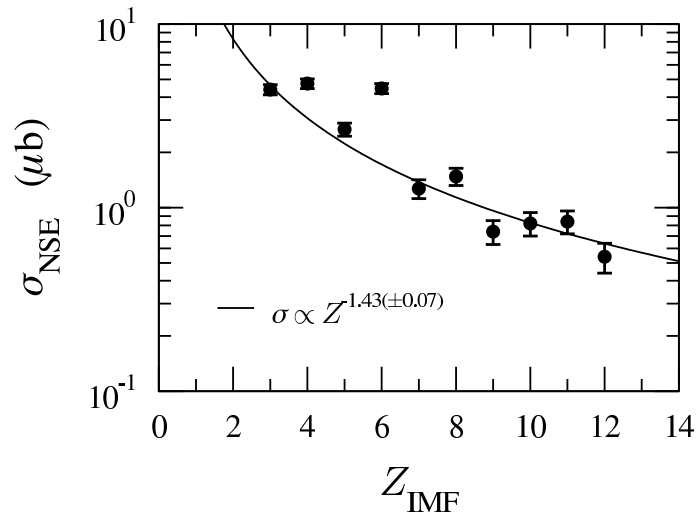
Figure 4.16: Experimental cross-sections for near-scission emission as a function of Z_{IMF} of the ternary particle for the reaction ^{12}C + ^{232}Th at 16 MeV/A.

[17] Y. Gazit, E. Nardi, and S. Katcoff, Phys. Rev. C **1**, 2101 (1970).

[18] W. Baum, Ph.D. thesis, Technische Hochschule Darmstadt, 1992.

[19] M. Wöstheinrich *et al.*, Acta. Phys. Slovaca **49**, 117 (1999).

[20] N. Cârjan, A. Sierk, and J. Nix, Nucl. Phys. **A452**, 381 (1986).

[21] N. Cârjan (private communication).

[22] L. Moretto, D. Breus, L. Phair, and G. Wozniak, Phys. Rev. Lett. **85**, 2645 (2000).

[23] R. Yanez *et al.*, Phys. Rev. Lett. **85**, 2646 (2000).

[24] M. Zielinska-Pfabe and K. Dietrich, Phys. Lett. **B49**, 123 (1974).

[25] R. Vandenbosch, Nucl. Phys. **A502**, 1c (1989).

[26] R. de Souza and N. Cârjan, to be submitted to Phys. Rev. C .

[27] V. Viola, Jr. and T. Sikkeland, Phys. Rev. **130**, 2044 (1963).

[28] B. Back *et al.*, Phys. Rev. C **32**, 195 (1985).

[29] T. Murakami *et al.*, Phys. Rev. C **34**, 1353 (1986).

[30] V. Ramamurthy *et al.*, Phys. Rev. C **65**, 25 (1990).

[31] A. Karnik *et al.*, Z. Phys. **A351**, 195 (1995).

[32] N. Majumdar *et al.*, Phys. Rev. C **53**, R544 (1996).

[33] J. Lestone, A. Sonzongi, M. Kelly, and D. Prindle, Phys. Rev. C **55**, R16 (1997).

Chapter 5

Comparison with Model Calculations

Three models were employed in an attempt to gain additional insight into the salient features of ternary fission:

1. SIMON statistical decay code: Used to calculate elemental yields of ternary fragments assuming sequential decay, i.e. IMF emission followed by fission, within a statistical model framework [1].

2. Fission energetics code: Used to investigate the potential energy for various ternary scission configurations relative to a spherical parent, assuming a particular size of ternary fragment. The calculations included contributions from the nuclear binding energies, the Coulomb energy, and the proximity energy (details of the proximity energy calculation are provided in Appendix D). Nuclear binding energies were calculated using the Droplet Model of Myers and Swiatecki [2, 3, 4] (details of the model are provided in Appendix E).

3. Los Alamos Dynamical Fission Model: Used to explore the effects of angular momentum, isospin (N/Z), and kinetic energy along the deformation coordinate in ternary fission.
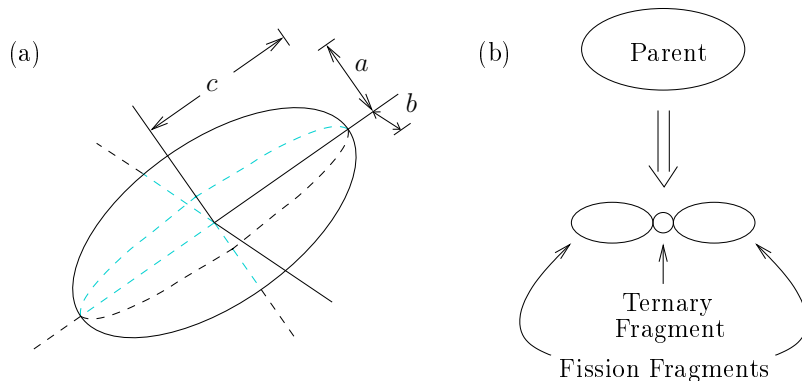
Figure 5.1: (a) A prolate spheroid of rotation ($a = b < c$) with semi-major axis, c, and semi-minor axes, a and b, labeled. The spheroid depicted has an axis ratio of $c/a = 2/1$ ($\varepsilon = 0.866$). (b) Diagram of the initial state (parent) and final state (ternary fragment plus two identical fission fragments) configurations used in the fission barrier calculations. In this diagram the parent and fission fragments each have an axis ratio of $2/1$, while the ternary fragment is spherical.

The IMF yields calculated with SIMON were compared directly to the experimentally measured yields of IMFs emitted isotropically and near-scission. The results of these statistical calculations were previously described in Secs. 4.4 and 4.5. The energetics calculations and dynamical model simulations are the focus of the remainder of this chapter.

5.1   Energetics of Ternary Fission

Calculations were performed in an attempt to estimate the magnitude of various contributions to the energetics of ternary fission, and how those contributions varied with the deformation of one or more of the fragments. The procedure calculated the change in energy between an initial state consisting of a heavy parent nucleus and a collinear three-body final state consisting of two identical fission fragments (FF) separated by a smaller ternary fragment (TF). Deformation of any fragment
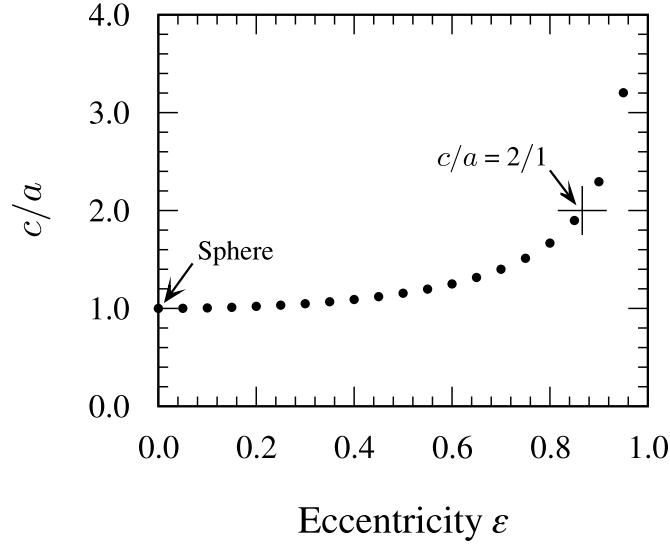
Figure 5.2: Ratio of semi-major to semi-minor axes (c/a) of a prolate spheroid as a function of the eccentricity ε . The cross-hair marks the eccentricity which results in an axis ratio of $2/1$.

---

was parametrized by its eccentricity, ε, defined as

$$\varepsilon = \left[1 - \left(\frac{a}{c}\right)^2\right]^{1/2} \tag{5.1}$$

where the quantity a/c is the ratio of the semi-minor to semi-major axes, a and c respectively, of a prolate spheroid as shown in panel (a) of Fig. 5.1. Only spheres $(a = b = c)$ and prolate spheroids $(a = b < c)$ were considered, allowing a range in eccentricity of $0.0 \leq \varepsilon < 1.0$. The dependence of the axis ratio, c/a, on ε is shown in Fig. 5.2. The three collinear fragments of the final state were assumed to be aligned along their semi-major axes as shown in panel (b) of Fig. 5.1.

In all of the calculations, the mass and charge, A_{FF} and Z_{FF}, respectively, of each fission fragment was calculated as:

$$A_{\mathrm{FF}} = \frac{1}{2}\left(A_{\mathrm{Parent}} - A_{\mathrm{TF}}\right) \qquad \text{and} \qquad Z_{\mathrm{FF}} = \frac{1}{2}\left(Z_{\mathrm{Parent}} - Z_{\mathrm{TF}}\right).$$

Half-integer values were allowed for both A_{FF} and Z_{FF}. Furthermore, the assumption

of incompressibility was applied by forcing the volume of a spheroidal fragment to be equal to that of a spherical fragment with identical A:

$$V = \tfrac{4}{3}\pi r^3 \qquad\qquad \text{for a sphere} \tag{5.2}$$

$$V = \tfrac{4}{3}\pi\sqrt{1-\varepsilon^2}\,c^3 \qquad\qquad \text{for a prolate spheroid.} \tag{5.3}$$

The radius used to calculate the volume in Eq. 5.2 is defined as $r = r_0 A^{1/3}$, with $r_0 = 1.18$ fm. Setting the right side of Eq. 5.3 equal to the volume calculated for the case of a spherical nucleus and solving for c gives

$$c = \left[\frac{3\,V_{\text{sph}}}{4\pi\sqrt{1-\varepsilon^2}}\right]^{1/3} \tag{5.4}$$

where c is the semi-major axis of the prolate spheroid with volume equal to that of the equivalent sphere, V_{sph}. Of course, for the case $\varepsilon = 0.0$ (a sphere) Eq. 5.4 gives the result $c = r$ as expected.

The total energy of a particular state (either initial or final) was calculated as the sum of three contributing energies: fragment-fragment Coulomb repulsion, surface proximity energy, and individual fragment binding energies. Since the initial state consists of just the parent nucleus, the initial Coulomb and proximity energies are both zero and the total energy is determined by the binding energy of the parent nucleus. Figure 5.3 shows a simple schematic of a one-dimensional fission barrier as a function of an arbitrary parameter ζ along the deformation coordinate. The energy change ΔE between the initial and final states is indicated in this figure. The following calculations assume an initial state consisting of a spherical parent nucleus in its ground state. These calculations provide no information about the saddle-point shape or the energy associated with it. If the decision to proceed to fission were determined exclusively at the saddle point, these calculations would provide no insight into the process. In reality, however, fission is a dynamical process with at least some degrees of freedom determined between saddle and scission. From this perspective, the following calculations can be instructive.
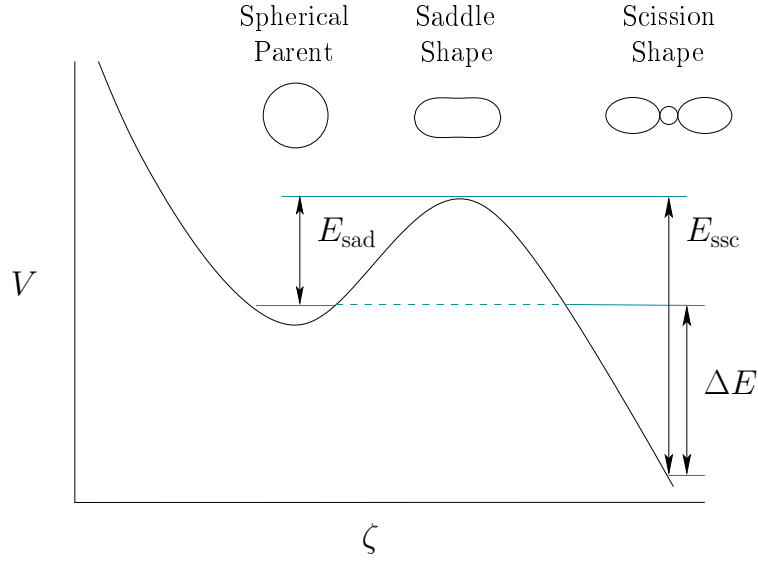
Figure 5.3: Simple schematic of a one dimensional fission barrier as a function of an arbitrary parameter ζ along the deformation coordinate. The initial state in the barrier calculations corresponds to a spherical parent nucleus in the ground state. The height of the barrier relative to the ground state is labelled E_{sad} and the saddle to scission energy is labelled E_{ssc}. The quantity calculated in the current work is labelled ΔE.

5.1.1 Final State Coulomb Energy

The Coulomb repulsion energy was treated by approximating each of the three fragments in the final state as a point charge. The distance between charge centers was chosen to be equal to the sum of the lengths of the semi-major axes between adjacent charge pairs, i.e. the fragments were assumed to be touching prolate spheroids. This lead to the following expression for the total Coulomb repulsion energy,

$$E_{\text{Coul}}^{final} = \left(2\, \frac{1.44 \cdot Z_{\text{TF}} Z_{\text{FF}}}{r_{\text{TF}-\text{FF}}} + \frac{1.44 \cdot Z_{\text{FF}}^2}{r_{\text{FF}-\text{FF}}} \right) \text{ MeV}, \tag{5.5}$$

where Z_{TF} and Z_{FF} are the atomic numbers of the ternary fragment and fission fragments, respectively, $r_{\text{TF}-\text{FF}}$ is the distance between the charge centers of the

ternary fragment and one fission fragment, and $r_{\mathrm{FF-FF}}$ is the distance between the charge centers of the two fission fragments.

5.1.2 Final State Proximity Energy and Droplet Model Binding Energies

The final state in the current calculations consists of three fragments in close proximity. The attractive force between two adjacent nuclear surfaces gives rise to a proximity energy that is dependent on the size of the gap between the surfaces. Blocki *et. al.* [5] developed a method of determining the proximity energy between two spheres as a product of a geometrical factor and a universal function describing the separation between the two surfaces, both of which are characteristic of the material composing the objects and related to the surface energy coefficient. The method was later extended by Malhotra and Gupta to include non-spherical shapes [6]. Details of the proximity energy calculation are provided in Appendix D. The binding energy of each fragment was calculated using the Droplet Model (DM) expressions derived by Myers and Swiatecki [2, 3, 4]. Details of these calculations are provided in Appendix E.

5.1.3 Calculating the Fission Energetics

The energy change between the *initial* and *final* states was calculated as follows:

$$\Delta E = E^{final} - E^{initial} = E^{final}_{\mathrm{DM}} + E^{final}_{\mathrm{Coul}} + E^{final}_{\mathrm{Prox}} - E^{initial}_{\mathrm{DM}}, \tag{5.6}$$

where ΔE is the calculated energy change, E_{DM} is the total Droplet model binding energy for the indicated state, $E^{final}_{\mathrm{Coul}}$ is the total Coulomb repulsion energy of the *final* state and $E^{final}_{\mathrm{Prox}}$ is the total surface proximity energy of the *final* state. The three final state quantities are summed over all three fragments of the final state; i.e. E^{final}_{DM} is the sum of the Droplet model binding energies of the three fragments in the final state.

Figure 5.4 contains plots resulting from the energetics calculations for four different ternary fragments, ^{7}Li (solid lines), ^{14}C (dotted lines), ^{20}F (dashed lines) and

^{26}Mg (dot-dashed lines). In each case ^{244}Cm was used as the parent nucleus with no deformation ($\varepsilon_{\text{Parent}} = 0.0$). Panels (a)–(d) show the dependence of the energy change and its components as a function of the eccentricity of the ternary fragment assuming spherical fission fragments. Panels (e)–(h) are plots of the same quantities as a function of the eccentricity of the two fission fragments assuming a spherical ternary fragment. Panels (a) and (e) show the energy change, ΔE, as a function of the deformation of the ternary fragment (TF) and fission fragments (FF), respectively. The remaining panels show plots of the three energy components appearing on the right side of Eq. 5.6, with $\Delta E_{\text{DM}} = E_{\text{DM}}^{final} - E_{\text{DM}}^{initial}$ being the change in the total Droplet model binding energy.

We look first at the case $\varepsilon_{\text{TF}} = \varepsilon_{\text{TF}} = 0.0$, i.e. three collinear spheres. The change in the Droplet model binding energy, shown in panels (d) and (h), decreases with increasing size of the ternary fragment. This result is expected from simple energetics arguments - the magnitude of the nuclear binding energy is a maximum for fragments near ^{56}Fe, and decreases for lighter and heavier fragments. Therefore, the final state should become more bound (decreasing ΔE_{DM}) as the size of the ternary fragment is increased. Because the parent nucleus is the same for all cases, as the size of the ternary fragment is increased, the size of the two fission fragments is decreased, also leading to an increase in the final state binding energy.

Panels (c) and (g) show the total Coulomb repulsion energy for the final state configuration. For the case of three collinear spheres the total Coulomb repulsion increases with the atomic number of the ternary fragment. This result can be understood by looking at how the Coulomb energy is calculated in Eq. 5.5. An increase in Z_{TF} will have a much larger effect on E_{Coul}^{final} than the corresponding decrease in Z_{FF}. For increasing Z_{TF} the ternary fragment – fission fragment Coulomb repulsion increases more rapidly than the fission fragment – fission fragment Coulomb repulsion decreases. This trend can be seen in Fig. 5.5, which shows the two terms of Eq. 5.5 plotted separately. A linear fit was made to each set in Fig. 5.5 to provide an estimate of the relative effect of the two terms. The resulting slopes, m, are listed in
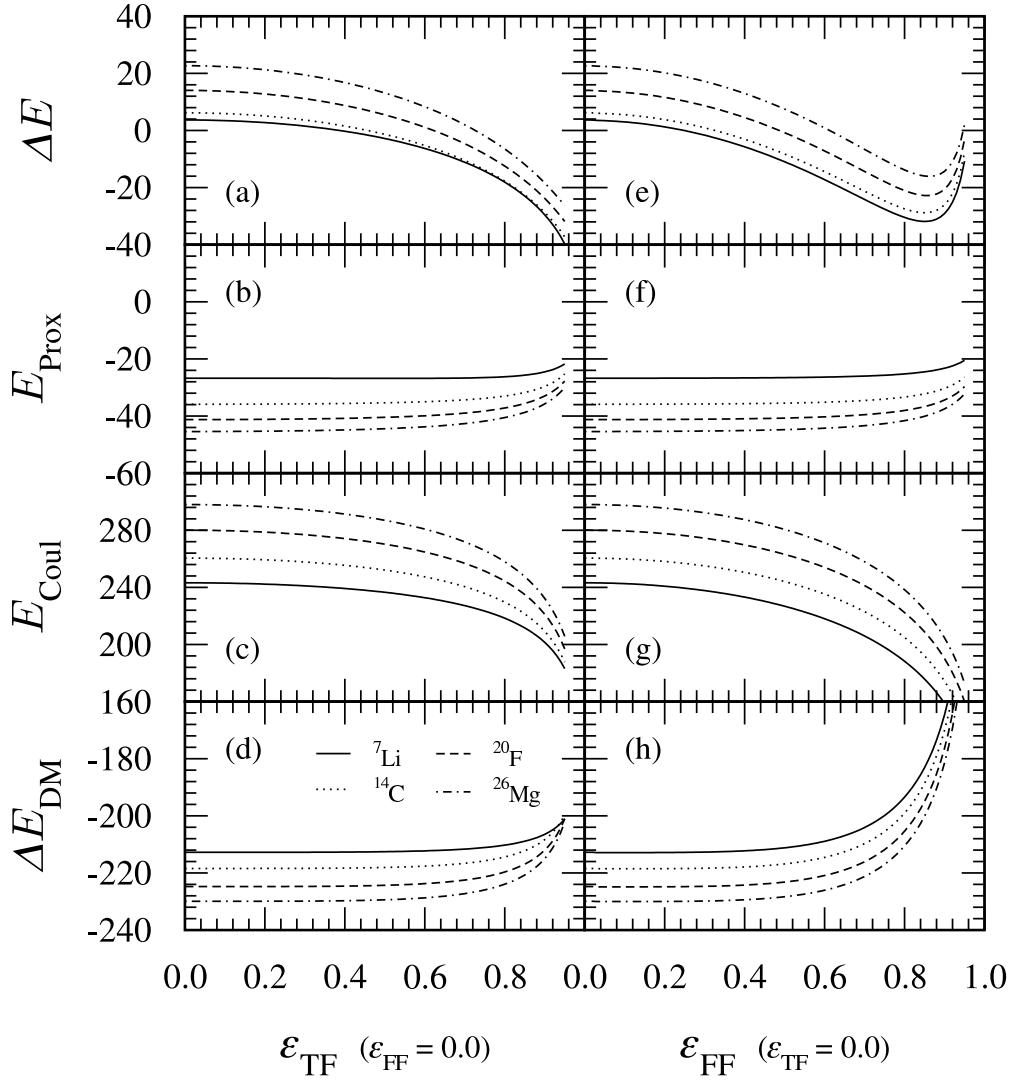
Figure 5.4: Calculated energy change, ΔE, for the cases where the ternary fragment is ^{7}Li (solid lines), ^{14}C (dotted lines), ^{20}F (dashed lines) and ^{26}Mg (dot-dashed lines), along with plots of the three energy components. All energies are in MeV.
Note - the energy range for E_{Coul} is twice that of the other plots.
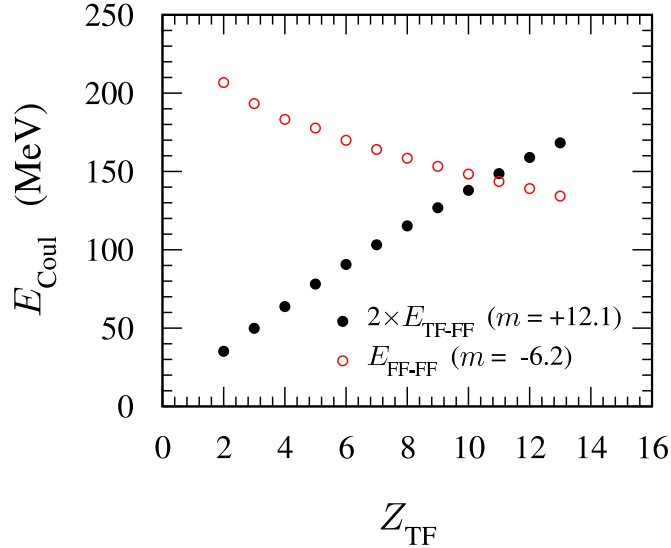
Figure 5.5: Variation of the contributions to the Coulomb energy with the size of the ternary fragment. The two terms in Eq. 5.5 are plotted separately. The first term is twice the Coulomb repulsion between the ternary fragment and one fission fragment, $E_{\text{TF-FF}}$, indicated by the filled circles. The second term is the Coulomb repulsion between the two fission fragments, $E_{\text{FF-FF}}$, indicated by the open circles. A linear fit was applied to each set, and the resulting slopes, m, are listed in the legend.

the figure legend. As expected, the variation in the first term dominates the overall variation in the total Coulomb repulsion energy.

In panels (b) and (f) of Fig/ /reffig:DM-comp we note that the magnitude of the (attractive) proximity energy E_{Prox} increases with increasing mass of the ternary fragment. Since the proximity energy is in part a function of the surface area of the two adjacent fragments, we expect that the increased surface area associated with a larger ternary fragment will lead to a larger (more negative) proximity energy. Also, since the surface area goes roughly as $r^2 = r_0^2 A^{2/3}$ for spherical nuclei, we expect that the increase in surface area of the smaller, ternary fragment will have a larger
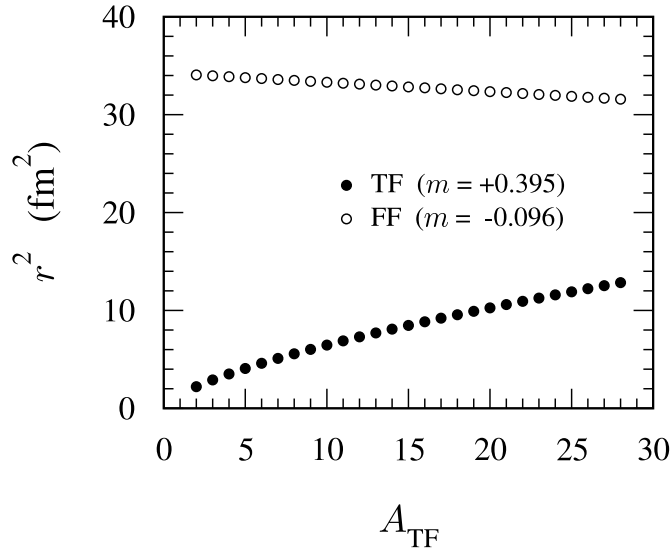
Figure 5.6: Variation of the radius squared with fragment mass A assuming the relation $r^2 = r_0^2 A^{2/3}$, for the ternary fragment (closed circles) and fission fragments (open circles) as a function of the mass of the ternary fragment. A linear fit was applied to each set, and the resulting slopes, m, are listed in the legend.

effect on the proximity energy than the corresponding decrease in surface area of the two fission fragments, each of which loses half the number of nucleons added to the ternary fragment. The effect on r^2 is shown in Fig. 5.6 for both the ternary and fission fragments. Again, a linear fit was applied to both sets to estimate the relative effect, with the resulting slopes, m, listed in the legend. Clearly the variation of the proximity energy is dominated by the variation in the mass of the ternary fragment, with heavier ternary fragments leading to larger (negative) proximity energies.

The net effect of the three components of the energetics calculation can be seen in panels (a) and (e) of Fig. 5.4. For the case of three collinear spheres ($\varepsilon_{TF} = \varepsilon_{FF} = 0.0$) the energy change increases with increasing mass of the ternary fragment. This trend continues when we consider deformations of either the ternary fragment in panel (a), and the two fission fragments in panel (e). A notable difference

between the two plots only occurs for the most deformed fragments (TF or FF). For the case of extremely deformed ternary fragments, the energy change is a continuously decreasing function of the deformation $\varepsilon_{\mathrm{TF}}$. However, in the case of extremely deformed fission fragments a minimum occurs at $\varepsilon_{\mathrm{FF}} \simeq 0.85$, after which the barrier begins to increase. This increase for extreme deformations of the fission fragments can be seen as a result of the rapid increase in the net Droplet Model binding energy shown in panel (h) (extremely deformed fragments are less tightly bound), which begins to outweigh the contribution from the decreasing Coulomb component shown in panel (g). Although the increase in the binding energy also occurs for deformation of the ternary fragment, shown in panel (d), it is much more gradual, and does not out-pace the decrease in the Coulomb repulsion shown in panel (c).

The Coulomb energy of the final state as a function of the deformation of the ternary and fission fragments is shown in panels (c) and (g) respectively. We see that the Coulomb energy is a decreasing function of the eccentricity of either the ternary or fission fragments. This trend is the result of the increasing separation between charge centers for more deformed shapes (remember that in our rather simplistic picture of the final state the fragment separation is the sum of the semi-major axes of the two adjacent fragments). The effect is greater for deformations of the fission fragments as they lead to larger changes in the inter-fragment separation.

The above observations for the effects of deformations imposed on the ternary and fission fragments can be summed up by considering the relative sizes of the two fragment types. For the Coulomb repulsion, a fixed deformation of the ternary fragment cannot cause the same degree of separation of the charge centers as an identical deformation of the fission fragments. Size can also be used to explain the greater effect on the net binding energy for the case of deformed fission fragments compared to a deformed ternary fragment. Each shape-dependent term in the Droplet Model binding energy expression is a function of A and/or Z for the fragment in question (see Appendix E). Thus it would be expected that a larger fragment would experience comparably larger effects from a variation in the deformation.

^{14}C

PSfrag replacements

Mg

^{26}Mg

PSfrag replacements

C
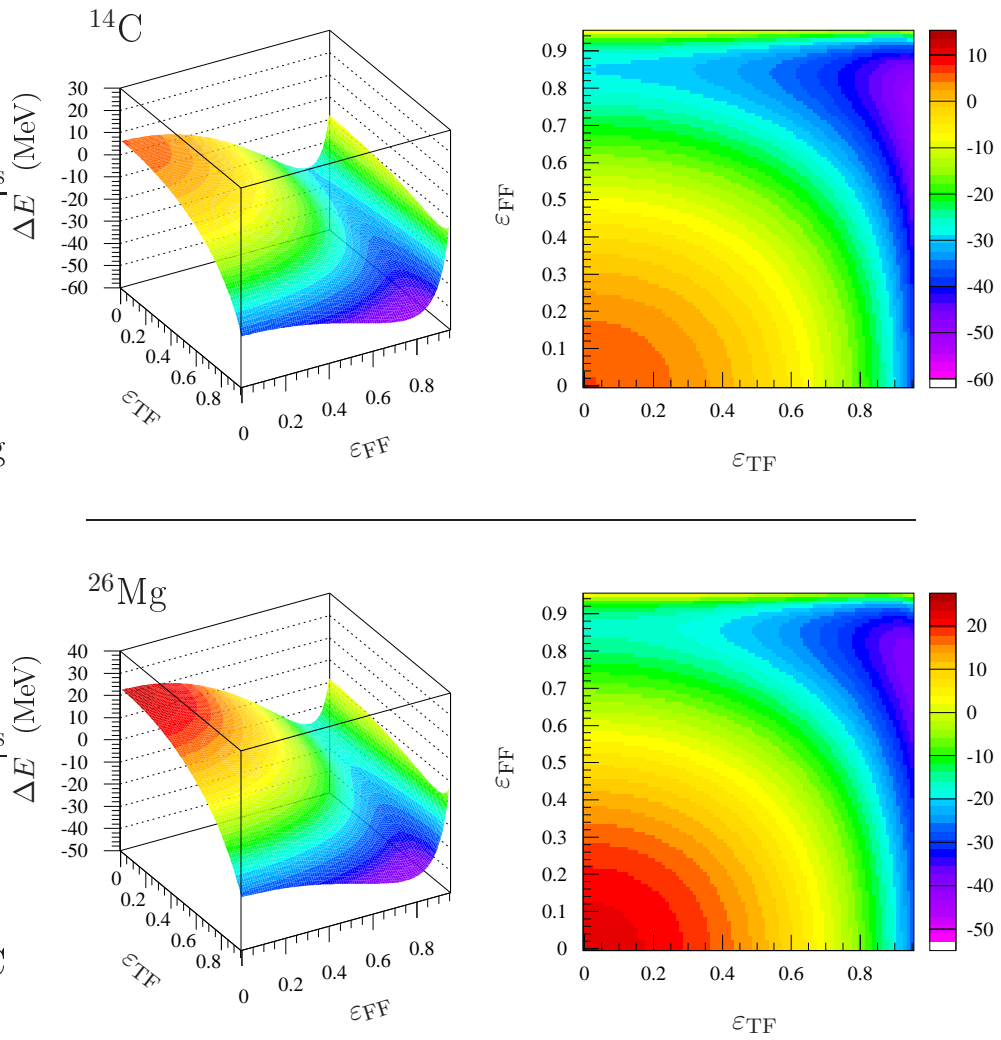
Figure 5.7: Energy change, ΔE, for ^{14}C and ^{26}Mg, as a function of the eccentricities of the ternary (TF) and fission (FF) fragments.

Next we consider simultaneous variations in the deformations of the ternary and fission fragments. Figure 5.7 contains surface and contour plots of the energy change, ΔE, as calculated for the the two cases in which the ternary fragment is either ^{14}C or ^{26}Mg. In each case ΔE is plotted as a function of both ε_{TF} and ε_{FF}. In our definition of ΔE, a negative result indicates an exoergic process, while a positive result would indicate an endoergic process. Since we know that fission of heavy nuclei is an exoergic process, we will focus on those regions of the energy surface where $\Delta E < 0$. An examination of the two energy surfaces presented in Fig. 5.7 reveals that they are remarkably similar in overall shape. The only real difference is that the surface for ^{26}Mg is shifted up in energy relative to the surface for ^{14}C. This is a general trend observed for all cases investigated with ternary fragments ranging from ^{4}He to ^{29}Al. For both cases it is clear that more extended final states (larger values of the eccentricity) are favored. If we make the assumption that ternary fission will only occur for final state configurations in which $\Delta E < 0$ the follow conclusions can be made:

1. In general, ternary fission will only occur for more extended scission configurations.

2. Larger ternary fragments will be limited to more extended scission configurations than smaller ternary fragments.

Item 2 is consistent with conclusions drawn from an examination of the relative experimental yields as discussed in Sec. 4.5.

Due to the rather crude nature of these calculations, the results should be considered qualitative at best. Suggestions have recently been made to improve these calculations [7], such as the use of a more realistic interaction energy in the final state, e.g. to use the real Coulomb energy of diffuse shapes plus an attractive Yukawa-plus-exponential energy instead of the point charge Coulomb energy plus proximity energy approximations.

5.2   Dynamical Model Simulations

In order to investigate our expectations of the influence of angular momentum, isospin (N/Z), and kinetic deformation (stretching) on the ternary fission probability, we utilized the Los Alamos dynamical model of fission [8, 9]. This model was used to simulate the dynamical evolution of the system in the multi-dimensional deformation space as the fissioning system proceeded from saddle to scission. Special emphasis was put on the onset of ternary fission.

Calculations were performed for two dissipation mechanisms: two-body viscosity (responsible for dissipation in ordinary fluids) and one-body surface dissipation (arising from collision of nucleons with the moving nuclear surface, and when there is a neck between the binary reaction partners, also transfer of nucleons through it). These two dissipation mechanisms represent not only opposite extremes of small and large magnitude, respectively, but also dissipations with very different tensorial properties. In order to estimate the impact of neutron emission prior to the system reaching the saddle, the fission of ^{216}U was calculated in addition to ^{236}U.

Three different situations were investigated:

1. Compound nuclei at their saddle point with angular momenta from $\ell = 0$ to $\ell = \ell_{max}$; the value of the fission barrier vanishes at about $70\hbar$ for ^{236}U and $60\hbar$ for ^{216}U.

2. Nearly spherical systems with angular momenta greater than ℓ_{max}, representing fast fission events.

3. Deformed non-rotating systems with large kinetic energies in the fission degree-of-freedom, imitating the incomplete transfer of orbital angular momentum into rigid rotation, the difference going into deformation of the composite system along the direction of the projectile impact.

In reality, of course, effects 2 and 3 above co-exist. The initial angular momentum in the deformation space was chosen to correspond to the most probable trajectory. The

results are therefore only suitable for comparison with data that represent the most probable decay channel. Nevertheless, these calculations are useful for qualitatively illustrating dependencies on angular momentum, N/Z, and stretching.

Figs. 5.8 and 5.9 depict the effect of angular momentum on the time evolution of nuclear shapes from saddle to scission for ^{236}U and ^{216}U respectively. The numbers in the upper right corner of each panel indicate the time in units of 1 x 10^{-22} sec. Two-body dissipation with a viscosity coefficient $\mu = 0.02$ TP was used. One can clearly see that in all cases a third light fragment forms between the two heavy fragments. The size (mass) of this fragment increases with angular momentum and is larger for ^{216}U than for^{236}U reflecting an increase in fissility (0.697 *vs.* 0.684).

One can likewise notice that the saddle-to-scission time also varies with angular momentum attaining a maximum at $\ell = \ell_{max}$ and that it is slightly shorter for ^{216}U. The elongation at scission turns out to be the same for the two nuclei but the saddle to scission descent for ^{216}U is steeper than for ^{236}U. This difference leads to higher pre-scission dissipation and kinetic energy and consequently a shorter time scale.

The corresponding time evolution of nuclear shapes obtained with one-body surface dissipation is presented in Figs. 5.10 and 5.11. Although the time scale is now longer, the configurations are more compact and therefore no longer lead to ternary divisions. Based upon our calculations, with this type of dissipation only the highly rotating (120$\hbar$), extremely neutron-deficient ^{176}U would result in ternary fission as the average behavior.

Finally, the consequence of having a large amount of initial kinetic energy along the fission eigenvector was explored. Such a situation may occur when a significant fraction of the incident energy is neither immediately dissipated nor converted into rigid rotation but instead deforms the system along the direction of the projectile motion. This motion will be largely converted into motion along the scission axis. Shown in Fig. 5.12 are the results for two-body dissipation and $\ell = 0$. The ability of the system to attain even larger middle fragments than previously calculated is remarkable. For the case of two-body dissipation a large kinetic energy along the

fission direction is indeed an efficient means to produce ternary fragmentations. In contrast for the case of one-body dissipation the initial kinetic energy is quickly damped into intrinsic excitation. For this case therefore, initial stretching does not result in an increased ternary probability.

A summary of our calculations is provided in Fig. 5.13. In this figure, the influence of angular momentum or initial kinetic energy on the size of the middle fragment, the distance between the two fission fragments, and the total kinetic energy is depicted for the case of two-body dissipation. As the angular momentum increases (panels a–c), all three quantities increase. For $\ell \leq \ell_{max}$, the increase is gradual in contrast to the increase for angular momenta above the rotating-liquid-drop limit. The neutron-deficient nucleus ^{216}U exhibits a slight increase in the mass of the middle fragment as compared to ^{236}U. The behavior of the size of the middle fragment, the fission fragment separation distance, and the total kinetic energy on the initial kinetic energy is relatively linear. The magnitude of the two-body coefficient has a modest effect on the size of the middle fragment while providing little change in the fission-fragment separation distance.
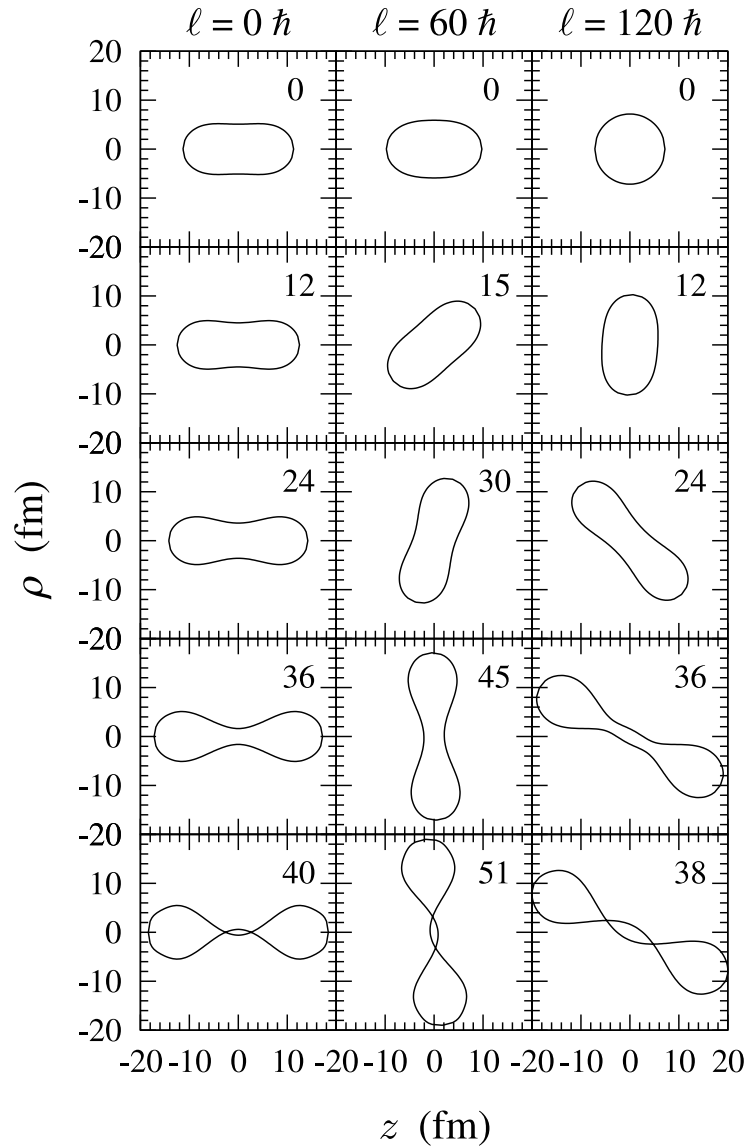
Figure 5.8: Saddle-to-scission shapes calculated with the Los Alamos dynamical fission model for ^{236}U with $\ell_{\text{init}} = 0$, 60, and 120 $\hbar$ assuming two-body dissipation with $\mu = 0.02$ TP.
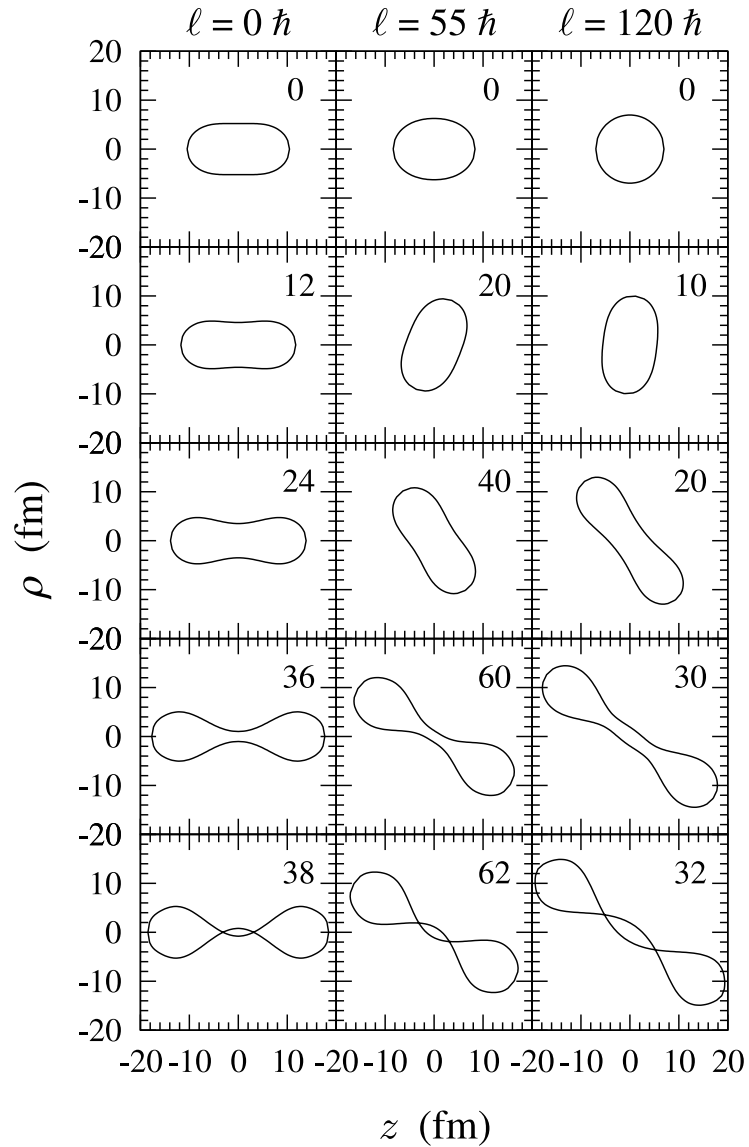
Figure 5.9: Saddle-to-scission shapes calculated with the Los Alamos dynamical fission model for ^{216}U with $\ell_{\text{init}} = 0$, 55, and 120 $\hbar$ assuming two-body dissipation with $\mu = 0.02$ TP.
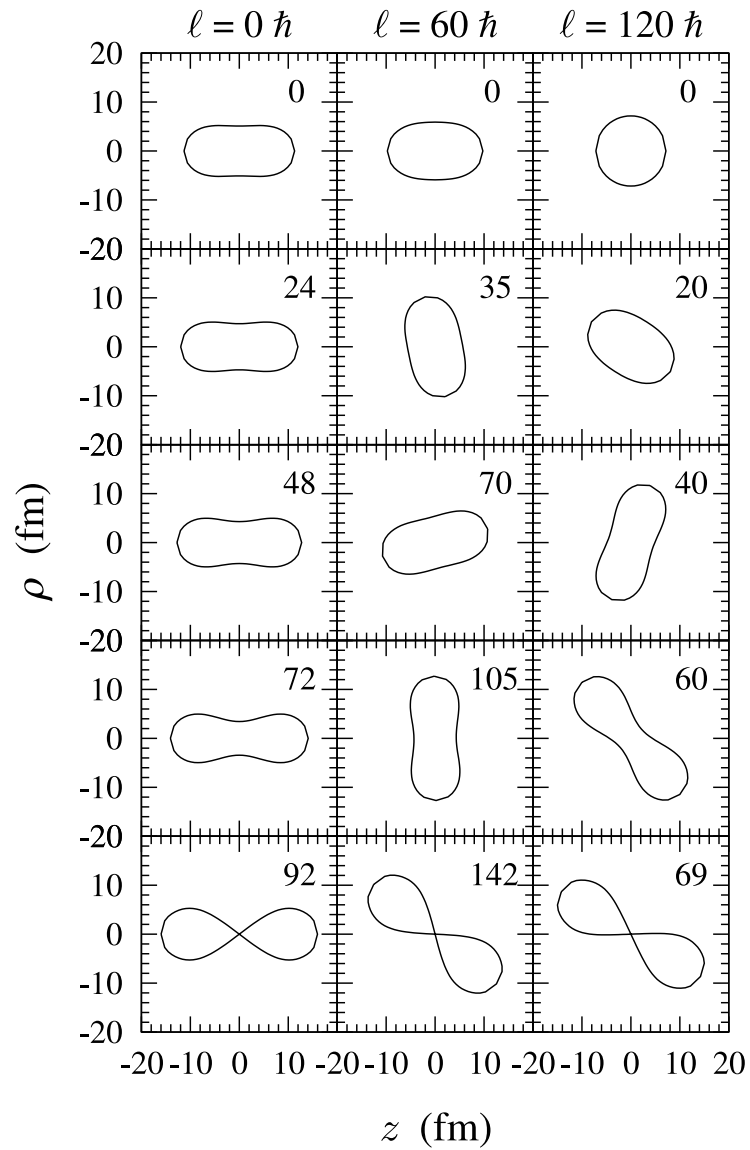
Figure 5.10: Saddle-to-scission shapes calculated with the Los Alamos dynamical fission model for ^{236}U with $\ell_{init} = 0$, 60, and 120 $\hbar$ assuming one-body dissipation.
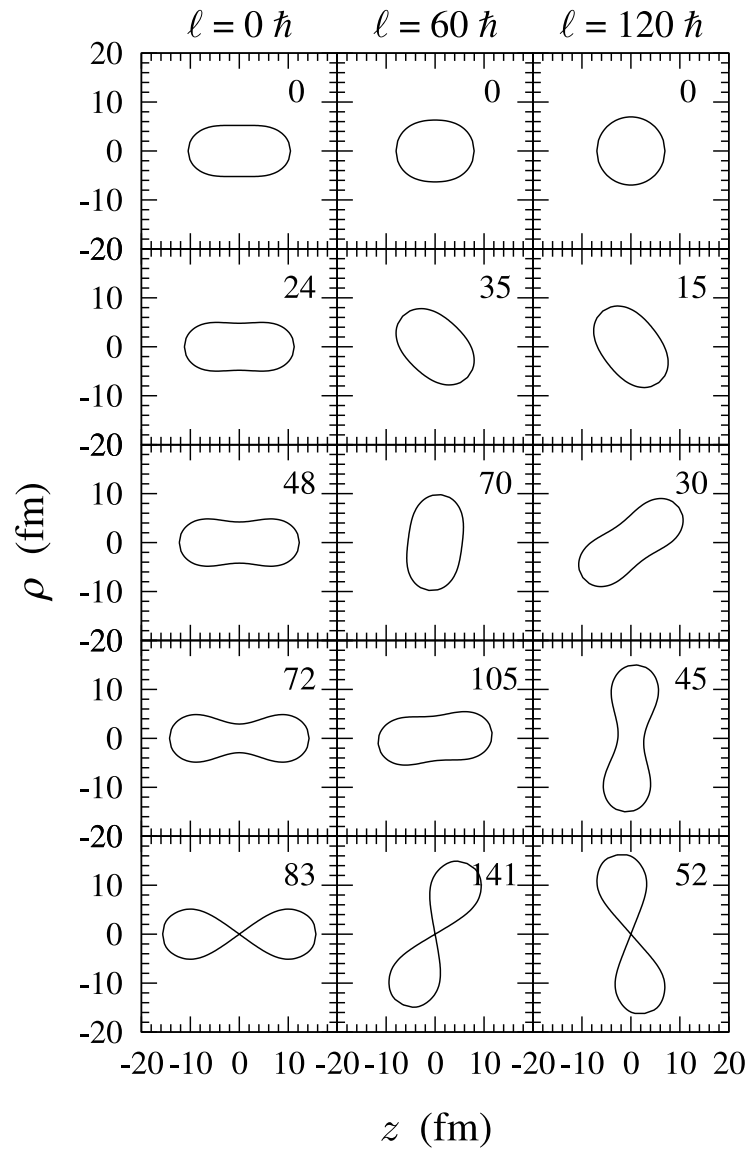
Figure 5.11: Saddle-to-scission shapes calculated with the Los Alamos dynamical fission model for ^{216}U with $\ell_{init} = 0$, 60, and 120 $\hbar$ assuming one-body dissipation.
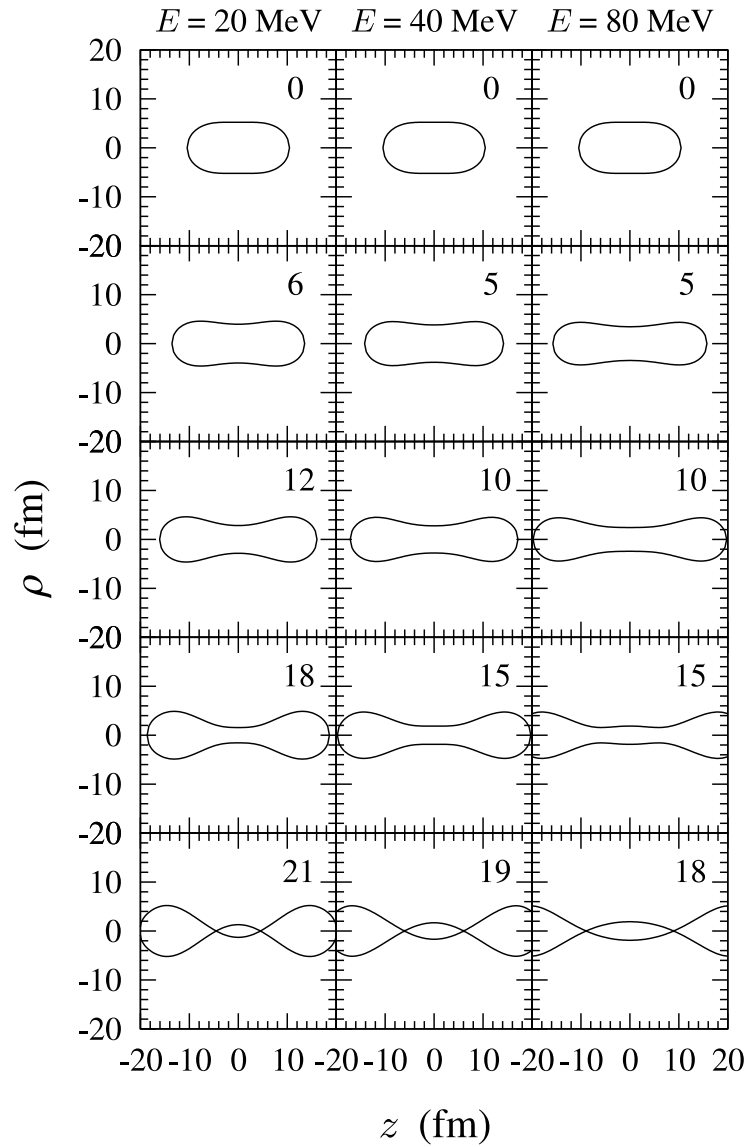
Figure 5.12: Saddle-to-scission shapes calculated with the Los Alamos dynamical fission model for ^{216}U with $E_{\mathrm{init}} = 20$, 40, and 80 MeV for two-body dissipation with $\mu = 0.02$ TP.
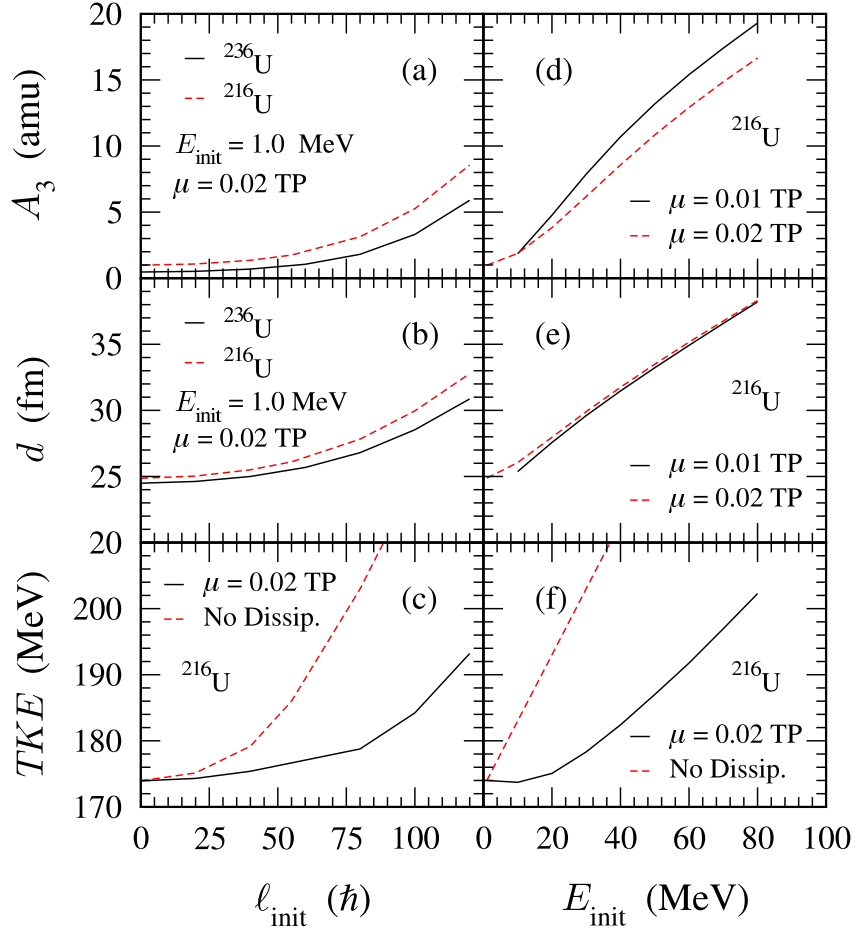
Figure 5.13: Summary of the Los Alamos dynamical fission model calculations assuming two-body dissipation. Panels (a) and (d) show the mass of the ternary fragment, A_3, as a function of the initial angular momentum of the system, ℓ_{init}, and initial kinetic energy along the scission direction, E_{init}, respectively. Panels (b) and (e) show the separation distance d between the two fission fragments at scission as a function of the two initial conditions ℓ_{init} and E_{init} respectively. Panels (c) and (f) are plots of the total kinetic energy (*TKE*) of the two fission fragments at infinity for the initial conditions ℓ_{init} and E_{init} respectively.

References

[1] D. Durand (unpublished).

[2] W. Myers and W. Swiatecki, Nucl. Phys. **81**, 1 (1966).

[3] W. Myers and W. Swiatecki, Ann. Phys. **55**, 395 (1969).

[4] W. Myers and W. Swiatecki, Ann. Phys. **84**, 186 (1974).

[5] J. Blocki, J. Randrup, W. Swiatecki, and C. Tsang, Ann. Phys. **105**, 427 (1977).

[6] N. Malhotra and R. K. Gupta, Phys. Rev. C **31**, 1179 (1985).

[7] A. Sierk (private communication).

[8] N. Cârjan, A. Sierk, and J. Nix, Nucl. Phys. **A452**, 381 (1986).

[9] N. Cârjan (private communication).

Chapter 6

Conclusions

The characteristics of intermediate-mass-fragment (IMF) emission in coincidence with two correlated fission fragments have been studied for the reaction ^{12}C + ^{232}Th at incident energies of $E/A = 16$ and 22 MeV. We focused our investigation on the yields of ternary fragments, their kinetic energies, and their angular distributions with respect the the scission axis. Based upon the measured IMF kinetic energies and angular distributions, we have isolated IMFs emitted near the moment of scission (near-scission emission) from those emitted at an earlier stage, while the composite system is still in a compact state. Ternary events were compared to binary events on the basis of the folding angle measured between the two correlated fission fragments. From the measured folding angle, the fractional linear momentum transfer (FLMT) to the composite system was deduced. The initial excitation energy of the composite system was determined from the deduced FLMT, assuming an incomplete fusion scenario by utilizing a massive-transfer model. The dependence of the relative IMF yields on the excitation energy for near-scission emission exhibits considerably different behavior as compared to the early stage/isotropic emission component

The measured fission-fragment folding-angle distributions for binary events have been compared with previous measurements for similar systems. Both the general shape and the trends with increasing excitation energy are in good agreement with previously published results. The measured binary fission cross-section was also

found to be in agreement with previously published results for the same and similar systems. For ternary events, a comparison of the dependence of the mean fission-fragment folding angle on $Z_{\rm IMF}$ for both isotropic and near-scission IMF emission has revealed a striking dissimilarity for heavier fragments. For isotropic emission the mean fission-fragment folding angle is observed to be a monotonically decreasing function of $Z_{\rm IMF}$, consistent with linear momentum conservation. For fragments emitted near scission with $Z_{\rm IMF} \leq 6$ the same general trend is observed. However, for heavier near-scission fragments, with $Z_{\rm IMF} \geq 7$, the mean fission-fragment folding angle increases with increasing $Z_{\rm IMF}$, indicating that heavier IMFs emitted from the neck region between the two nascent fission fragments are associated with more peripheral collisions. This behavior suggests a dependence on the orbital angular momentum of the entrance channel.

Examination of the excitation energy dependence of the relative yields of ternary fragments has provided additional evidence for non-standard statistical emission of heavier fragments near-scission. For isotropically emitted IMFs, the relative yields as a function of the excitation energy of the composite system are consistent with statistical emission from a compact source, with Z-dependent emission barriers. In contrast, for near-scission emission the relative yields do not show the same Z dependence of the emission probability, thus indicating an emission mechanism that is not solely dependent on the excitation of the composite system. Our interpretation of the apparent link between the centrality of the initial interaction and the size of the ternary fragment in near-scission emission suggests that perhaps more peripheral collisions lead to more stretched initial configurations of the composite system, which then affects the subsequent decay. General considerations indicate that the survival of any dynamical stretching should depend sensitively on the magnitude and tensorial properties of nuclear dissipation. Dynamical production of fragments in ternary fission might thus serve as a sensitive probe of nuclear dissipation.

One of the presently debated issues in the field is the density dependence of the asymmetry term in the nuclear equation of state (EOS). Nuclear matter is a

binary fluid of protons and neutrons. The N/Z composition of the fluid influences the phase diagram for nuclear matter. How the N/Z composition depends on the density is presently a topic of considerable interest. The degree of neutron enrichment in the neck region, as evidenced by the isotopic composition of ternary IMFs, could provide a tool to gain insights into N/Z composition at low density. Ternary fission allows for clean selection of a process in which a portion of the nuclear matter, the neck region, is low density at some point during the decent from saddle to scission. Fragments emitted near scission could be used as probes of N/Z in this low density region. Measurements for spontaneous and low-energy-induced ternary fission have shown a pronounced enhancement of neutron-rich isotopes for fragments emitted near scission, consistent with the commonly held idea that the neck region between the two nascent fission fragments is itself neutron rich. The tendency to favor neutron-rich isotopes has also been observed in light-ion (α and ^{3}He) induced ternary fission. However, to date there has been no conclusive evidence that this observation holds for heavy-ion-induced ternary fission, where both the initial excitation energy and the angular momentum of the composite system can be much higher. A heavy-ion-induced ternary fission study that provides isotopic identification of the neck fragments may thus provide valuable information neutron content of the neck and perhaps even provide insight into the density dependence of the asymmetry term in the nuclear EOS.

The relative velocities of the fission fragments is a sensitive probe of nuclear dissipation. Any dynamical stretching prior to scission should be evident in the fission fragment velocities. To date all ternary fission studies have assumed that Viola systematics are followed in the case of ternary fission. The Viola systematics, derived for binary fission, were used to deduce several important quantities in the present analysis. Although it has been determined that the relative velocities of the fission fragments do not depend sensitively on the excitation of the fissioning system in binary fission, it remains to be proven whether ternary fission can be adequately described by the same or similar systematics.

While ternary fission is an extremely interesting process, the yield for ternary fission is small in comparison to binary fission, which remains the dominant process. Therefore, direct comparison of experimental data with theoretical models requires the models to predict not just the average behavior but the entire distribution of possibilities sampled by the fissioning system. For example, inclusion of fluctuations in a physically meaningful way into the Los Alamos dynamical model of fission would allow a more direct comparison to experimental results. This requirement remains a significant theoretical challenge, which ultimately limits our ability to fully utilize the information provided by ternary fission studies.

Appendix A

Euler Transformations

A method was developed to simplify the transformation from the coordinate system defined within the position sensitive detectors, $\mathbf{x}''$, to the laboratory coordinate system, $\mathbf{x}$, where

$$\mathbf{x}'' = \begin{pmatrix} x'' \\ y'' \\ z'' \end{pmatrix} \qquad \text{and} \qquad \mathbf{x} = \begin{pmatrix} x \\ y \\ z \end{pmatrix}.$$

The intersection of the incident beam with the target foil defines the origin for both coordinate systems. The laboratory z-axis is defined by the beam, with positive z being downstream, and the horizontal plane containing the beam is the (y,z)-plane. The detector z''-axis passes through the center of the active area of the detector.

We start by mentally placing each detector at a well defined location within the laboratory coordinate system. A convenient choice would be to center the detector on the z-axis at the appropriate distance from the target position. In this position the x- and y-axes of the detector coordinate system are parallel to those for the laboratory coordinate system, and the z-axes of the two overlap. Furthermore, since the detectors are not position sensitive in the z coordinate of the detector system we can set the detector z coordinate to whatever value we please. The simplest choice would of course be to set it equal to the distance from the target to the center of the detector, which we will call d.
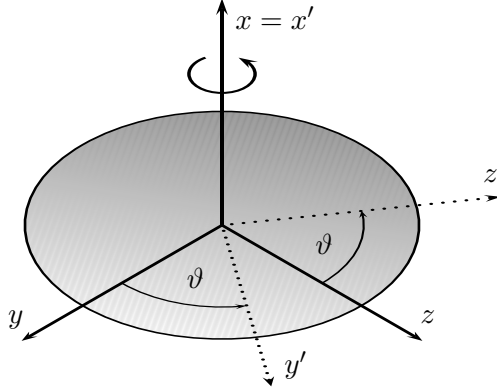
Figure A.1: Counterclockwise rotation by an angle ϑ about the x axis. The coordinate transformation is described by the rotational matrix λ_ϑ.

We now treat the angular position of the detector as two rotational transformations that will take the detector from its (imaginary) starting position on the z-axis to the position it occupied during the experiment. A rotation by an angle ϑ about the laboratory x-axis is described by the matrix

$$
\lambda_\vartheta = \begin{pmatrix} 1 & 0 & 0 \\ 0 & \mathrm{Cos}\,\vartheta & \mathrm{Sin}\,\vartheta \\ 0 & -\mathrm{Sin}\,\vartheta & \mathrm{Cos}\,\vartheta \end{pmatrix}
$$

where the angle ϑ is positive for a counterclockwise rotation in a right handed coordinate system. At his point the (y,z)- and (y',z')-planes are coincident (see Fig. A.1). For the in-plane detectors the above rotational matrix is all that is necessary to transform from the detector to the laboratory coordinate systems. For detectors located out of the horizontal plane a second rotation is necessary described by the angle φ with respect to the (y',z')-plane. Note, although the rotation angle ϑ has a direct correspondence with the spherical coordinate θ in the laboratory system the rotation angle φ does not have such a correspondence with the spherical coordinate ϕ. A rotation by an angle φ about the y'-axis is described by the matrix
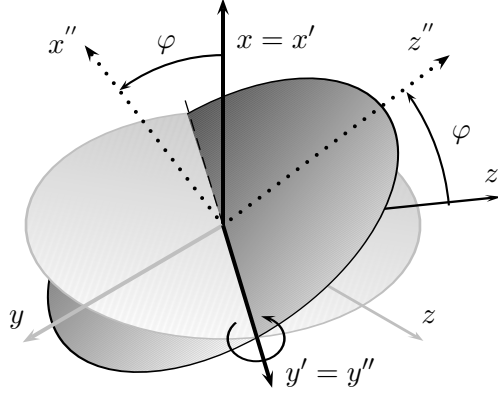
Figure A.2: Counterclockwise rotation by an angle φ about the y' axis. The coordinate transformation is described by the rotational matrix λ_φ.

$$
\lambda_\varphi = \begin{pmatrix} \mathrm{Cos}\,\varphi & 0 & -\mathrm{Sin}\,\varphi \\ 0 & 1 & 0 \\ \mathrm{Sin}\,\varphi & 0 & \mathrm{Cos}\,\varphi \end{pmatrix}
$$

where the angle φ is positive for a counterclockwise rotation (see Fig. A.2). For in-plane detectors $\varphi = 0$, and λ_φ becomes the unit matrix ($\lambda_\varphi = \underline{1}$) Combining both rotations we have the following transformation that moves the detector, and its internal coordinate system, from its starting position to its final position

$$
\mathbf{x} = \lambda_\varphi \lambda_\vartheta \mathbf{x}''. \tag{A.1}
$$

Solving Eq. A.1 for the laboratory coordinates $\mathbf{x}$ provides the required equations,

$$
\begin{aligned}
x &= x''\,\mathrm{Cos}\,\varphi + y''\,\mathrm{Sin}\,\vartheta\,\mathrm{Sin}\,\varphi - z''\,\mathrm{Cos}\,\vartheta\,\mathrm{Sin}\,\varphi \\
y &= y''\,\mathrm{Cos}\,\vartheta + z''\,\mathrm{Sin}\,\vartheta \\
z &= x''\,\mathrm{Sin}\,\varphi - y''\,\mathrm{Sin}\,\vartheta\,\mathrm{Cos}\,\varphi + z''\,\mathrm{Cos}\,\vartheta\,\mathrm{Cos}\,\varphi.
\end{aligned}
$$

Although the above equations were derived only for the center of the detector, $(x'',y'',z'') = (0,0,d)$, the transformation is valid for mapping any set of coordinates (x'',y'',d) to the corresponding laboratory coordinates (x,y,z).

Appendix B

Kinematic Reconstruction

An iterative, self-consistent method was developed for the kinematic reconstruction of binary and ternary fission events. The fission fragment folding angle technique was used for both event types to deduce several quantities of interest, including the fractional linear momentum transfer (FLMT) from the projectile to the resulting composite system [1, 2]. The deduced FLMT was then used in the framework of the Massive Transfer model to calculate the initial excitation energy of the composite system [3]. A flow diagram for the reconstruction procedure is provided in Fig. B.1. A limit was placed on the number of allowed iterations in each step to avoid a runaway loop in the analysis program. Events which could not be reconstructed within this limit were discarded. This method was successful in reconstructing almost 100% of binary and over 95% of ternary events in the current data.

At the beginning of the procedure, initial values are chosen for the mass and charge numbers as well as the velocity, v_{CN}, of the composite system, consistent with pre-equilibrium neutron emission following complete fusion of the projectile and target. The first iteration loop performs a binary search over possible values of the velocity of the composite nucleus. The loop exits when a value for v_{CN} is found such that, when it is used in the reconstruction equations, reproduces the experimentally measured fission fragment folding angle to within $\pm 0.5°$. The second loop uses the results from the first to calculate the mass of the composite nucleus,
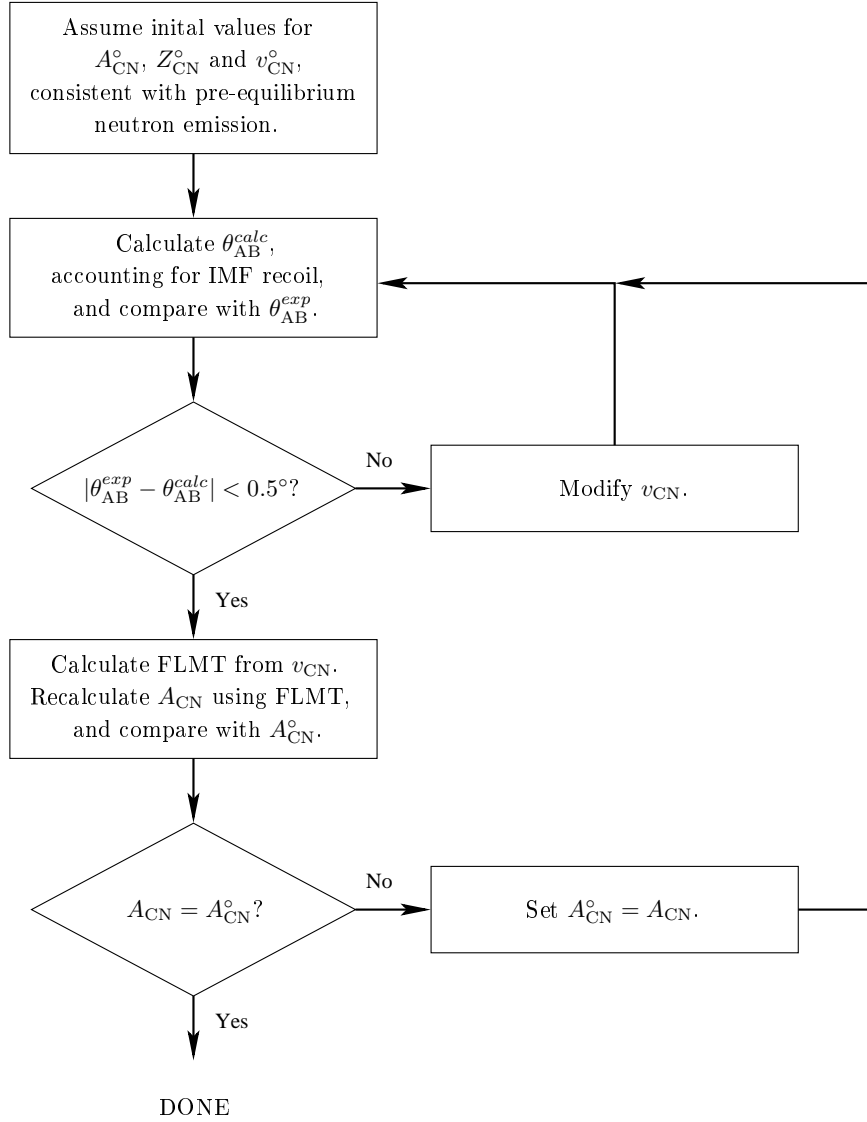
Figure B.1: Flow diagram for the kinematic reconstruction of binary and ternary events.

A_{CN}, and compares this result with the initial value. If the two do not agree, then the newly calculated mass is substituted for the initial mass and the process is repeated from the beginning. The reconstruction was designed so that a minimum of two cycles through the iteration loops were performed. Thus, the reconstruction was not considered complete until the calculated masses from two consecutive cycles were in agreement.

The remainder of this Appendix will focus on deriving the equations used in the reconstruction, as well as those used to calculate other important quantities. The following conventions will be used in describing the derivation:

- Vector quantities will be denoted by bold symbols, e.g. $\mathbf{v}_{\mathrm{A}}$.

- The magnitude of a vector quantity will be denoted by the script version of the vector symbol, e.g. $|\mathbf{v}_{\mathrm{A}}| = v_{\mathrm{A}}$.

- Unprimed variables refer to quantities viewed in the laboratory reference frame.

- Single primed variables refer to quantities viewed in the center-of-mass frame of the composite nucleus (CN).

- Double primed variables refer to quantities viewed in the center-of-mass frame of the fissioning system (FS), i.e. after accounting for the recoil from the ternary particle.

B.1   Vector Relations

A vector diagram for binary fission showing the fission fragment velocities in the laboratory and the center-of-mass of the composite nucleus is presented in Fig. B.2. For binary and ternary fission, the fission fragment emission angles measured in the laboratory were directly observed quantities. The laboratory folding angle was defined as the sum of the two emission angles, $\theta_{\mathrm{AB}} = \theta_{\mathrm{A}} + \theta_{\mathrm{B}}$, as measured in the plane containing the target and both fission fragments (the fission plane). The magnitudes of the laboratory velocities of the two fission fragments, v_{A} and v_{B},
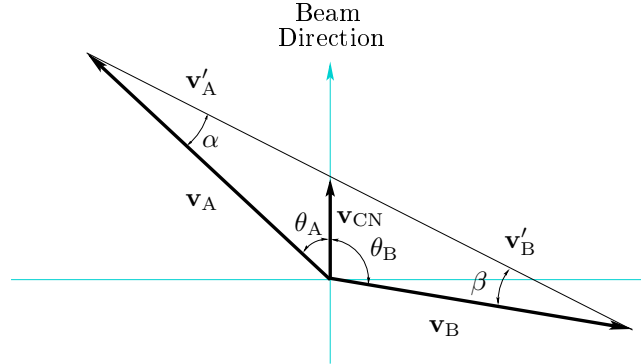
Figure B.2: Vector diagram of the fission fragment velocities for binary fission. The emission angles θ_A and θ_B for fragments A and B, respectively, were directly measured quantities. The velocity of the composite nucleus formed by the fusion of projectile and target is labelled $\mathbf{v}_{CN}$ in the diagram.

---

were calculated from their respective times-of-flight with respect to the recorded accelerator RF signal or were calculated from Viola systematics as described in Sec. B.3.

The emission of the third, or ternary particle in ternary fission reduces the mass of the residual fissioning nucleus, and introduces an additional momentum component from the recoil as shown in Fig. B.3. The recoil momentum had to be included in the calculations to provide an accurate reconstruction of each event. A vector diagram of the velocities for a ternary event is given in Fig. B.4, where the velocity of the composite nucleus, $\mathbf{v}_{CN}$, has been replaced by the velocity of the fissioning system, $\mathbf{v}_{FS}$. From this diagram it was possible to write out the following trigonometric relations:

$$\frac{\sin \alpha}{v_B} = \frac{\sin \theta_{AB}}{v_A'' + v_B''} \tag{B.1}$$

$$\frac{\sin \beta}{v_A} = \frac{\sin \theta_{AB}}{v_A'' + v_B''} \tag{B.2}$$
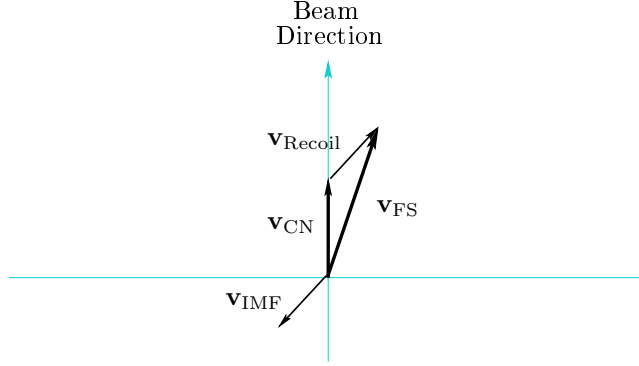
Figure B.3: For ternary events the recoil velocity from the emission of the ternary particle was added to the composite nucleus velocity to construct the velocity vector for the residual fissioning system, $\mathbf{v}_{\text{FS}}$. For binary events the recoil velocity was zero, which left $\mathbf{v}_{\text{FS}}$ equal to $\mathbf{v}_{\text{CN}}$.

$$\frac{\sin \alpha}{v_{\text{B}}} = \frac{\sin \beta}{v_{\text{A}}} \tag{B.3}$$

$$\frac{\sin \alpha}{v_{\text{FS}}} = \frac{\sin \theta_{\text{A-FS}}}{v_{\text{A}}''} \tag{B.4}$$

$$\frac{\sin \beta}{v_{\text{FS}}} = \frac{\sin \theta_{\text{B-FS}}}{v_{\text{B}}''} \tag{B.5}$$

and

$$v_{\text{B}}''^2 = v_{\text{FS}}^2 + v_{\text{B}}^2 - 2v_{\text{FS}}v_{\text{B}} \cos \theta_{\text{B-FS}}. \tag{B.6}$$

where $\theta_{\text{AB}} = \theta_{\text{A-FS}} + \theta_{\text{B-FS}}$. The angles $\theta_{\text{A-FS}}$ and $\theta_{\text{B-FS}}$ were not directly observed quantities but their sum θ_{AB} was required to be equal to the sum of the observed angles θ_{A} and θ_{B}.

These relations will be used in the derivations detailed in the following sections. In binary fission the center-of-mass frame of the fissioning system is equivalent to that for the composite nucleus ($v_{\text{Recoil}} = 0$ in Fig. B.3). Because of this, these relations are valid for both binary and ternary events.
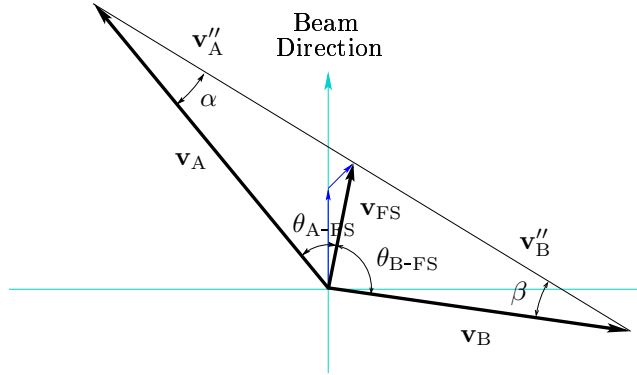
Figure B.4: Vector diagram of the fission fragment velocities for ternary fission. The angles $\theta_{\text{A-FS}}$ and $\theta_{\text{B-FS}}$ for fragments A and B, respectively, were calculated following the derivation in Sec. B.4. For binary fission $\mathbf{v}_{\text{FS}} = \mathbf{v}_{\text{CN}}$, and the problem reduces to that described in Fig. B.2.

B.2   Fission Fragment Mass Ratio

The first step in the reconstruction was to determine the mass ratio of the two fission fragments. A ratio of the velocities of the two fission fragments in the center-of-mass of the fissioning system was constructed using Eqs. B.4 and B.5:

$$\left.\begin{array}{l} v''_{\text{A}} = v_{\text{FS}} \dfrac{\sin \theta_{\text{A-FS}}}{\sin \alpha} \\[2mm] v''_{\text{B}} = v_{\text{FS}} \dfrac{\sin \theta_{\text{B-FS}}}{\sin \beta} \end{array}\right\} \qquad \dfrac{v''_{\text{A}}}{v''_{\text{B}}} = \dfrac{\sin \theta_{\text{A-FS}}}{\sin \theta_{\text{B-FS}}} \dfrac{\sin \beta}{\sin \alpha} \tag{B.7}$$

The dependence on the unknown angles α and β was then eliminated by substitution of a rearranged form of Eq. B.3

$$\frac{\sin \beta}{\sin \alpha} = \frac{v_{\text{A}}}{v_{\text{B}}}$$

which leads to

$$\frac{v''_{\text{A}}}{v''_{\text{B}}} = \frac{v_{\text{A}} \sin \theta_{\text{A-FS}}}{v_{\text{B}} \sin \theta_{\text{B-FS}}}. \tag{B.8}$$

This left the ratio of the center-of-mass velocities as a function of the determinable quantities v_{A}, v_{B}, $\theta_{\text{A-FS}}$, and $\theta_{\text{B-FS}}$. The fission fragment velocities were deduced

from their respective times-of-flight.

Invoking conservation of linear momentum in the center-of-mass frame of the fissioning system provided a relation between the fission fragment velocities in that frame and their respective masses, A_A and A_B,

$$A_A v_A'' = A_B v_B'' \qquad \Longrightarrow \qquad \frac{v_A''}{v_B''} = \frac{A_B}{A_A}.$$

Substitution of this result into Eq. B.8 lead to

$$\frac{A_B}{A_A} = \frac{v_A \sin \theta_{A\text{-FS}}}{v_B \sin \theta_{B\text{-FS}}} \equiv R \qquad (B.9)$$

which provided the required relation between the ratio of the fission fragment masses, R, and the angles and velocities as measured in the laboratory. With this relation it was possible to deduce the individual masses and charges of the fragments once the mass and charge of the fissioning system were known:

$$A_A = \frac{A_{FS}}{R+1} \qquad \text{and} \qquad A_B = \frac{R A_{FS}}{R+1} = A_{FS} - A_A \qquad (B.10)$$

$$Z_A = \frac{Z_{FS}}{R+1} \qquad \text{and} \qquad Z_B = \frac{R Z_{FS}}{R+1} = Z_{FS} - Z_A. \qquad (B.11)$$

The actual values of A_{FS} and Z_{FS} were determined by application of the massive transfer model as described in Sec. B.4. Since the angles $\theta_{A\text{-FS}}$ and $\theta_{B\text{-FS}}$ were not observed quantities, it was necessary to make a first approximation by substituting the measured values of θ_A and θ_B for the first pass through the iterative reconstruction described in Sec. B.4. Once the velocity vector of the fissioning system, $\mathbf{v}_{FS}$, had been determined, it was possible to recalculate the mass ratio R using the calculated values of $\theta_{A\text{-FS}}$ and $\theta_{B\text{-FS}}$.

For cases where the time-of-flight information was not available, the fission fragment mass ratio was determined from a modified ratio of the anode pulse heights from the PPACs. It was determined that the following relation produced good agreement with the mass ratio calculated from the time-of-flight:

$$R = \frac{a_A f + a_B}{a_B} - 1.0.$$

In the above equation a_A and a_B are the anode pulse heights for fragments A and B respectively. The quantity f is a pseudo-normalization factor chosen to force the centroids of the two anode pulse height distributions, a_A and a_B, to be equal (assumes that the most probable mass split is symmetric). This value for the mass ratio was then used to determine the mass and charge numbers for the two fission fragments.

B.3   Fission Systematics

For cases where the time-of-flight information was not available, the fission fragment velocities in the center-of-mass of the fissioning system were calculated using Viola systematics [2, 4]. The most probable total kinetic energy ($\overline{TKE}$) available to the fission fragments in the center-of-mass of the fissioning system was calculated as

$$\overline{TKE} = 0.755 \, \frac{Z_A Z_B}{A_A^{1/3} + A_B^{1/3}} + 7.3 \, \text{MeV} \tag{B.12}$$

which expresses the total kinetic energy as a function of the mass and charge numbers of the two fission fragments. Equation B.12 can also be written as

$$\overline{TKE} = \frac{A_A v_A''^2}{2} + \frac{A_B v_B''^2}{2}.$$

in which the total energy is expressed in terms of the mass numbers and velocities of the two fission fragments. The two velocities were separated by invoking conservation of linear momentum, which allowed the expression of v_A'' in terms of v_B'' and vice versa

$$v_A'' = \frac{A_B}{A_A} v_B'' \qquad \text{and} \qquad v_B'' = \frac{A_A}{A_B} v_A''.$$

Substitution of each of these in turn into Eq. B.3 made it possible to solve for v_A'' and v_B'' independently

$$v_A'' = \sqrt{\frac{2\,\overline{TKE}}{A_A \left(1 + A_A/A_B\right)}} \tag{B.13}$$

$$v_B'' = \sqrt{\frac{2\,\overline{TKE}}{A_B \left(1 + A_B/A_A\right)}}, \tag{B.14}$$

each of which could be transformed back to the laboratory reference frame. Thus, using the results from Sec. B.2, it was possible to calculate the total kinetic energy available to the two fission fragments in the center-of-mass of the fissioning system using Eq. B.12. Once the total kinetic energy was determined, it was then possible to calculate the velocities of the two fission fragments using Eqs. B.13 and B.14.

B.4   Linear Momentum Transfer

As mentioned previously, the angle $\theta_{\text{B-FS}}$ (see Fig. B.4) was not a measured quantity. While the direction of the velocity vector for fission fragment B was measured, that for the velocity of the fissioning system had to be calculated taking into account both the velocity of the composite nucleus, $\mathbf{v}_{\text{CN}}$, and the recoil from the ternary IMF. The laboratory velocity vector of the ternary IMF was calculated from the measured kinetic energy using an assumed mass as a function of Z_{IMF}, and the known detector position:

$$v_{\text{IMF}} = \sqrt{\frac{2E_{\text{IMF}}}{m_{\text{IMF}}}} \qquad \text{and} \qquad \mathbf{v}_{\text{IMF}} = v_{\text{IMF}}\hat{\mathbf{r}}_{\text{IMF}}$$

where $\hat{\mathbf{r}}_{\text{IMF}}$ is the unit position vector directed from the target toward the center of the Si detector quadrant that detected the ternary IMF, and m_{IMF} is the assumed mass. Next, the velocity of the ternary particle was transformed into the center-of-mass of the composite nucleus, and then converted into the corresponding momentum vector

$$\mathbf{v}'_{\text{IMF}} \;\; = \;\; \mathbf{v}_{\text{IMF}} - \mathbf{v}_{\text{CN}} \tag{B.15}$$

$$\mathbf{p}'_{\text{IMF}} \;\; = \;\; m_{\text{IMF}}\mathbf{v}'_{\text{IMF}}$$

where $\mathbf{v}_{\text{CN}}$ denotes the laboratory velocity of the composite nucleus. By conservation of linear momentum, the recoil momentum of the residual nucleus in the CN center-of-mass is equal and opposite to the momentum of the ternary particle

$$\mathbf{p}'_{\text{FS}} \;\; = \;\; \mathbf{p}'_{\text{recoil}} = -\mathbf{p}'_{\text{IMF}}$$

$$\mathbf{v}'_{\text{FS}} = \frac{1}{A_{\text{FS}}}\mathbf{p}'_{\text{FS}}.$$

Finally, the velocity vector of the fissioning system is transformed back to the laboratory system, and the angle between it and the measured unit position vector for fission fragment B is calculated:

$$\mathbf{v}_{\text{FS}} = \mathbf{v}'_{\text{FS}} + \mathbf{v}_{\text{CN}} \tag{B.16}$$

$$\theta_{\text{B-FS}} = \cos^{-1}\left[\frac{\hat{\mathbf{r}}_{\text{B}} \cdot \mathbf{v}_{\text{FS}}}{v_{\text{FS}}}\right]. \tag{B.17}$$

These steps provide the velocity of the fissioning system, v_{FS}, as well as one of the two angular quantities required to complete the reconstruction, $\theta_{\text{B-FS}}$, using simple vector algebra.

In order to determine the fractional linear momentum transfer from projectile to target, FLMT, it was necessary to deduce the velocity of the composite nucleus, v_{CN}, prior to the emission of the ternary particle. Utilizing Eqs. B.1, B.4 and B.9, it was possible to construct the following expression:

$$\begin{aligned}
v_{\text{B}} &= \left(v''_{\text{A}} + v''_{\text{B}}\right)\frac{\sin\alpha}{\sin\theta_{\text{AB}}} \\[2mm]
&= v_{\text{FS}}\left(\frac{v''_{\text{A}} + v''_{\text{B}}}{v''_{\text{A}}}\right)\frac{\sin\theta_{\text{A-FS}}}{\sin\theta_{\text{AB}}} \\[2mm]
&= v_{\text{FS}}\left(1 + \frac{v''_{\text{B}}}{v''_{\text{A}}}\right)\frac{\sin\theta_{\text{A-FS}}}{\sin\theta_{\text{AB}}} \\[2mm]
&= v_{\text{FS}}\left(1 + \frac{1}{R}\right)\frac{\sin\theta_{\text{A-FS}}}{\sin\theta_{\text{AB}}}. \tag{B.18}
\end{aligned}$$

where $\theta_{\text{AB}} = \theta_{\text{A-FS}} + \theta_{\text{B-FS}}$. This expression can be simplified by defining the intermediate variables

$$\kappa \equiv \left(1 + \frac{1}{R}\right) \quad \text{and} \quad \xi \equiv \frac{\sin\theta_{\text{A-FS}}}{\sin\theta_{\text{AB}}} \tag{B.19}$$

which, when substituted into Eq. B.18, provide the more compact result

$$v_{\text{B}} = v_{\text{FS}}\kappa\xi.$$

Substituting this into Eq. B.6 gives

$$v_B''^2 = v_{FS}^2 + v_{FS}^2 \kappa^2 \xi^2 - 2 v_{FS}^2 \kappa \xi \cos \theta_{B\text{-}FS}$$

or

$$\xi^2 - \frac{2 \cos \theta_{B\text{-}FS}}{\kappa} \xi + \frac{1}{\kappa} \left(1 - \frac{v_B''^2}{v_{FS}^2} \right) = 0$$

which is a quadratic equation of the variable ξ. Finally, solving for ξ we have

$$\xi = \frac{1}{\kappa} \left[\cos \theta_{B\text{-}FS} \pm \sqrt{\cos^2 \theta_{B\text{-}FS} + \frac{v_B''^2}{v_{FS}^2} - 1} \right]. \tag{B.20}$$

Using Eq. B.20 as the definition of ξ, a modified form of the original definition in Eq. B.19 was used to solve for $\theta_{A\text{-}FS}$ in terms of ξ and $\theta_{B\text{-}FS}$:

$$\xi = \frac{\sin \theta_{A\text{-}FS}}{\sin \theta_{AB}} = \frac{\sin \theta_{A\text{-}FS}}{\sin \theta_{A\text{-}FS} \cos \theta_{B\text{-}FS} + \cos \theta_{A\text{-}FS} \sin \theta_{B\text{-}FS}}$$

$$\xi \sin \theta_{A\text{-}FS} \cos \theta_{B\text{-}FS} + \xi \cos \theta_{A\text{-}FS} \sin \theta_{B\text{-}FS} - \sin \theta_{A\text{-}FS} = 0$$

$$\xi \tan \theta_{A\text{-}FS} \cos \theta_{B\text{-}FS} + \xi \sin \theta_{B\text{-}FS} - \tan \theta_{A\text{-}FS} = 0$$

$$\tan \theta_{A\text{-}FS} \left(\xi \cos \theta_{B\text{-}FS} - 1 \right) + \xi \sin \theta_{B\text{-}FS} = 0$$

$$\tan \theta_{A\text{-}FS} = \frac{\xi \sin \theta_{B\text{-}FS}}{1 - \xi \cos \theta_{B\text{-}FS}}$$

$$\theta_{A\text{-}FS} = \tan^{-1} \left(\frac{\xi \sin \theta_{B\text{-}FS}}{1 - \xi \cos \theta_{B\text{-}FS}} \right) \tag{B.21}$$

where the value of ξ was determined using Eq. B.20. This provided a means to calculate $\theta_{A\text{-}FS}$ using previously determined quantities, i.e. an assumed value for v_{CN}, the fission fragment mass ratio from Eq. B.9, the center-of-mass velocity of fission fragment B from Eq. B.14, the velocity of the fissioning system from Eq. B.16, and finally the angle between the position vector of fission fragment B and the velocity vector of the fissioning system from Eq. B.17.

It was now possible to construct a calculated value for the fission fragment folding angle as a function of the assumed value for the velocity of the composite nucleus and

the geometry of the reaction. The constructed folding angle was then compared with the measured folding angle. The criteria for agreement between the experimentally measured folding angle, $\theta_{\text{AB}}^{exp} = \theta_{\text{A}} + \theta_{\text{B}}$, and the calculated folding angle, $\theta_{\text{AB}}^{calc} = \theta_{\text{A-FS}} + \theta_{\text{B-FS}}$, was that the absolute difference between the two must be less than $0.5°$, i.e.

$$|\theta_{\text{AB}}^{exp} - \theta_{\text{AB}}^{calc}| < 0.5°.$$

If this condition were true, then additional quantities were calculated, as described later in this section. If this criterion was not met, then the assumed value for v_{CN} was modified and the process repeated. Thus it was possible to calculate $\theta_{\text{AB}}^{calc}$ iteratively from trial values of v_{CN} until it agreed with the observed value of θ_{AB}^{exp}. Because of the placement and geometry of the detector telescopes, the direction of v_{Recoil} and thus v_{FS} was known to within $\pm 2.4°$.

The the final steps in the kinematic reconstruction were to calculate the fractional linear momentum transfer (FLMT) from the incomplete fusion of the projectile and target and the initial excitation energy consistent with the calculated FLMT. In the massive transfer model the fraction of the projectile nucleus that does not fuse with the target nucleus is assumed to continue along the projectile trajectory with its original velocity, v_P, such that

$$\rho = \frac{v_{\text{CN}}}{v_{\circ}} \left[1 + \frac{A_P}{A_T} \left(1 - \frac{v_{\text{CN}}}{v_{\circ}} \right) \right] \tag{B.22}$$

where ρ is the FLMT, v_{CN} is the velocity of the composite nucleus (i.e. the composite system formed by the incomplete fusion of projectile and target nuclei), $v_{\circ}$ is the CN velocity for the case of complete fusion, and A_P and A_T are the mass numbers of the projectile and target respectively [3]. Once the FLMT had been determined, the mass and charge of the CN were recalculated as

$$A_{\text{CN}} = A_T + \rho A_P \qquad \text{and} \qquad Z_{\text{CN}} = Z_T + \rho Z_P.$$

The integer value of the newly calculated CN mass was then compared to the value used in the earlier calculations. If the masses did not agree, then the entire process

was repeated using the new mass value.

Finally, for each event successfully reconstructed the deduced FLMT was used to calculate the initial excitation energy of the composite system within the framework of the massive transfer model. For this model the initial excitation is defined as

$$\langle E^* \rangle = E_P \rho \frac{A_T}{A_T + \rho A_P} \sqrt{1 - \left(\frac{v_P}{c}\right)^2} + \langle Q \rangle \tag{B.23}$$

where E_P is the incident projectile energy, ρ is the FLMT, A_T and A_P are the mass numbers of the target and projectile, respectively, v_P is the velocity of the projectile, and $\langle Q \rangle$ is the average Q value of reaction channels consistent with the given ρ. It should be stressed that Eq. B.23 provides only the *initial* excitation energy, that is the excitation energy of the composite nucleus immediately following the projectile/target interaction. Much of this initial excitation may be removed, through neutron emission etc., by the time the system reaches scission.

References

[1] T. Sikkeland, E. Haines, and V. Viola, Jr., Phys. Rev. **125**, 1350 (1962).

[2] V. Viola, Jr. and T. Sikkeland, Phys. Rev. **130**, 2044 (1963).

[3] E. Mordhorst *et al.*, Phys. Rev. C **43**, 716 (1991).

[4] V. Viola, K. Kwiatkowski, and M. Walker, Phys. Rev. C **31**, 1550 (1985).

Appendix C

Geometric Efficiency Corrections

In order to correct for limitations in the experimental detector geometry, a Monte Carlo simulation was written based on the kinematic equations derived in Appendix B. The simulation allowed for quantitative determination of the detector efficiencies, ε, for observing coincident fission fragments for the case of binary fission as well as fission accompanied by intermediate mass fragment (IMF) emission. The plots presented in this appendix all resulted from simulation of the reaction ^{12}C + ^{232}Th at 16 MeV/A.

The geometric efficiency correction factor, $1/\varepsilon$, was determined separately for each of the five IC telescopes, as well as for the case of binary fission, where none of the IC telescopes recorded a hit. Each case used a distinct unit vector defining the direction of the velocity of the fissioning system, $\mathbf{v}_{\mathrm{FS}}$, as measured in the laboratory. This was required for the case of ternary fission because the direction of $\mathbf{v}_{\mathrm{FS}}$ is determined in part by the recoil of the fissioning system resulting from the emission of an IMF. For binary fission $\mathbf{v}_{\mathrm{FS}}$ was assumed to be along the beam direction. The components of the unit vector for each ternary case were determined from the experimental data by plotting the components of $\mathbf{v}_{\mathrm{FS}}$, integrated over Z_{IMF}, and extracting the mean values. Justification for integrating over Z_{IMF} is provided in Sec. C.3. The geometric efficiency correction was determined as a function of both the velocity of the fissioning system, v_{FS}, and the fission fragment folding angle, θ_{AB},

for each of the six cases.

The resulting detector efficiency curves as a function of v_{FS} were used in the analysis of the experimental data by correcting the counts on an event-by-event basis, i.e. each real event recorded during the experiment was treated as $1/\varepsilon(v_{\text{FS}})$ events in the subsequent analysis. This of course had to be done after the value of v_{FS} had been determined for the event. The detector efficiency curves as a function of θ_{AB} were used only for the creation of efficiency corrected fission fragment folding angle distributions.

C.1   PPAC Masks

A mask array was generated in θ, ϕ space for each pair of PPACs to simulate the active area of the detectors as they were positioned during the experiment. The granularity of each mask arrays was $0.1°$ in both θ and ϕ. The arrays were used as an event filter to determine the number of simulated events for which both fission fragments would have been detected. For each simulated event, if the final position vector of a simulated fission fragment corresponded with an "active" array element in a detector mask, then the fragment was considered to have been detected.

Plots of the detector masks for the in-plane and out-of-plane PPAC pairs are shown in Fig.C.1. Panels (a) and (c) represent the PPACs located left of the beam axis as viewed from upstream, while panels (b) and (d) represent the PPACs located right of the beam axis. Target shadow was accounted for by imposing a cut-off in the mask arrays for the PPACs located left of the beam axis. The cut-off was imposed based on the relative angle between the array element (θ_i, ϕ_j) of the detector mask and the plane defined by the target frame, with the vertex located at the center of the target. Array elements for which this angle was less than or equal to $3.5°$ were cut. Any array elements that were located behind the plane of the target frame as viewed from upstream were also cut.
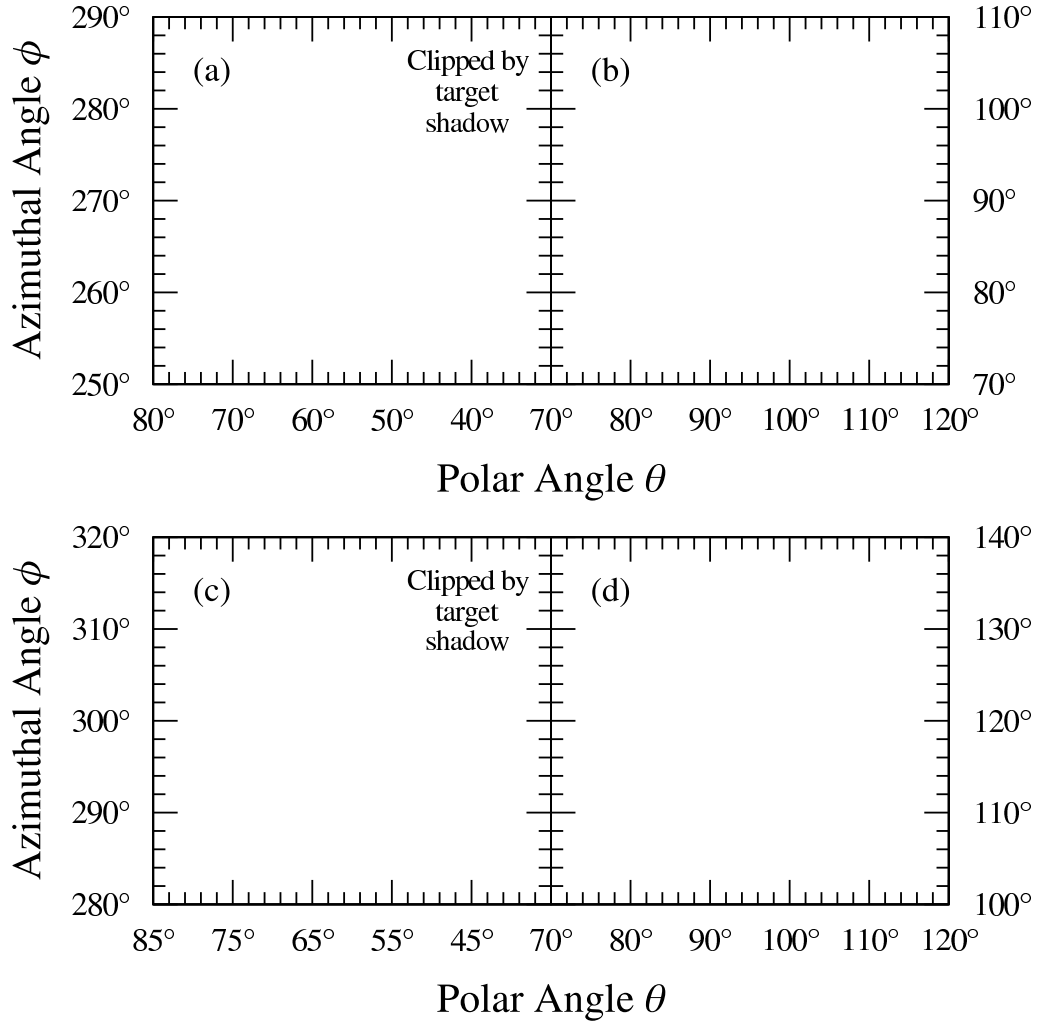
Figure C.1: Detector masks used in the geometric efficiency simulations. Masks in θ, ϕ space simulating the positions of the two in-plane, (a) and (b), and two out-of-plane, (c) and (d), PPACs for the reaction ^{12}C + ^{232}Th at 16 MeV/A. The darker regions in panels (a) and (b) are discussed in Sec. C.5.
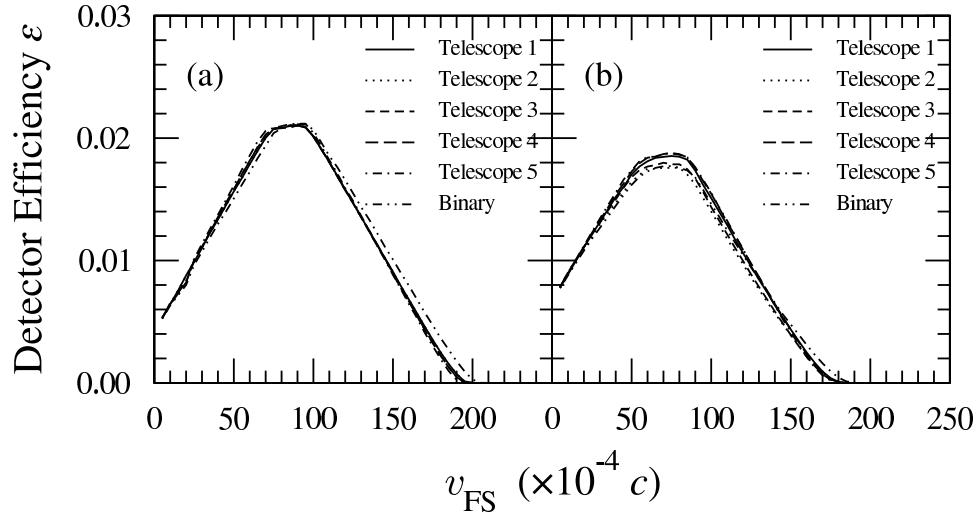
Figure C.2: Geometric efficiency curves for the detection of coincident fission fragments as a function of the deduced velocity of the fissioning system, v_{FS}, for the in-plane (a) and out-of-plane (b) PPAC pairs.

C.2 Geometric Efficiency as a Function of v_{FS}

The general approach used in the simulation was to loop over values of the velocity of the fissioning system, v_{FS}, simulate a fixed number of events for each value, and calculate the fraction of simulated events for which both fission fragments were "detected" in the PPAC mask. The loop covered values $0 \leq v_{FS} \leq 0.025c$ in steps of $0.0005c$ where c is the speed of light in a vacuum. During the analysis the effect of the step size was compensated for by interpolating between the two points in v_{FS} adjacent to the experimentally determined value for the event.

Each simulated event began by generating a random unit vector in the center-of-mass frame of the fissioning system. This unit vector was used to define the direction of motion for one of the two fission fragments. Conservation of linear momentum then required that the direction of motion of the second fission fragment be along a unit vector opposite that of the first. The mass and charge of each fission

fragment was randomly determined from a Gaussian distribution resulting from a fit to the experimental data. The kinetic energies and velocities of the simulated fission fragments were calculate from Viola systematics as described in Sec. B.3 [1, 2]. The velocities were then boosted to the laboratory frame, using the current value of the v_{FS} index, and the resulting vectors were compared to the PPAC mask arrays. The detector efficiencies were defined as the number of simulated events in which both fission fragments were "detected" divided by the total number of simulated events. Plots of the detector efficiencies, ε, as a function of v_{FS}, are shown in Fig.C.2.

C.3   Dependence of ε on Z_{IMF}

As stated previously, the direction of $\mathbf{v}_{\mathrm{FS}}$ for ternary events was determined by the IC telescope position only, with no consideration for the type of ternary particle emitted. To test the validity of this simplification three simulations were run, each using a value of $\mathbf{v}_{\mathrm{FS}}$ based on a different value of Z_{IMF}. Figure C.3 shows the resulting detector efficiency curves for $Z_{\mathrm{IMF}} = 3$, 8 and 13 as determined for telescope 2, which was located orthogonal to the scission axis, using the in-plane PPAC masks. In each case the direction of $\mathbf{v}_{\mathrm{FS}}$ was taken from the experimental data for the specific ternary particle. It is clear from the results that the detector efficiency varies little with Z_{IMF} over the range of experimentally observed values of v_{FS} for ternary events, denoted by the vertical lines in Fig. C.3. Quantitatively, the maximum variation in the geometric efficiency correction factor, $1/\varepsilon$, which occurs for the most peripheral collisions - i.e. the lowest observed values of v_{FS} - is less than 6%.

C.4   Geometric Efficiency as a Function of θ_{AB}

In each simulated event the fission fragment folding angle, θ_{AB}, was calculated. The number of occurrences of a particular value of the folding angle was summed in two arrays, the indices of which were the values of the folding angle with a granularity of $1.0°$. The first array, $\mathbf{m}$, was incremented for each occurrence of a particular value
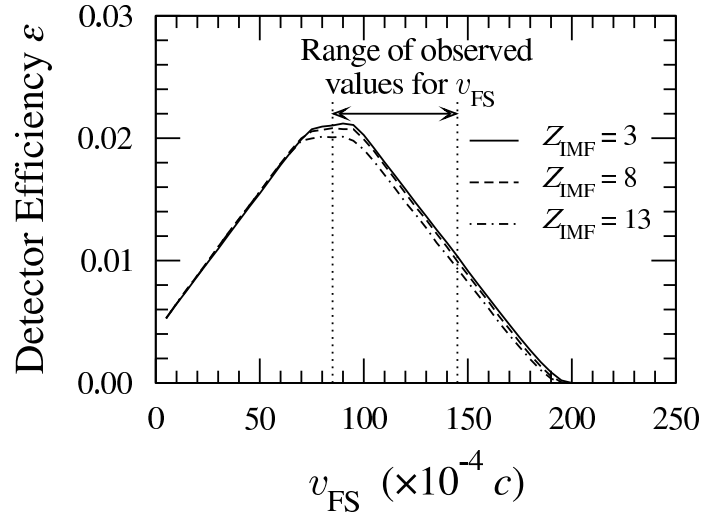
Figure C.3: Geometric efficiency, ε, for the detection of coincident fission fragments in ternary events. The curves represent the results of simulations using a ternary particle with charge $Z_{IMF} = 3$, 8 or 13. The simulations were run using IMF telescope 2 to define the direction of $\mathbf{v}_{FS}$ for each value of Z_{IMF}.

of the folding angle. The second array, $\mathbf{n}$ was only incremented when the simulated event resulted in both fission fragments being detected. In this way it was possible to determine the detection efficiency as a function of the calculated folding angle by dividing the contents of array $\mathbf{n}$ by the corresponding contents of array $\mathbf{m}$

$$\varepsilon_i = \frac{n_i}{m_i},$$

where i spans the allowed values of θ_{AB}. Plots of the detector efficiencies as a function of θ_{AB} are presented in Fig.C.4.

C.5   Validation of the Efficiency Corrections

A general validation of the geometric efficiency corrections was made by comparing the binary fission cross-section, σ_f, as calculated in Sec. 4.6, to binary fission excitation functions for the same and similar systems. The result is presented in Fig.
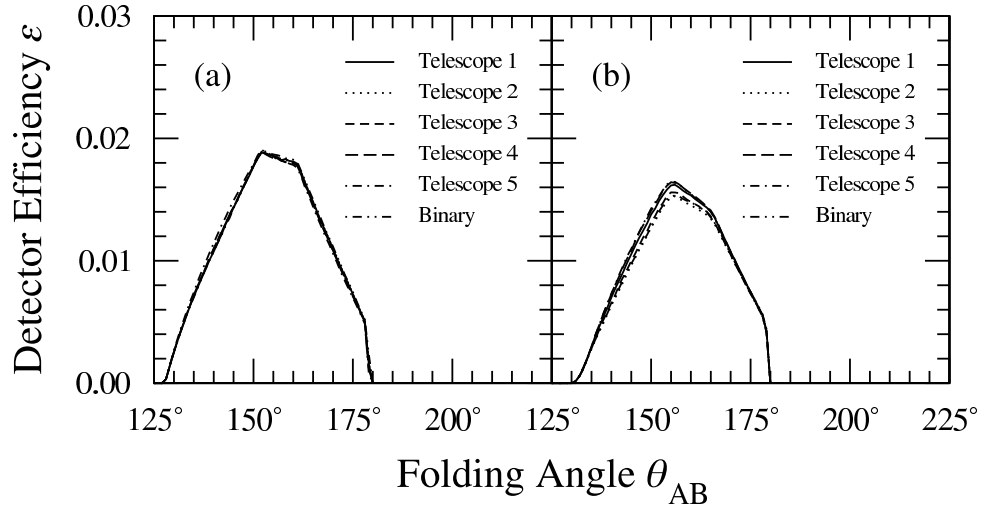
Figure C.4: Geometric efficiency curves for the detection of coincident fission fragments as a function of the measured folding angle, θ_{AB}, for the in-plane (a) and out-of-plane (b) PPACs.

4.15. The binary fission cross-section calculated in the current work, which includes the geometric efficiency corrections, is in good agreement with the asymptotic value of the binary fission excitation functions for all four systems.

To understand the shape of the geometric efficiency curves a simulation was run in which the PPAC masks centered on the horizontal plane were reduced to a fraction of their normal coverage (indicated by the dark regions of panels (a) and (b) in Fig. C.1) The right side PPAC mask was reduced to a 1 cm × 1 cm square centered in the horizontal plane at 95° with respect to the beam axis, while the left side mask was reduced to a horizontal strip 1 cm high centered along its length in the horizontal plane. In this configuration the "detectable" range was limited to $143° \lesssim \theta_{AB} \lesssim 168°$. The efficiency curve as a function of θ_{AB} for this detector geometry is presented in Fig. C.5.

The results of the restricted simulation shows an enhancement in detection efficiency at smaller values of θ_{AB}. This trend is also observed in the efficiency curves
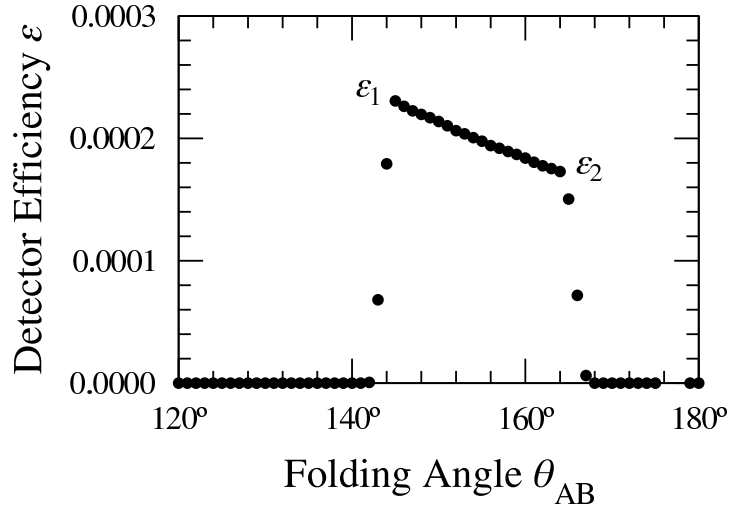
Figure C.5: Geometric efficiency for a restricted event filter.

used in the data analysis as shown in Fig. C.4. This enhancement can be easily understood by considering how the detector masks map into θ, ϕ space. The forward edge of the strip mask ($\theta = 48.5°$) covers a larger fraction of ϕ than does the backward edge ($\theta = 70.0°$). This explanation can be verified by looking at the ratio of the extent in the ϕ coordinate at the two ends of the strip in the left side PPAC mask. At $\theta = 48.5°$ we have $268.73° \leq \phi \leq 271.27°$, which corresponds to an extent of $\Delta\phi = 2.54°$, and at $\theta = 70.0°$ we have $269.02° \leq \phi \leq 270.98°$, which corresponds to an extent of $\Delta\phi = 1.96°$. The ratio of these two values is

$$\frac{\Delta\phi_{48.5°}}{\Delta\phi_{70.0°}} = \frac{2.54°}{1.96°} = 1.30.$$

This result was then compared to the ratio of the geometric efficiencies at the two edges in Fig. C.5. For the points labeled ε_1 and ε_2 we get

$$\frac{\varepsilon_1}{\varepsilon_2} = \frac{0.000231}{0.000173} = 1.34.$$

These two ratios are in agreement to within 3%. This small difference can be accounted for by uncertainties introduced by the finite bin size (1° resolution) used to accumulate and record the results.

References

[1] V. Viola, Jr. and T. Sikkeland, Phys. Rev. **130**, 2044 (1963).

[2] V. Viola, K. Kwiatkowski, and M. Walker, Phys. Rev. C **31**, 1550 (1985).

Appendix D

The Proximity Potential

The attractive force between two adjacent nuclear surfaces gives rise to a proximity energy that is dependent on the size of the gap between the surfaces. Blocki *et. al.* [1] have developed a method of determining the proximity energy between two spheres as a product of a geometrical factor describing their shapes and a universal function describing the separation between the two curved surfaces, both of which are characteristic of the material composing the objects, and related to the surface energy coefficient. The derivation of the expressions for the proximity energy rely on the leptodermous, or thin skin approximation, in which the surface thickness is assumed to be much less than the overall dimensions of the system (i.e. the surface thickness is much less than the diameter of the fragment). The method was later extended by Baltz and Bayman [2] and Malhotra and Gupta [3] to include non-spherical shapes. A schematic describing the orientational parameters is provided in Fig. D.1.

The proximity energy between two adjacent fragments was calculated as

$$E_{\text{Prox}} = 4\pi\gamma\overline{R}b \cdot \Phi(s)$$

where γ is the surface energy coefficient, $\overline{R}$ is the geometric mean of the two principal radii of curvature, b is the Süssman width of a Woods-Saxon surface profile [4], and $\Phi(s)$ is a dimensionless proximity moment as a function of the minimum
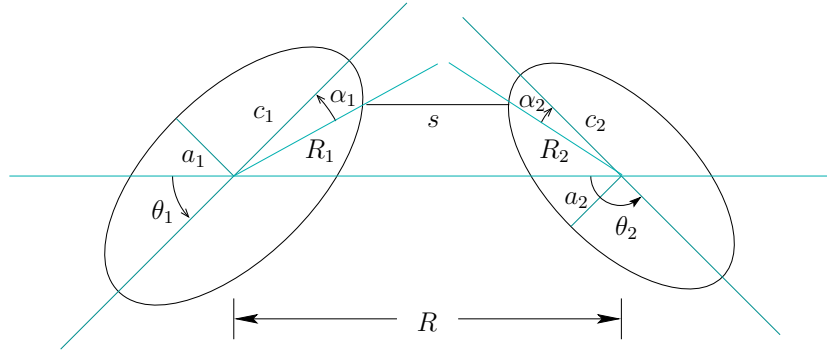
Figure D.1: A schematic configuration of two prolate deformed nuclei lying in the same plane. The semi-major and semi-minor axes are labeled c_i and a_i, $i = 1, 2$, respectively. The radius vectors R_i point to the locations on the nuclear surfaces that correspond to the minimum separation distance s. In the present work the nuclei are always aligned along their semi-major axes (c_i), thus the four angles α_i and θ_i are fixed at $\alpha_1 = \alpha_2 = \theta_1 = 0°$ and $\theta_2 = 180°$. Two additional angles, ϕ_i, represent rotations out of the common plane of the figure. These two angles are fixed at $0°$ in the present work.

---

separation distance between the two surfaces, s. The surface energy coefficient, γ, was determined from the Lysekil mass formula [5]

$$\gamma = 0.957 \left(1 - 1.7826 I^2\right) \text{ MeV/fm}^2$$

where $I = (N - Z)/A$ is the relative neutron excess of the entire system, i.e. $A = A_1 + A_2$, $Z = Z_1 + Z_2$, and $N = N_1 + N_2$, for adjacent fragments 1 and 2. The Süssman width b was determined assuming a "10–90 fall-off distance", $t_{10\text{-}90}$, of 2.4 fm [4]. This resulted in a value of $b = 0.99$ fm using the following expression

$$b = \frac{\pi}{2\sqrt{3}\ln 9} \cdot t_{10\text{-}90}.$$

The mean curvature radius, $\overline{R}$, is a kind of "reduced radius" of the two adjacent fragments. For the case of two prolate spheroids the mean curvature radius is given

by

$$\frac{1}{\overline{R}^2} = \frac{1}{R_{11}R_{12}} + \frac{1}{R_{21}R_{22}} + \left[\frac{1}{R_{11}R_{21}} + \frac{1}{R_{12}R_{22}}\right]\text{Sin}^2\phi + \left[\frac{1}{R_{11}R_{22}} + \frac{1}{R_{21}R_{12}}\right]\text{Cos}^2\phi,$$

where ϕ is the azimuthal angle between the principal planes of curvature of the two nuclei (a measure of the skewness between the two adjacent fragments, see Fig. D.1) and the four principal radii of curvature are given by

$$R_{i1} = \left|\frac{\left(R_i^2(\alpha_i) + [R_i'(\alpha_i)]^2\right)^{3/2}}{R_i''(\alpha_i)R_i(\alpha_i) - 2[R_i'(\alpha_i)]^2 - R_i^2(\alpha_i)}\right|, \tag{D.1}$$

$$R_{i2} = \left|\frac{R_i(\alpha_i)\text{Sin}\,\alpha_i\left[R_i^2(\alpha_i) + (R_i'(\alpha_i))^2\right]^{1/2}}{R_i'(\alpha_i)\text{Cos}\,\alpha_i - R_i(\alpha_i)\text{Sin}\,\alpha_i}\right|, \tag{D.2}$$

for fragments $i = 1, 2$ respectively. The radius vector for a prolate spheroid as a function of the angle α with respect to the semi-major axis is given by

$$R_i(\alpha_i) = \left[\frac{\text{Sin}^2\alpha_i}{a_i^2} + \frac{\text{Cos}^2\alpha_i}{c_i^2}\right]^{-1/2} \tag{D.3}$$

where a_i and c_i are the semi-minor and semi-major axes respectively for fragment i. The quantities R_i appearing in Eqs. D.1 and D.2 are actually the effective central radii of two sharp spheres, each generating a diffuse potential. Mathematically, each is a mean between the central radii of the density and potential distributions for each fragment,

$$R_i = R_i^\circ - \frac{b}{R_i^\circ} \qquad i = 1, 2 \tag{D.4}$$

where b is again the Süssman width, and R_i° is the effective sharp radius of fragment i given by Eq. D.3. The first and second derivatives of Eq. D.3 are given by

$$R_i'(\alpha_i) = -\left[\frac{\text{Sin}^2\alpha_i}{a_i^2} + \frac{\text{Cos}^2\alpha_i}{c_i^2}\right]^{-3/2}\left(\frac{1}{a_i^2} - \frac{1}{c_i^2}\right)\text{Sin}\,\alpha_i\,\text{Cos}\,\alpha_i$$

$$R_i''(\alpha_i) = \frac{\left(a_i^2 - c_i^2\right)\left(4\left(a_i^2 + c_i^2\right)\text{Cos}\,2\alpha_i - \left(a_i^2 - c_i^2\right)\left(-5 + \text{Cos}\,4\alpha_i\right)\right)}{8\left[\frac{\text{Sin}^2\alpha_i}{a_i^2} + \frac{\text{Cos}^2\alpha_i}{c_i^2}\right]^{1/2}\left(a_i^2\text{Cos}^2\alpha_i + c_i^2\text{Sin}^2\alpha_i\right)^2}.$$

In the present work the fragments are always aligned along their semi-major axes, meaning that the angles α_i are always zero and thus the first derivatives, R'_i, are always zero.

Finally, the proximity moment $\Phi(s)$ is defined as

$$\Phi(s) = \begin{cases} -\frac{1}{2}(s-s_0)^2 - k(s-s_0)^3 & (s \leq s_1) \\ \\ -3.437 \exp\left[-s/0.75\right] & (s \geq s_1) \end{cases} \tag{D.5}$$

where s is the minimum gap width between adjacent nuclear surfaces, $s_1 = 1.2511$ represents a discontinuity in the underlying universal proximity function ϕ, and $s_0 = 2.54$ (see reference [1] for details). The minimum gap width used in Eq. D.5 was determined by applying corrections for the surface diffuseness to the sum of the semi-major axes of the adjacent fragments

$$s = \frac{1}{b}(R - R_1 - R_2).$$

Here the quantity $R = c_1 + c_2$ is the sum of the semi-major axes of the two adjacent prolate spheroids calculated as

$$c_i = \left[\frac{3\,V_i^{\text{sph}}}{4\pi\sqrt{1-\varepsilon_i^2}}\right]^{1/3}.$$

where V_i^{sph} is the volume of the equivalent sphere and ε_i is the eccentricity of fragment i. The quantities R_1 and R_2, for adjacent fragments 1 and 2, are the semi-major axis of the two fragments corrected for surface diffuseness using Eq. D.4, i.e.

$$R_i = c_i - \frac{b}{c_i} \qquad i = 1,\,2.$$

References

[1] J. Blocki, J. Randrup, W. Swiatecki, and C. Tsang, Ann. Phys. **105**, 427 (1977).

[2] A. Baltz and B. Bayman, Phys. Rev. C **26**, 1969 (1982).

[3] N. Malhotra and R. K. Gupta, Phys. Rev. C **31**, 1179 (1985).

[4] W. Myers, Nucl. Phys. **A204**, 465 (1973).

[5] W. Myers and W. Swiatecki, Ark. Fys. **36**, 343 (1967).

Appendix E

Droplet Model Binding Energy

The Droplet Model of nuclei is an extension of the Liquid Drop Model, used to describe the average behavior of the nuclear binding energy. The refinements take into account effects associated with deviations of the neutron and proton densities from their respective bulk values, as well as certain shell effects. The Droplet Model (DM) expressions were originally derived by Myers and Swiatecki [1, 2, 3] and re-evaluated by Hasse [4]. The total DM binding energy of a nucleus of atomic number Z and mass number A is calculated as

$$
\begin{aligned}
E_{\text{total}} \;=\; & \left[-a_1 + J\bar{\delta}^2 - \frac{1}{2}K\bar{\epsilon}^2 + \frac{1}{2}M\bar{\delta}^4 \right] \cdot A \\[2mm]
& + \left[a_2 + \frac{9J^2}{4Q}\bar{\delta}^2 \right] \cdot A^{2/3}B_{\text{surf}} + a_3 A^{1/3}B_{\text{curv}} \\[2mm]
& + c_1 Z^2 A^{-1/3} B_{\text{Coul}} - c_2 Z^2 A^{1/3} B_{\text{red}} \\[2mm]
& - c_3 Z^2 A^{-1} - c_4 Z^{4/3} A^{-1/3} - c_5 Z^2 B_{\text{sr2}}, \tag{E.1}
\end{aligned}
$$

where

$$
\bar{\delta} \;=\; \left[I + \frac{3c_1}{16Q} Z A^{-2/3} B_{\text{sr1}}^{1/2} \right] \Big/ \left[1 + \frac{9J}{4Q} A^{-1/3} B_{\text{surf}} \right] \tag{E.2}
$$

$$
\bar{\epsilon} \;=\; \frac{1}{K} \left[-2a_2 A^{-1/3} B_{\text{surf}} + c_1 Z^2 A^{-4/3} B_{\text{Coul}} + L\bar{\delta}^2 \right]. \tag{E.3}
$$

Note that the first terms in each of the first three lines of Eq. E.1 together form the standard Liquid Drop Model (LDM) binding energy

$$
\begin{aligned}
E_{\text{total}}^{\text{LDM}} \quad = \quad & -a_1 A && \text{(volume energy)} \\
& + a_2 A^{2/3} B_{\text{surf}} && \text{(surface energy)} \\
& + c_1 Z^2 A^{-1/3} B_{\text{Coul}} && \text{(Coulomb energy)}.
\end{aligned}
$$

The additional terms in Eq. E.1 represent the corrections to the LDM expression incorporated into the Droplet Model.

In Eqs. E.1 – E.3 the quantities A, N, Z, and $I = (N - Z)/A$ are specific to the nucleus under consideration, identifying the mass, neutron number, proton (atomic) number and relative neutron excess respectively. The total energy also depends on two additional sets of quantities, constants and shape dependencies. The constants, using the notation of Myers and Swiatecki, along with the values used in the present calculations are as follows:

$a_1 = 15.986$ MeV   volume energy coefficient.
$a_2 = 20.76$ MeV   surface energy coefficient.
$a_3 = 0.0$ MeV   curvature energy coefficient.
$c_1 = 0.73531$ MeV   Coulomb energy coefficient.
$c_2 = 1.6477 \times 10^{-4}$ MeV   Coulomb redistribution coefficient.
$c_3 = 1.30501$ MeV   Coulomb diffuseness coefficient.
$c_4 = 0.56149$ MeV   Coulomb exchange coefficient.
$c_5 = 4.9695 \times 10^{-4}$ MeV   surface redistribution coefficient of second kind.
$J = 36.6$ MeV   symmetry energy coefficient.
$K = 240.0$ MeV   compressibility coefficient.
$L = 100.0$ MeV   density-symmetry coefficient.
$M = 0.0$ MeV   symmetry anharmonicity coefficient.
$Q = 17.0$ MeV   effective surface stiffness coefficient.

The shape dependencies are defined such that they assume a value of unity for spherical shapes. The shape dependencies appearing in Eqs. E.1 – E.3 are as follows:
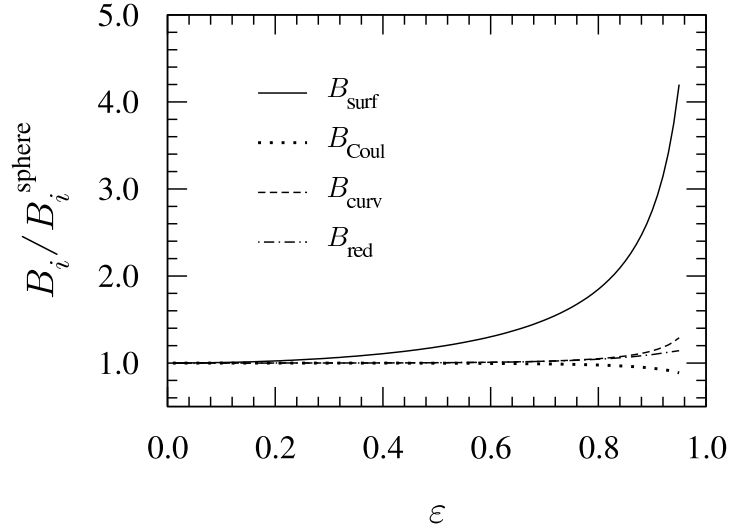
Figure E.1: Shape dependencies in the Droplet Model. The variation in the DM binding energy for deformed nuclei, relative to the spherical result, is dominated by the change in the surface energy. The variations in the Coulomb, curvature and Coulomb redistribution energies are much less by comparison.

B_{surf} surface energy shape dependence.

B_{Coul} Coulomb energy shape dependence.

B_{curv} curvature energy shape dependence.

B_{red} Coulomb redistribution shape dependence.

B_{sr1} shape dependence of the surface redistribution of the first kind.

B_{sr2} shape dependence of the surface redistribution of the second kind.

The first four shape dependencies lend themselves to rather straightforward interpretation. These four quantities are plotted in Fig. E.1. The surface energy shape dependence accounts for the increase in the surface area for any non-spherical shape. For prolate deformations parametrized by the eccentricity, ε, the surface energy shape dependence is calculated as

$$B_{\text{surf}} = \frac{1}{2\sqrt[3]{1-\varepsilon^2}}\left[1 + \frac{\text{Sin}^{-1}\varepsilon}{\varepsilon\sqrt[3]{1-\varepsilon^2}}\right]$$

which is an increasing function of the eccentricity describing the increase in surface area of the nucleus. The Coulomb energy shape dependence considers the change in the mean charge separation for non-spherical shapes. For the present case the Coulomb energy shape dependence is calculated as

$$B_{\text{Coul}} = \frac{\sqrt[3]{1-\varepsilon^2}}{2\,\varepsilon} \ln \frac{1+\varepsilon}{1-\varepsilon}.$$

B_{Coul} is a decreasing function of the eccentricity. The curvature energy shape dependence is a correction to the surface energy to account for the finite curvature of the nuclear surface:

$$B_{\text{curv}} = \frac{1}{2\sqrt[3]{1-\varepsilon^2}} \left[1 + \frac{(1-\varepsilon^2)}{2\varepsilon} \ln \frac{1+\varepsilon}{1-\varepsilon} \right].$$

It is an increasing function of the eccentricity. Finally, the Coulomb redistribution energy shape dependence introduces a correction to the Coulomb energy to account for the redistribution of the protons due to compression of the nucleus as it is deformed

$$
\begin{aligned}
B_{\text{red}} \;=\; & \frac{3}{4}\left(1-\varepsilon^2\right)^{2/3} \left[\frac{3}{4\varepsilon^2}\left(\ln\frac{1+\varepsilon}{1-\varepsilon}\right)^2 \right. \\
& \left. - \frac{5}{\varepsilon^3}\ln\frac{1+\varepsilon}{1-\varepsilon}\left(\frac{1}{2\varepsilon}\ln\frac{1+\varepsilon}{1-\varepsilon}-1\right) + \frac{15}{\varepsilon^4}\left(\frac{1}{\varepsilon}\ln\frac{1+\varepsilon}{1-\varepsilon}-1\right)^2 \right].
\end{aligned}
$$

From Fig. E.1 it is clear that the greatest variation from the spherical result occurs in the surface energy. The effects from the remaining three shape dependencies are minor in comparison.

The last two shape dependencies are not as intuitive as those plotted in Fig. E.1. These are the surface redistribution energy of the first kind

$$B_{\text{sr1}} = 25p_1^2 - 60p_1 B_{\text{Coul}} B_{\text{surf}} + 36 B_{\text{Coul}}^2 B_{\text{surf}}^2,$$

and the surface redistribution energy of the second kind

$$B_{\text{sr2}} = 25p_2 - 60p_1 B_{\text{Coul}} + 36 B_{\text{Coul}}^2 B_{\text{surf}}.$$

The above two shape dependencies are corrections to the surface energy arising from the redistribution of neutrons and protons due to compression of the nucleus as it is deformed. The quantities p_1 and p_2 appearing in the expressions for the surface redistribution dependencies are defined as

$$p_1 = 0.0938 \left[1 - \varepsilon^2\right]^{1/3} \left[8\xi_1 B_{\text{surf}} \right.$$

$$\left. + \frac{\xi_2}{\varepsilon^2} \left(\frac{\text{Sin}^{-1}\varepsilon}{\varepsilon \left[1 - \varepsilon^2\right]^{1/6}} - \left[1 - \varepsilon^2\right]^{1/3} \left(1 - 2\varepsilon^2\right) \right) \right]$$

and

$$p_2 = 0.2813 \left[1 - \varepsilon^2\right]^{2/3} \left[2\xi_1 B_{\text{surf}} \right.$$

$$\left. + 0.125 \frac{\xi_2 \text{Sin}^{-1}\varepsilon}{\varepsilon^3 \left[1 - \varepsilon^2\right]^{1/6}} \left(4\xi_1 + \frac{\xi_2}{\varepsilon^2} - 4\xi_1 \left[1 - \varepsilon^2\right]^{1/3} \left(1 + \frac{2}{3}\varepsilon^2 - \frac{8}{3}\varepsilon^4\right) \right) \right]$$

where

$$\xi_0 = \frac{1}{2\varepsilon} \ln \frac{1 + \varepsilon}{1 - \varepsilon}$$

$$\xi_1 = \xi_0 + \frac{1}{\varepsilon^2} \left(\xi_0 - 1\right)$$

$$\xi_2 = \xi_0 + \frac{3}{\varepsilon^2} \left(\xi_0 - 1\right).$$

Aside from the volume term, the two remaining terms in the DM binding energy that do not have an associated shape dependence are the diffuseness and exchange energies respectively appearing in the last line of Eq. E.1.

References

[1] W. Myers and W. Swiatecki, Nucl. Phys. **81**, 1 (1966).

[2] W. Myers and W. Swiatecki, Ann. Phys. **55**, 395 (1969).

[3] W. Myers and W. Swiatecki, Ann. Phys. **84**, 186 (1974).

[4] R. W. Hasse, Ann. Phys. **68**, 377 (1971).